



TECHNISCHE  
UNIVERSITÄT  
DARMSTADT

# **Modelling of radiative heat transfer in oxy-fuel combustion scenarios**

**Vom Fachbereich Maschinenbau  
an der Technischen Universität Darmstadt**

zur Erlangung des akademischen Grades  
Doktor–Ingenieur (Dr.–Ing.)

**genehmigte DISSERTATION  
von M.Sc. Vitali Kez aus Karabulak**

Erstgutachter: Prof. Dr.–Ing. Bernd Epple  
Zweitgutachter Prof. Dr.–Ing. Jean-Louis Consalvi

Tag der Einreichung: 20. 10. 2021  
Tag der mündlichen Prüfung: 12. 01. 2022

Darmstadt 2022  
D17

## Modelling of radiative heat transfer in oxy-fuel combustion scenarios

Genehmigte Dissertation von M.Sc. Vitali Kez

Erstgutachter: Prof. Dr.–Ing. Bernd Epple

Zweitgutachter: Prof. Dr.–Ing. Jean-Louis Consalvi

Tag der Einreichung: 20.10.2021

Tag der Prüfung: 12. 01. 2022

Darmstadt, Technische Universität Darmstadt

Dieses Dokument wird bereitgestellt von TUprints,

E-Publishing-Service der TU Darmstadt

<http://tuprints.ulb.tu-darmstadt.de>

[tuprints@ulb.tu-darmstadt.de](mailto:tuprints@ulb.tu-darmstadt.de)

URN: urn:nbn:de:tuda-tuprints-205167

Jahr der Veröffentlichung der Dissertation auf TUprints: 2022

Veröffentlicht unter CC BY-SA 4.0 International

<https://creativecommons.org/licenses/>



# Preface

The present Ph.D. thesis “Modelling of radiative heat transfer in oxy-fuel combustion scenarios” is the result of my time as a doctoral candidate and scientific employee of sub-project C3 of the collaborative research project SFB/TRR 129 “Oxyflame” at the Department of Energy Systems and Technology at the Technische Universität Darmstadt. I would like to express my gratitude to all those who gave me the possibility to complete this thesis.

I wish to thank:

Prof. Dr.–Ing. Bernd Epple, the supervisor of this Ph.D. thesis, for his valuable guidance and for giving me the opportunity to do this wonderful work,

Prof. Dr.–Ing. Jean-Louis Consalvi, the reviewer of this Ph.D. thesis, for numerous advice, the wonderful cooperation, the possibility for working as a visiting scientist at his institute in Marseille and taking over the co-review of this work,

Dr.–Ing. Jochen Ströhle, my supervisor in the sub-project C3, for introducing me to the interesting topic of thermal radiation, giving me advice, direction and supervision for my research,

Ph.D. Fengshan Liu for the wonderful cooperation, a lot of support and many valuable scientific discussions,

PD Dr.–Ing. habil. Falah Alobaid and Dr.–Ing. Ralf Starkloff, friends of mine for the friendship, many valuable scientific discussions and constant support to finish this Ph.D. thesis, and all scientific staff and students at EST.

Exceptionally, I would like to express my gratitude to my parents (Emilia and Viktor) for their constant support during the long time period of my education, their advice to put education on the first place, their help and love without expecting anything in return. Without you, I would never have the possibility to even start this thesis. Finally, I would like to thank my wonderful wife (Marta) and my son (Milan) for their patience, sacrifice, the belief that, in the end, I will finish this work and the incredible love.

Diese Arbeit ist im Rahmen des Sonderforschungsbereiches SFB/TRR 129 entstanden und ich bedanke mich bei der DFG für die finanzielle Unterstützung.

# Ehrenwörtliche Erklärung

Ich erkläre hiermit ehrenwörtlich, dass ich die vorliegende Arbeit selbstständig angefertigt habe. Sämtliche aus fremden Quellen direkt oder indirekt übernommenen Gedanken sind als solche kenntlich gemacht.

Die Arbeit wurde bisher keiner anderen Prüfungsbehörde vorgelegt und noch nicht veröffentlicht.

Wilkszyn, den 20. Oktober 2021

A handwritten signature in black ink, appearing to read 'Vitali Kez'.

(Vitali Kez)

# TABLE OF CONTENTS

<b>PREFACE</b> .....	<b>III</b>
<b>EHRENWÖRTLICHE ERKLÄRUNG</b> .....	<b>IV</b>
<b>TABLE OF CONTENTS</b> .....	<b>V</b>
<b>NOMENCLATURE</b> .....	<b>VII</b>
<b>ZUSAMMENFASSUNG</b> .....	<b>1</b>
<b>ABSTRACT</b> .....	<b>2</b>
<b>1 INTRODUCTION</b> .....	<b>3</b>
1.1 State of the art .....	5
1.2 Research objectives .....	9
1.3 Thesis outline .....	9
<b>2 THERMAL RADIATION MODELLING</b> .....	<b>11</b>
2.1 Radiative Transfer Equation .....	11
2.2 Gas radiation modelling.....	14
2.2.1 Statistical Narrow-Band Model .....	16
2.2.2 Narrow-Band Correlated-k .....	17
2.2.3 Wide-Band Correlated-k based on spectroscopic database HITEMP 2010.....	21
2.2.4 Full-Spectrum Correlated-k Model .....	22
2.2.5 Weighted-Sum-of-Gray-Gases Model.....	24
2.2.6 Wide-Band Correlated-k Model based on Exponential Wide-Band Model .....	28
2.2.6.1 Spectral formulation.....	31
2.2.6.2 Gray gases formulation .....	31
2.2.6.3 Multiple gases formulation.....	32
2.3 Particle radiation modelling .....	32
2.3.1 Mie Theory.....	33
2.3.2 Henyey-Greenstein Phase Function .....	36
2.3.3 Transport Approximation .....	36
2.3.4 Approximate particle properties .....	37
2.3.5 Particle material properties .....	39

<b>2.4</b>	<b>Numerical Methods</b> .....	<b>39</b>
2.4.1	Discrete Transfer Method.....	39
2.4.2	Discrete Ordinates Method.....	41
2.4.3	Finite Volume Method.....	42
2.4.4	Spatial Discretization Schemes.....	44
<b>3</b>	<b>RESULTS</b> .....	<b>45</b>
<b>3.1</b>	<b>Gas radiation modelling in a 3D virtual oxy-fuel gas turbine combustor with dry recycle</b> .....	<b>45</b>
3.1.1	Results and discussion.....	47
3.1.1.1	Case 1 (dry recycle with 40 % CO <sub>2</sub> in fuel/oxidizer mixture) .....	48
3.1.1.2	Case 2 (dry recycle with 62.5 % CO <sub>2</sub> in fuel/oxidizer mixture) .....	54
3.1.1.3	Overall performance.....	58
3.1.2	Conclusions .....	60
<b>3.2</b>	<b>Gas radiation modelling in a 3D virtual coal-fired furnace</b> .....	<b>61</b>
3.2.1	Results and discussion.....	63
3.2.1.1	Case 1 (air-fuel combustion) .....	63
3.2.1.2	Case 2 (oxy-fuel combustion with dry recycle) .....	68
3.2.1.3	Case 3 (oxy-fuel combustion with wet recycle).....	72
3.2.1.4	Overall model performance.....	79
3.2.2	Conclusions .....	80
<b>3.3</b>	<b>Gas-particle radiation modelling in a 2D virtual oxy-fuel coal-fired furnace with wet recycle</b> ...	<b>82</b>
3.3.1	Results and discussion.....	84
3.3.1.1	Influences of various contributions on total radiation.....	85
3.3.1.2	Influence of particle radiation modelling within the NBCK context .....	88
3.3.1.3	Influence of gas radiation modelling .....	94
3.3.2	Conclusions .....	96
<b>4</b>	<b>CONCLUSIONS AND PERSPECTIVES</b> .....	<b>98</b>
	<b>BIBLIOGRAPHY</b> .....	<b>103</b>

# Nomenclature

## Latin symbols

$A$	surface area	$[m^2]$
$a$	weighting function of considered global model	$[-]$
$a_n$	Mie coefficient	$[-]$
$b$	polynomial coefficient	$[-]$
$b_n$	Mie coefficient	$[-]$
$C$	cross section of absorption, scattering or extinction	$[m^2]$
$E_1$	first-order exponential function	$[-]$
$F$	blackbody fraction	$[-]$
$f$	absorption coefficient distribution function of correlated-k model	$[-]$
$f_A$	cross-sectional area per volume of considered particles	$[m^2/m^3]$
$f_a$	axial factor	$[-]$
$f_b$	burnout factor	$[-]$
$f_m$	mixing factor	$[-]$
$f_r$	radial factor	$[-]$
$g$	cumulative distribution function of correlated-k model, asymmetry factor	$[-], [-]$
$H$	Heaviside's unit step function	$[-]$
$h_n^{(1)}$	spherical Hankel function of $n^{\text{th}}$ order	$[-]$
$I$	radiative intensity	$[W/m^2 sr]$
$i_{\parallel}$	ratio of scattered to incident intensity parallel to scattering plane	$[-]$
$i_{\perp}$	ratio of scattered to incident intensity perpendicular to scattering plane	$[-]$
$j_n$	spherical Bessel function of $n^{\text{th}}$ order	$[-]$
$k$	reordered absorption coefficient of correlated-k model, absorptive index	$[m^{-1}], [-]$
$\bar{k}$	ratio of mean line strength to mean line spacing of SNB model	$[m^{-1} bar^{-1}]$
$L$	length (in x-, y-, z-direction; gas column), order of polynomial function	$[m], [-]$
$l$	direction cosine	$[-]$
$m$	complex index of refraction	$[-]$
$n$	refractive index	$[-]$
$\vec{n}$	normal unit vector	$[m]$
$P_n$	Legendre polynomial of $n^{\text{th}}$ order	$[-]$
$p$	(partial) pressure	$[bar]$
$Q$	efficiency of absorption, scattering or extinction	$[-]$
$q$	heat flux	$[W/m^2]$

$r$	radius/ radial distance	[m]
$S$	source function, line strength	$[W/m^2 sr], [cm^{-1}]$
$\vec{s}$	direction of considered ray	[-]
$T$	temperature	[K]
$V$	volume	$[m^3]$
$\overline{W}$	mean value of the equivalent black-line widths of SNB model	$[cm^{-1}]$
$w_G$	associated weight of Gauss-Legendre quadrature point	[-]
$w^m$	quadrature weight of associated direction $m$	[-]
$x$	location, size parameter	[m], [-]
$Y$	mole fraction of gas species	[-]
$x, y, z$	Cartesian coordinates	[m]

### Greek symbols

$\vec{\nabla}$	nabla operator	$[m^{-1}]$
$\alpha$	absorptivity, integrated band intensity	[-], $[cm^{-1}/(g/m^2)]$
$\beta$	extinction coefficient	$[m^{-1}]$
$\overline{\beta}$	average line-width to spacing ratio of SNB model	[-]
$\overline{\gamma}$	average line Lorentz half-width of SNB model	$[cm^{-1}]$
$\Delta$	relative error	[-]
$\delta$	mean line spacing, Dirac-delta function	$[cm^{-1}], [-]$
$\overline{\delta}$	weighted mean line spacing between two spectral lines of SNB model	$[cm^{-1}]$
$\varepsilon$	emissivity	[-]
$\eta$	wavenumber	$[cm^{-1}]$
$\theta$	azimuthal angle	[rad]
$\kappa$	absorption coefficient	$[m^{-1}]$
$\lambda$	wavelength	[m]
$\mu$	weighting factor of spatial discretization scheme	[-]
$\xi$	reordered wavenumber of WBC model based on EWB model	$[cm^{-1}]$
$\xi_n$	Ricatti-Bessel function of $n^{\text{th}}$ order based on Hankel functions	[-]
$\pi_n$	angle dependent function of $n^{\text{th}}$ order based on Legendre polynomials	[-]
$\rho$	reflectivity	[-]
$\sigma$	scattering coefficient	$[m^{-1}]$
$\tau$	transmissivity, optical thickness	[-], [-]
$\tau_n$	angle dependent function of $n^{\text{th}}$ order based on Legendre polynomials	[-]
$\Phi$	scattering phase function	[-]
$\varphi$	polar angle	[rad]
$\phi$	physical variable	[different]
$\psi$	scattering angle	[rad]
$\psi_n$	Ricatti-Bessel function of $n^{\text{th}}$ order based on spherical Bessel functions	[-]
$\Omega$	solid angle	[sr]
$\omega$	single scattering albedo, band width parameter of EWB model	[-], $[cm^{-1}]$

**Constants**

$C_1$	radiation constant	$[W \mu\text{m}^4/\text{m}^2 \text{sr}]$
$C_2$	radiation constant	$[\mu\text{m K}]$
$c_0$	speed of light in vacuum	$[\text{m/s}]$
$h$	Planck constant	$[\text{kg m}^2/\text{s}]$
$k_B$	Boltzmann constant	$[\text{kg m}^2/\text{s}^2 \text{K}]$
$\sigma_{SB}$	Stefan–Boltzmann constant	$[\text{W}/\text{m}^2 \text{K}^4]$

**Superscripts, subscripts and indices**

0	reference state
<i>abs</i>	absorption
<i>ad</i>	adiabatic
<i>b</i>	blackbody, state of the burnout
$CO_2$	carbon dioxide
<i>CV</i>	control volume
<i>c</i>	centerline, center
<i>d</i>	state of the diluent
<i>div</i>	divergence
<i>e</i>	state at the exit
<i>ext</i>	extinction
<i>f</i>	state of fuel/oxidizer mixture, radiative heat flux
<i>G</i>	quadrature point of Gauss-Legendre quadrature scheme
<i>g</i>	gas, cumulative distribution function of correlated-k model
$H_2O$	water vapor
<i>HG</i>	Henyey-Greenstein
<i>i</i>	midpoint of surface element of control volume, state at the inlet, considered ray direction, considered wide-band
<i>j</i>	considered narrow-band
<i>k</i>	gray gas
<i>l</i>	lower, gas species, axial position
<i>m</i>	angular direction
<i>mf</i>	mole fraction
<i>mix</i>	mixture
<i>mod</i>	modified
<i>n</i>	normalized, iteration step
<i>nb</i>	narrow-band
<i>P</i>	midpoint of control volume
<i>Pm</i>	Planck-mean
<i>p</i>	particle
<i>s</i>	solid phase, radiative source term

---

<i>sca</i>	scattering
<i>Tr</i>	transport approximation
<i>u</i>	upper
<i>V</i>	volatiles
<i>w</i>	wall
<i>wb</i>	wide-band
$\eta$	spectral dependence on wavenumber

## Abbreviations

APH	air preheater
ASU	air separation unit
CCUS	carbon capture, utilization and storage
CFD	computational fluid dynamics
DOM	discrete ordinates method
DTM	discrete transfer method
ESP	electrostatic precipitator
EWBM	exponential wide-band model
FGD	flue gas desulfurization
FOM	fuel/oxidizer mixture
FSCK	full-spectrum correlated-k
FVM	finite volume method
GGF	gray gases formulation
HG	Henyey-Greenstein
IGCC	integrated gasification combined cycle
MFS	mean flux scheme
MGF	multiple gases formulation
MR	molar ratio
NBCK	narrow-band correlated-k
NBKD	narrow-band k-g distribution database
RTE	radiative transfer equation
SCR	selective catalytic reduction reactor
SLW	spectral-line based weighted-sum-of-gray-gases
SNB	statistical narrow-band
SPF	spectral formulation
WBCK	wide-band correlated-k
WBKD	wide-band k-g distribution database
WSGG	weighted-sum-of-gray-gases



# Zusammenfassung

Die Oxyfuel-Verbrennung fossiler Energieträger stellt eine vielversprechende Technologie zur Reduzierung des anthropogen erzeugten Kohlenstoffdioxidausstoßes neuer als auch bestehender Kraftwerke dar. Die Verwendung von reinem Sauerstoff und die Rückführung eines Anteils des Abgases in die Brennkammer bedingen im Vergleich zur Luftverbrennung einen erhöhten Anteil von Kohlenstoffdioxid und Wasserdampf im Brennraum, der die thermische Gasstrahlung stark beeinflusst. Dabei zeigt vor allem der Absorptionskoeffizient dieser Moleküle einen stark schwankenden Verlauf über den zu berücksichtigenden Spektralbereich, so dass ein nicht-graues Strahlungsmodell zur genauen Berechnung der Strahlungswärmeübertragung bei Einsatz numerischer Lösungsverfahren verwendet werden muss.

In dieser Arbeit werden Schmalbandmodelle zur Bestimmung der Referenzlösungen verwendet und anhand dieser die Genauigkeit der Breitband- und globalen Strahlungsmodelle für drei unterschiedliche Geometrien untersucht. Die Parameter der Breitbandmodelle werden auf Basis der Spektraldatenbank des Exponential Wide-Band Modells und der für Hochtemperaturanwendungen abgeleiteten Spektraldatenbank HITEMP 2010 bestimmt. Die Full-Spectrum Correlated-k und Weighted-Sum-of-Gray-Gases Modelle werden zur Beurteilung der Genauigkeit globaler Strahlungsmodelle betrachtet. Dabei werden sieben unterschiedliche Parametersätze für das Weighted-Sum-of-Gray-Gases Modell berücksichtigt, welche für Luft- und Oxy-fuel-Verbrennungsatmosphären hergeleitet wurden, und eine Empfehlung zu ihrem Einsatz in kommerziell verfügbaren CFD-Softwarepaketen gegeben.

In den ersten beiden 3D Geometrien (virtuelle Gasturbinenbrennkammer mit trockener Abgasrezirkulation und virtuelle mit kohlebefeuerten Brennkammer mit Luft-, trockener und nasser Oxy-fuel-Verbrennungsumgebung) wurde festgestellt, dass das NBCK Modell sich zur Berechnung der Referenzlösungen aufgrund der sehr hohen Genauigkeit bei verringerter Rechenleistung eignet. Bei kurzen Pfadlängen und hohen Betriebsdrücken zeigen alle untersuchten Gasstrahlungsmodelle eine ähnliche Genauigkeit. Bei langen Pfadlängen und Atmosphärendruck weisen die verwendeten Spektraldatenbanken und die berücksichtigten Druck-Weglängen zur Ableitung der Strahlungseigenschaften eine große Bedeutung auf die Genauigkeit der Simulationsergebnisse auf. Dabei eignen sich das FSCK Modell und das WSGG Modell mit den Parametern von Bordbar et al. (2014), beide basierend auf der HITEMP 2010 Spektraldatenbank, zur genauen Beschreibung der Gasstrahlung. Die Untersuchung verschiedener Approximationen zur Modellierung der Strahlungswärmeübertragung eines Gas-Partikel-Gemisches zeigte, dass die Gasstrahlung bis zu 50% der Gesamtwärmestrahlung ausmachen kann und vor allem die Gasabsorption in kälteren Temperaturbereichen zur genauen Strahlungsberechnung berücksichtigt werden sollte. Die Betrachtung der Partikelstreuung als starke Vorwärtsstreuung mittels vereinfachter Modelle wie der Henyey-Greenstein Funktion zeigte eine hohe Genauigkeit im Vergleich zu den mit der Mie-Theorie bestimmten Referenzlösungen. Die Verwendung grauer Streuungsfunktionen, die über Planck-gemittelte Asymmetriefaktoren bestimmt werden, zeigte eine hohe Genauigkeit bei Abweichungen geringer als 10% von den Referenzlösungen. Eine Reduktion der spektralen Auflösung mittels der WBCK oder FSCK Methoden, basierend auf der HITEMP 2010 Spektraldatenbank, führte zu einer starken Verringerung der Rechenleistung bei gleichbleibender Genauigkeit.

Zusammenfassend wird das Full-Spectrum Correlated-k Modell mit dem Mischungsansatz nach Modest und Riazzi (2005) in Verbindung mit grauen Partikelstrahlungseigenschaften für den Einsatz in numerischen Simulationen realer Oxyfuel-Verbrennungsanwendungen empfohlen, da dieses konsistent für alle untersuchten Oxyfuel-Verbrennungsszenarien eine hohe Vorhersagegenauigkeit und einen angemessenen Rechenaufwand aufwies.

# Abstract

The oxy-fuel combustion of fossil fuels is a promising carbon capture technology for the design of new thermal power plants as well as retrofitting existing ones to reduce the emission of anthropogenic produced carbon dioxide into the atmosphere. The substitution of air with pure oxygen as the oxidizer and the recirculation of flue gas into the furnace lead to higher amounts of carbon dioxide and water vapor within the combustion chamber compared to air-firing systems, and, thus, strongly impact the thermal radiation by the gas phase. Especially, the erratic behavior of the absorption coefficients of these molecules in the infrared spectral range necessitates the use of a non-gray gas radiation model to accurately predict the radiative heat transfer in oxy-fuel combustion processes by means of numerical solution procedures.

In this thesis, the statistical narrow-band and the narrow-band correlated-k models are used to provide the benchmark solutions for the assessment of various radiation models. The accuracy of wide-band and global models is investigated for three different geometries. The parameters of the wide-band models are based on the older spectroscopic database of the exponential wide-band model as well as the newer HITEMP 2010 spectroscopic database. The full-spectrum correlated-k and the weighted-sum-of-gray-gases models are considered to evaluate the performance of global radiation models. For the latter one, seven different parameter sets, derived for air and oxy-fuel conditions, are investigated to provide a recommendation for its possible application in commercially available CFD software.

The first two 3D geometries represent a virtual gas turbine combustor with dry oxy-fuel combustion and a virtual furnace of a coal-fired power plant with air-firing, dry and wet oxy-fuel combustion conditions, respectively. Here, it was found that the accuracy of the NBCK model is sufficient to compute reference solutions with less computational effort. For short path lengths at high absolute pressures, all considered gas radiation models show similar accuracy. For long path lengths at atmospheric pressure, the considered pressure path lengths and the spectroscopic database used for the derivation of the radiative properties have a major influence on the accuracy of the simulation results. Here, the FSCK model and the WSGG model with the parameters of Bordbar et al. (2014), both based on the HITEMP 2010 spectroscopic database, are appropriate for modelling the gas radiation. The investigation of various approximations to model the radiative heat transfer in a gas-particulate mixture revealed that gas radiation can contribute up to 50% of the total radiation. Especially, the consideration of gas absorption in regions with lower temperatures is important to compute accurate radiative heat transfer. The approximation of particle scattering as strongly forward scattering via simpler models like Henyey-Greenstein function is sufficient to attain simulation results similar to the benchmark solutions, which were obtained with Mie theory. The application of gray Henyey-Greenstein phase functions obtained with Planck-mean weighted asymmetry factors showed a high accuracy with relative errors less than 10% in comparison to the benchmark solutions. The reduction of the spectral resolution of the radiative properties through applying a wide-band correlated-k or a full-spectrum correlated-k methodology, both based on the HITEMP 2010 spectroscopic database, yield a strong reduction in computational effort with almost no loss of accuracy.

In summary, the full-spectrum correlated-k model with the mixture scheme of Modest and Riazzi (2005) in conjunction with gray particle properties is recommended for the use in numerical simulations of real oxy-fuel combustion applications due to its consistently high accuracy and reasonable computational expense for all considered oxy-fuel combustion scenarios.

# 1 Introduction

The climate change, mainly induced by the high anthropogenic emission of greenhouse gases, is considered as a major challenge to mankind nowadays to ensure the well-being of future generations. The high energy demand of industrial countries was and is still met by a high consumption of fossil fuels yielding to an increased amount of anthropogenic emitted greenhouse gases. According to the World Energy Outlook 2019 [1] provided by the International Energy Agency, the future energy and, especially, the electricity demand will further increase due to the continuing development of countries like China or India. To satisfy this demand, besides increased share of regenerative energy resources, fossil fuels, in particular coal, will still play an important role in the future utilized mixture of energy resources. Thus, technologies like carbon capture, utilization and storage (CCUS) have to be applied to reduce the amount of carbon dioxide (CO<sub>2</sub>) emission of fossil fueled power plants as a mid-term solution.

In CCUS technologies for coal-fired power plants, as well as for thermal power plants driven by biofuels like biomass, the goal is yielding a high purity CO<sub>2</sub> flow stream, which is further compressed to higher pressures for probable storage in geological reservoirs like saline aquifers, or is used to produce valuable products like synthetic fuels [2]. Therefore, CO<sub>2</sub> capture technologies are applied, which are subdivided into three categories: post-combustion, pre-combustion and oxy-fuel combustion. Post-combustion processes capture the CO<sub>2</sub> from the flue gas of a conventional power plant after combustion by means of absorption by a liquid, e.g. amine based solvents [3], or by a solid, e.g. the carbonate looping process [4], adsorption by a solid, e.g. carbonized rice husk based materials [5], or membrane separation processes [6]. The Integrated Gasification Combined Cycle (IGCC) is an example for pre-combustion technologies [7]. Here, the coal is gasified and the resulting syngas is reformed to yield CO<sub>2</sub>, which is captured and further processed, and hydrogen that is used to drive a combined cycle power plant.

In contrast to the aforementioned CCUS technologies, the oxy-fuel process [8]–[10] utilizes oxygen rather than air to combust the fossil fuel. The oxygen is provided by an air

separation unit (ASU), or as in the chemical looping process [11] via a metal oxide, yielding a flue gas with a high  $\text{CO}_2$  content, which can be further processed. The advantage of the former oxy-fuel capture technology is the possibility to retrofit existing power plants within reasonable costs and efficiency penalties [9]. The substitution of the conventional oxidizer (air) by pure oxygen results in higher maximum combustion temperatures compared to air-fired boilers, which can lead to the melting of the ash content in the flue gas and put hazard on the commonly used pipe materials within the furnace. Thus, flue gas is recycled and mixed with the oxygen rich stream to reduce the combustion temperatures. In Figure 1, a schematic of the oxy-fuel process for pulverized coal combustion is depicted. Depending on the amount of water vapor ( $\text{H}_2\text{O}$ ) in the recycled flue gas, dry or wet flue gas recycle is differentiated. The resulting flue gas contains mainly  $\text{H}_2\text{O}$  and  $\text{CO}_2$  and is suitable for sequestration or utilization purposes after condensation of water vapor and, in the case of coal combustion, removal of impurities like nitrogen oxides, particulate matter, sulfur oxides or other non-condensable gases.

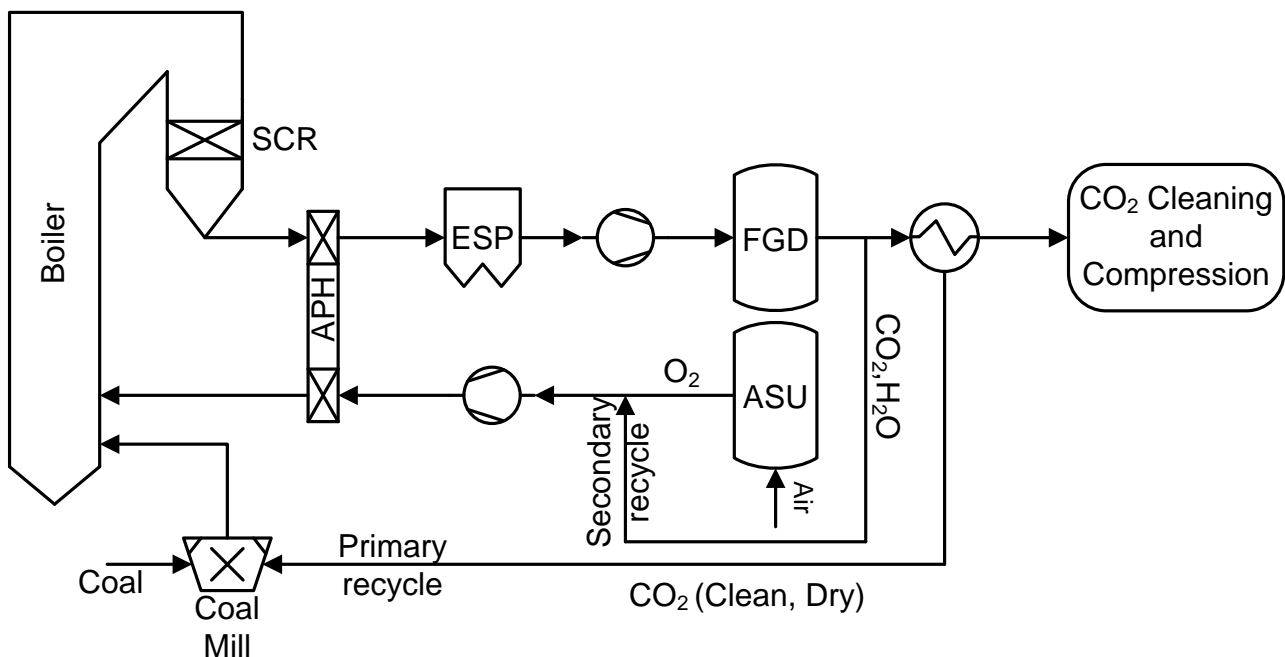


Figure 1: Schematic of coal-fired oxy-fuel process; ASU: Air Separation Unit, APH: Air Preheater, SCR: Selective Catalytic Reduction reactor, ESP: Electrostatic Precipitator, FGD: Flue gas Desulfurization; Adopted from [12]

Up to date, several oxy-fuel pilot plant projects were successfully conducted. Here, e.g. the “Schwarze Pumpe” project in Germany [13] provided insights into different operation modes, varying burner geometries, combustion conditions and their impacts on overall operation of the power plant with a thermal input of 30 MW. Current research on oxy-fuel combustion is focused on the improvement of the air-separation unit to reduce its cost and energy penalties by considering e.g. oxygen transport membranes [14] or investigating the oxy-

fuel combustion of biofuels such as biomass or waste with carbon capture [15], which may lead to negative net carbon dioxide emissions.

The encountered high temperatures in furnaces of coal-fired power plants provoke thermal radiation as the main heat transfer mechanism in this component. Thus, thermal stresses on the evaporator pipes are mainly caused by the resulting net radiative wall heat fluxes. Additionally, the radiative source terms influence the temperature distribution within the furnace and indirectly affect the formation of unwanted constituents such as carbon monoxides, nitrogen oxides or sulfur oxides. The design of new and retrofitted furnaces of coal-fired power plants is strongly accompanied by the use of computational fluid dynamics (CFD) methods. Here, the radiative transfer equation (RTE), which describes the change of radiative intensity along a line of sight, has to be solved to compute the needed radiative source terms to solve the conservation of energy equation and the net wall heat fluxes. For this purpose, accurate radiative properties, i.e. absorption coefficients for gases and particulate matter as well as scattering coefficients and scattering phase functions for particles, are needed. The highly irregular distribution of the spectral radiative properties over the considered wavenumber range makes it more difficult to find appropriate values to be used in the RTE. This fact is further complicated in oxy-fuel combustion conditions, since the concentrations of  $\text{CO}_2$  and  $\text{H}_2\text{O}$  are about five times higher compared to those in conventional air-fired systems. The main challenge is therefore to provide a radiation model for use in CFD software, which yields accurate results of the net radiative wall heat fluxes and source terms at reasonable computational expense for oxy-fuel combustion conditions.

## 1.1 State of the art

Heat transfer in coal-fired furnaces is dominated by thermal radiation. Thus, the radiative properties of both radiating gases (mainly  $\text{CO}_2$  and  $\text{H}_2\text{O}$ ) and particles (coal/char and fly-ash) should be accurately modelled in the numerical simulation of combustion, heat transfer, and pollutant formation in coal-fired furnaces. The overall accuracy of CFD software packages used to design and/or provide insight into the operation of coal-fired furnaces is strongly influenced by the accuracy of the radiative heat transfer model. Since the radiation characteristics under oxy-fuel combustion conditions are quite different from those under conventional air-fuel conditions, the non-gray behavior of the gas radiation becomes more pronounced and has to be accounted for. In this context, it was found, see e.g. [16]–[20], that narrow-band models, like the statistical narrow-band model (SNB) [21] or the narrow-band

correlated-k model (NBCK) [22], are of similar accuracy as line-by-line (LBL) calculations [23] for predicting spectral-integrated radiative output in such configurations, also at elevated pressures. However, narrow-band models are much more computationally efficient than LBL calculations, since the spectral domain of interest is sub-divided into narrow-bands of about 25 to 100  $\text{cm}^{-1}$ . Thus, the RTE has to be solved for few hundred narrow-bands rather than about  $10^6$  for LBL calculations. As a consequence, the simulation results of the narrow-band models can serve as the benchmark for other approximate radiation models in the absence of LBL or experimental results. The NBCK model is preferred over the SNB model, since it provides the absorption coefficient distribution in each narrow-band and, thus, can be applied with any method to solve the RTE. In contrast, the SNB model relies on spectrally averaged transmissivities so that a ray-tracing type of method [24] has to be used to solve the RTE. This introduces additional computational effort if scattering is taken into account, since the considered rays have to be tracked in each iteration step during the solution process to obtain the in-scattering term and meet the convergence criterion.

Nevertheless, narrow-band models are still very computationally expensive when used to model radiative transfer in multidimensional engineering applications. Thus, wide-band models were developed, which treat an entire vibrational-rotational band as a single band [25]. Especially, the wide-band correlated-k (WBCK) approach [26], [27] offers the possibility to use the absorption coefficient as the main radiative property to solve the RTE, making it straightforward to handle particle scattering. In the context of oxy-fuel combustion involving only gas radiation, the study by Chu et al. [19] showed the potential of the WBCK model based on the HITEMP 2010 spectroscopic database to offer very similar accuracy as its NBCK counterpart but at significantly less computational effort. Ströhle [28] introduced different formulations of the WBCK model based on the database of the exponential wide-band model [25], [29] to further reduce the computational effort with reasonable accuracy considering only gas radiation.

The need for even more efficient radiation models to be used in CFD software for the design and investigation of engineering applications led to the development of so-called global models. In these models the radiative properties are evaluated across the entire spectral range of interest. Commonly used global models include the weighted-sum-of-gray-gases (WSGG) [30], the spectral-line based WSGG (SLW) [31]–[34] and the full-spectrum correlated-k (FSCK) [35]–[37] model. However, also other global models like the cumulative wavenumber method [38], [39] or the  $l$ -distribution method [40] were proposed to deal with inhomogeneous, non-isothermal gas radiation scenarios. Many studies in the field of gas radiation within oxy-fuel

atmospheres, e.g. [18], [19], [41]–[45], have concluded that the FSCK model should be a good candidate for CFD software. Additionally, extensive research was conducted to improve the WSGG model parameters for oxy-fuel combustion [46]–[53] and were used to investigate the effects of oxy-fuel atmospheres on the radiation characteristics within furnaces of real sized power plants [54]–[57].

With regard to particle radiation, the Mie-theory is generally considered very accurate to model the non-gray radiative properties of coal/char and ash particles assuming a spherical shape, see e.g. [58]–[62], that are required to solve the RTE in a participating medium. Since calculating the scattering phase function with Mie-theory is computationally tedious and the scattering phase function in general varies rapidly with the scattering angle, the scattering phase function of the coal/char or ash particles is often assumed to be isotropic, or other simpler approximations are applied, like the Delta-Eddington approximation [63] or the Henyey-Greenstein function [64]. A very promising approach to model radiative transfer of gas-particle mixtures in disperse systems is the transport approximation [65], [66]. The application of the transport approximation for modelling the scattering phase function makes it possible to include the forward peak of the particle scattering phase function into the modified scattering coefficient yielding to the “transport” scattering and extinction coefficients of the gas-particle mixture. With these “transport” coefficients the resulting RTE can be expressed similarly to isotropic scattering.

For oxy-fuel combustion, Johansson et al. [67] concluded for a pulverized coal cylindrical enclosure that particle radiation strongly dominates radiative heat transfer. They considered isotropic scattering phase function, but used absorption and scattering coefficients obtained from Mie-theory. The benchmark solutions were calculated with a SNB model. It should be noted that the use of one averaged spectral absorption coefficient for each narrow-band derived from spectral transmissivities could introduce some errors, since the spectral absorption coefficient is a strong erratic function even within a narrow-band. Nakod et al. [68] conducted a CFD-study of a 300 MW oxy-fuel boiler and observed that the incident radiation on the walls was primarily influenced by gas radiation. They used a non-gray WSGG model in conjunction with constant particle radiative properties and anisotropic forward scattering phase functions. In contrast, Yin [69] confirms the findings of Johansson et al. [67] that particle radiation is dominant in a CFD-study of a 609 MW pulverized coal boiler with air-firing and hypothesizes that the same conclusions can be drawn for oxy-fuel conditions. He also applied a non-gray WSGG model with varying particle radiative properties for absorption and scattering coefficients, but no information is given about the employed phase functions for the particles.

Gronarz et al. [70] conducted a sensitivity analysis of different parameters influencing the radiative transfer within a plane several meters above the burner region in an oxy-coal boiler. Besides the pre-dominant particle radiation, one of their findings was that applying isotropic scattering phase functions showed a large deviation from the reference solution for the radiative source terms and net wall heat fluxes, whereas the use of Delta-Eddington approximations for the scattering phase functions was more accurate to describe the total radiative transfer. Additionally, the lower spectral resolution of the non-gray WSGG model in comparison to the SNB model was of minor importance. It should be noted that using the SNB model could introduce some errors, as mentioned before, and, thus, diminish the influence of the spectral resolution on the accuracy of the simulation results.

If Mie-theory is used to compute the particle radiative properties, the complex index of refraction is needed as an input material property for the particles. Johansson et al. [58] found that the refractive index for ash particles has a strong influence on the simulation results with differences of up to 10 % for the radiative source terms and 40 % for the net wall heat fluxes, depending on the experimental data used. From investigations of the absorption (the imaginary part of the refractive index) and refractive indices, constant values for coal/char particles seem to be sufficient, whereas a spectrally varying absorption index for ash particles should be considered, but no quantitative information was given on how large the differences could be in comparison with reference solutions for the radiative source terms and net wall heat fluxes. Additionally, they concluded that using the Sauter diameter instead of the full particle size distribution is sufficient. Furthermore, in a recent study of Johansson [71] an efficient treatment of the particle radiative properties was investigated including the optical limit, the anomalous limit and his proposed correlations for the absorption and scattering coefficients. The reference solutions were computed with a SNB model with Mie-theory and isotropic scattering as in [67], but for pulverized coal conditions with air-firing in a cylindrical enclosure. He concluded that applying a non-gray WSGG model together with the proposed gray correlations for the absorption and scattering coefficients yield errors of about 10 % for the radiative source terms and net wall heat fluxes, which is comparable to using gray particle radiative properties computed as the Planck-mean values from Mie-calculations. Hofgren et al. [72] investigated the accuracy of applying Planck-mean values for particle radiative properties in the WSGG context for fly-ash particles from coal and biomass. They concluded that parameter sets for combined gas and particle absorption coefficients and their corresponding weighting factors should be additionally derived rather than applying the Planck-mean values for particle absorption, since use of Planck-mean values yielded average errors up to 87 % for

the radiative source terms and 72 % for wall heat fluxes depending on the investigated test case. Guo et al. [73]–[75] subsequently obtained WSGG parameters for modelling gas, ash and coal radiation from full-spectrum k-distributions. The particle parameter sets are derived for different particle diameters, burnout, size distributions and temperatures and apply the “transport” approximation to account for the strong forward scattering peak. They found good agreement for particle radiation with benchmark results obtained from LBL calculations for 1D air and oxy-fuel combustion atmospheres with maximum relative errors of about 4 % and 15 % for radiative heat fluxes and source terms, respectively. Good agreement was reported for combined gas and particle radiation test cases.

## 1.2 Research objectives

The described state of the art on modelling radiative transfer in oxy-fuel combustion scenarios clarifies that there is still a need to investigate various radiation models, like narrow-band, wide-band and different global models, within the framework of real industrial burners to take into account the influence of real size dimensions and, thus, increasing pressure path lengths on the accuracy and validity of each radiation model and to compare each performance. Furthermore, the contribution of the gas and particle radiation on the total radiative transfer is still unclear. The investigated gas radiation model should be capable of accurately predicting the strongly erratic gas radiative properties on a narrow-band level and allow the consideration of particle radiative properties in a straightforward manner by applying the absorption and scattering coefficients as the main properties for the computational solution of the total radiative transfer. As a consequence, the impact of the spectral resolution on the accuracy of the predicted radiative source terms and net wall heat fluxes can be clarified by considering radiation models with less spectral resolution.

This doctoral thesis aims to provide answers to the aforementioned open questions and tries to give a recommendation for a radiative model, which can be used in CFD software to predict the radiative wall heat fluxes and source terms in different oxy-fuel combustion scenarios.

## 1.3 Thesis outline

The presented doctoral thesis has the following structure:

- Chapter 2 provides the basic theoretical background regarding the modelling of thermal radiation. The considered gas radiation models as well as particle radiation treatment are

introduced. Finally, the numerical procedures used to solve the radiative transfer equation are shortly described.

- Chapter 3 presents the numerical simulation results for various oxy-fuel combustion atmospheres. First, the accuracy and computational expense of different gas radiation models are assessed for a 3D dry oxy-fuel gas turbine combustor to investigate the influence of short path lengths and high pressures on the model performance. Afterwards, gas radiation modelling in a virtual 3D coal-fired furnace under air-fired, dry and wet oxy-fuel conditions at longer path lengths and atmospheric pressure is considered. Finally, the influence of gas and particle radiation is investigated for a 2D square geometry representing possible wet oxy-fuel combustion conditions in a coal-fired furnace.
- Chapter 4, the last chapter, finally summarizes the conclusions of this thesis and provides the outlook for possible future works.

## 2 Thermal radiation modelling

Thermal radiation is an overall encountered heat transfer phenomena, since every object emits electromagnetic waves of various frequencies depending on its temperature. In industrial boilers, it is the pre-dominant heat transfer mode. The reason for this is the non-linear temperature dependence of the radiative heat transfer, which is proportional to the power of four of the absolute temperatures of two objects exchanging radiative heat transfer, whereas conduction and convection heat transfer is generally linear proportional to the temperature difference of the two objects [76]–[78]. Another distinguishing characteristic is that radiative heat transfer is a global phenomenon, i.e. every location within a domain is also influenced by the radiation coming from all other locations within the considered domain. Additionally, for the exchange of radiative heat transfer no medium is required. The presence of gases and particulate matter, e.g. water vapor or carbon dioxide and coal/ash particles as in a coal-fired furnace, however does influence the heat transfer by radiation in the considered domain. To calculate this impact, the radiative transfer equation (RTE) for a participating medium has to be solved. To find a solution for this equation, radiative properties of the participating media have to be known and/or modelled. Thus, the following subsections first introduce the RTE and then describe the models used in this thesis to account for the radiation of gases and particles. Numerical methods solving the RTE are explained in the last sub-section. More detailed information can be found in the text books of Modest [77] and Howell [78], on which the next subsections rely on.

### 2.1 Radiative Transfer Equation

The spectral RTE for a participating medium describes the change of spectral radiative intensity  $I_\eta$  along an infinitesimal path  $ds$  in a considered direction  $\vec{s}$  for a wavenumber  $\eta$  due to absorption, emission and scattering of the medium:

$$\frac{dI_\eta}{ds} = \underbrace{(\kappa_{g,\eta} + \kappa_{p,\eta})I_{b,\eta}}_{\text{emission}} - \underbrace{\beta_\eta I_\eta}_{\text{absorption+ out-scattering}} + \underbrace{\frac{\sigma_{p,\eta}}{4\pi} \int_{4\pi} I_\eta(\vec{s}_i) \Phi_{p,\eta}(\vec{s}_i, \vec{s}) d\Omega_i}_{\text{in-scattering}} \quad (1)$$

where the spectral extinction coefficient  $\beta_\eta$  is defined as the sum of gas,  $\kappa_{g,\eta}$ , and particle absorption coefficients,  $\kappa_{p,\eta}$ , as well as the spectral particle scattering coefficient,  $\sigma_{p,\eta}$ :

$$\beta_\eta = \kappa_{g,\eta} + \kappa_{p,\eta} + \sigma_{p,\eta} \quad (2)$$

In Equation (1), the first term on the right-hand side represents the enhancement of radiative intensity due to emission. The spectral blackbody intensity  $I_{b,\eta}$  is calculated by Planck's law

$$I_{b,\eta} = \frac{2C_1\eta^3}{n^2[e^{C_2\eta/nT} - 1]} \quad (3)$$

with the two radiation constants  $C_1 = hc_0^2$  and  $C_2 = hc_0/k_B$ , computed with the speed of light in vacuum  $c_0$ , Planck's constant  $h$  and Boltzmann's constant  $k_B$ , the refractive index  $n$  and the local temperature  $T$  of the gas or particle. The second term accounts for the loss of radiative intensity due to absorption, and scattering in other directions than the one considered. The scattering of radiative intensity from a direction  $\vec{s}_i$  into the considered direction  $\vec{s}$  by the presence of particles is described by the third term, and its probability is given by the spectral phase function  $\Phi_{p,\eta}(\vec{s}_i, \vec{s})$ . To account for the contribution of each possible direction, the integration is carried out over the total solid angle of  $4\pi$  by considering each possible direction through its associated solid angle  $\Omega_i$ .

The spectral RTE in Equation (1) has to be solved to attain the radiative intensity at each location, for all directions and wavenumbers, so it can be used to compute the radiative energy flux onto a surface and within the domain of interest. Since the RTE is an integro-differential equation, numerical procedures have to be used to compute a solution, see Subsection 2.4.

Introducing the dimensionless optical thickness  $\tau_\eta$

$$\tau_\eta = \int_0^s \beta_\eta ds, \quad (4)$$

and the dimensionless single scattering albedo  $\omega_\eta$

$$\omega_\eta = \frac{\sigma_{p,\eta}}{\beta_\eta}, \quad (5)$$

Equation (1) can be re-written in non-dimensional form as

$$\frac{dI_\eta}{d\tau_\eta} = -I_\eta + (1 - \omega_\eta)I_{b,\eta} + \frac{\omega_\eta}{4\pi} \int_{4\pi} I_\eta(\vec{s}_i) \Phi_{p,\eta}(\vec{s}_i, \vec{s}) d\Omega_i. \quad (6)$$

This equation can be reduced in a more consolidated form by defining the last two terms as the source function  $S_\eta(\tau_\eta, \vec{s})$ :

$$\frac{dI_\eta}{d\tau_\eta} + I_\eta = S_\eta(\tau_\eta, \vec{s}). \quad (7)$$

A formal solution can be derived by multiplying Equation (7) with  $e^{\tau_\eta}$  and integrating the resulting equation from a point  $s' = 0$  at the wall to a point  $s' = s$  within the medium in the considered direction, resulting in:

$$I_\eta(\tau_\eta) = I_\eta(0)e^{-\tau_\eta} + \int_0^{\tau_\eta} S_\eta(\tau'_\eta, \vec{s})e^{-(\tau_\eta - \tau'_\eta)} d\tau'_\eta. \quad (8)$$

This equation can be solved by specifying an appropriate boundary condition at the wall. For a diffusely emitting and reflecting opaque surface, the boundary condition for the spectral intensity leaving the wall,  $I_{w,\eta}$ , is given as

$$I_{w,\eta}(\vec{s}) = \varepsilon_{w,\eta}I_{w,b,\eta} + \frac{\rho_{w,\eta}}{\pi} \int_{\vec{n}_w \cdot \vec{s}_i < 0} I_{w,\eta}(\vec{s}_i) |\vec{n}_w \cdot \vec{s}_i| d\Omega_i, \quad (9)$$

where  $\varepsilon_{w,\eta}$ ,  $\rho_{w,\eta}$  and  $\vec{n}_w$  are the spectral emissivity, spectral reflectivity and the outward normal vector of the wall and  $\vec{n}_w \cdot \vec{s}_i$  is the cosine of the angle between any incoming direction and the wall normal vector. In this work, only black walls are considered, i.e. the spectral wall emissivity is always unity, whereas the spectral wall reflectivity vanishes, so that Equation (9) reduces to:

$$I_{w,\eta}(\vec{s}) = I_{w,b,\eta}. \quad (10)$$

In the above equations, scattering by gas molecules is neglected being a good approximation for combustion processes. Additionally, the absorption and scattering by particles can be omitted in the former equations, if only gas radiation is considered.

For industrial boilers, the knowledge of the total radiative net wall heat fluxes and the total radiative source terms is important. The total radiative net wall heat fluxes,  $\vec{q}_w$ , are determined from the radiative intensity field as:

$$\vec{q}_w = \int_0^\infty \int_{4\pi} I_\eta(\vec{s}) \vec{n}_w \cdot \vec{s} d\Omega d\eta. \quad (11)$$

The total radiative source terms,  $\vec{\nabla} \cdot \vec{q}$ , which impact the conservation of the total energy, are calculated from:

$$\vec{\nabla} \cdot \vec{q} = \int_0^\infty (\kappa_{g,\eta} + \kappa_{p,\eta}) \cdot \left[ 4\pi I_{b,\eta} - \int_{4\pi} I_\eta d\Omega \right] d\eta. \quad (12)$$

## 2.2 Gas radiation modelling

Gas radiation is characterized by a strong erratic function of the spectral absorption coefficient along the considered spectral variable (e.g. wavenumber). Even within narrow spectral intervals of few wavenumber units, the spectral absorption coefficient can attain values varying within few orders of magnitude. For illustrative purpose, Figure 2 depicts the variation of the spectral gas absorption coefficient of water vapor along wavenumber for a partial pressure of 0.2 bar at total pressure of 1 bar and temperature of 1900 K. The reason for this behavior can be explained by quantum mechanics, modelling gas molecules as oscillators and rotators that can occupy only permissible quantized energy levels representing the vibrational-rotational state of each molecule. These allowed energy states dictate the appearance of spectral lines characterizing each atom and molecule, which contribute to the spectral absorption coefficient at a considered wavenumber.

To account for this non-gray behavior, many different (gas) radiation models were proposed, which especially differ in the spectral resolution for which the radiative properties are provided. In line-by-line (LBL) calculations, the spectral coefficient is calculated for spectral intervals with

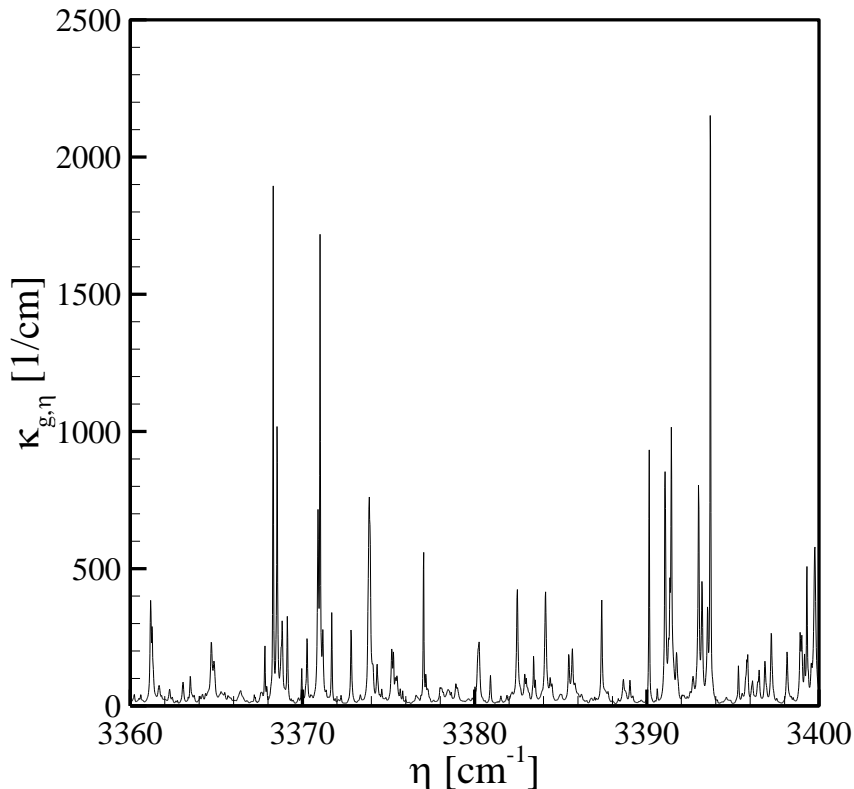


Figure 2: Absorption coefficients of water vapor along wavenumber for a partial pressure of 0.2 bar at total pressure of 1 bar and temperature of 1900 K obtained from own LBL calculations using the HITEMP 2010 spectroscopic database.

a very high resolution, typically in the order of  $0.01 \text{ cm}^{-1}$  [16], [23], [79], considering the possible contribution of all spectral lines for the spectral range of interest. The spectral line characteristics (e.g. line intensity, wavenumber location, line widths, etc.) are obtained from spectroscopic databases, like HITEMP 2010 [80]. The solution of the RTE given in Equation (1) with such resolution is computationally very expensive. Thus, simulation results of LBL calculations are generally obtained for rather academic test cases in 1D or 2D configurations and serve as benchmark solutions for the assessment of other radiation models. Narrow-band models subdivide the whole spectral range in spectral intervals with widths of 5 to  $25 \text{ cm}^{-1}$ , for which the blackbody intensity and particle radiative properties can be considered as constant. The spectral radiative intensity within each spectral interval is approximated with a mean value. This procedure reduces the computational effort, but the accuracy is close to LBL results [16], [20], [81]. A further reduction in computational effort is achieved by introducing the correlated-k methodology within the narrow-band framework [22], which enables the use of absorption based solution methods rather than tediously computing the transmissivity of gas columns with different lengths. Nevertheless, these models are still too expensive for engineering applications, since too many narrow-bands have to be considered. In wide-band models, the radiative characteristics of whole vibration-rotation absorption bands are approximated with correlations to account for the non-gray radiation behavior. These models furthermore reduce the computational time needed to solve the RTE, but depending on the underlying spectroscopic database can lead to higher uncertainties [43], [45] or are as accurate as narrow-band models [19]. A further reduction of computational expense can be achieved by using global radiation models such as the Weighted-Sum-of-Gray-Gases (WSGG) [30], [82], the spectral line-based WSGG (SLW) [31], the absorption-line blackbody distribution function (ADF) [83], the full-spectrum correlated-k [35] and other models [40], [84]. These models provide approximations of the total radiative properties, which are derived for the whole spectral range of interest. Thus, the spectral dependence is implicitly captured within those correlations, and the RTE is solved for a significantly reduced amount of global absorption coefficients. Especially, the WSGG model [30] is widely used in numerical simulations of engineering applications due to its simple implementation and low computational effort, see e.g. [55], [68], [85]–[87].

In the following subsections the gas radiation models used in this work are shortly described, which are also the most common models considered in literature to investigate gas radiation in oxy-fuel atmospheres.

### 2.2.1 Statistical Narrow-Band Model

In a Statistical Narrow-Band (SNB) model, the total spectral range under consideration is subdivided into narrow-bands with specified width  $\Delta\eta$ . The width  $\Delta\eta$  is sufficiently narrow that the assumptions of constant blackbody intensity and constant radiative particle properties within each narrow-band are valid. Nonetheless, the width is sufficiently wide to include enough absorption lines of the gas mixture to allow for a statistical treatment of the gas radiative properties. The aim is to provide a simple expression for the spectral averaged transmissivity of a gas column. In terms of gas absorption coefficient, the spectral averaged transmissivity  $\tau_{g,\Delta\eta}$  of a homogeneous gas column with specified length  $L$  is given as:

$$\tau_{g,\Delta\eta} = \frac{1}{\Delta\eta} \int_{\Delta\eta} e^{-\kappa_{g,\eta}L} d\eta. \quad (13)$$

Since the spectral gas absorption coefficient at a given wavenumber is attained from the sum of the contributions of all considered absorption lines within the specified narrow-band, the average transmissivity is expressed more generally as [21], [88]:

$$\tau_{g,\Delta\eta} = e^{-\bar{W}_l/\delta_l}, \quad (14)$$

where  $\bar{W}_l$  is a mean value of the equivalent black-line widths (depending on gas column length  $L$ ) and  $\delta_l$  the mean line spacing between two spectral lines within the specified narrow-band of the considered gas species  $l$ . In this work, the Malkmus SNB model [89] is used, since it is generally considered as most appropriate for polyatomic molecules [77]. The Malkmus SNB model assumes that the statistically uncorrelated spectral lines are randomly distributed within the narrow-band with random line strengths. However, one effective value of the line half-width at half-maximum  $\bar{\gamma}_l$  is assigned for each line and the line strengths are prescribed with an inverse exponential-tailed probability density function, see e.g. [88], [89]. Assuming a Lorentz shape for the spectral lines,  $\bar{W}_l$  can be expressed as:

$$\bar{W}_l = \delta_l \frac{2\bar{\gamma}_l}{\delta_l} \left( \sqrt{1 + \frac{Y_l p L \bar{k}_l \delta_l}{\bar{\gamma}_l}} - 1 \right), \quad (15)$$

with total pressure  $p$ , mole fraction of considered gas species  $Y_l$ , weighted mean spacing between two consecutive lines  $\bar{\delta}_l$  and ratio of mean line strength to mean line spacing  $\bar{k}_l$ . Thus, the spectral averaged transmissivity can be expressed as:

$$\tau_{g,\Delta\eta} = \exp \left[ \frac{\bar{\beta}_l}{\pi} \left( \sqrt{1 + \frac{2\pi Y_l p L \bar{k}_l}{\bar{\beta}_l}} - 1 \right) \right]. \quad (16)$$

Here, the mean line overlapping parameter is defined as:

$$\bar{\beta}_l = \frac{2\pi\bar{\gamma}_l}{\delta_l} \quad (17)$$

$\bar{\beta}_l$  and  $\bar{k}_l$  represent the parameters of the SNB model. In this work, the SNB parameters of the updated SNB database of Rivière and Soufiani [81] are used to calculate the spectral averaged gas transmissivities of water vapor and carbon dioxide for radiative transfer calculations. The updated SNB database comprises in total 450 narrow-bands for each radiating gas species (CO<sub>2</sub> and H<sub>2</sub>O) in the spectral wavenumber range between 12.5 and 11262.5 cm<sup>-1</sup> with a bandwidth  $\Delta\eta$  of 25 cm<sup>-1</sup>. The classical Curtis-Godson approximation [88], [90], [91] is applied to compute the spectral averaged gas mixture transmissivity for inhomogeneous gas columns.

The SNB model is used in this work solely for the solution of the radiative transfer equation presented in Equation (8) for combustion scenarios where only gas radiation is present. Since the transmissivity is the radiative property needed to obtain the radiative intensity field, a ray-tracing type of solution procedure is applied. This procedure is explained in subsection 2.4.1. The expansion of the SNB model to scattering media was introduced by Johansson et al. [67]. If the contribution of gas radiation is similar to the contribution given by particles, this expansion possibly incorporates errors. The reasons lie within the definition of the scattering albedo, Equation (5), since the gas absorption coefficient is needed to compute this quantity. SNB models, however, consider the spectral averaged transmissivity as the radiative property of choice, which is dependent on the column thickness. Thus, the resulting spectral averaged gas absorption coefficient will be dependent on the applied grid size using Beer's law. Furthermore, gas absorption will be considered by only one averaged value for the specified narrow-band. With regard to Figure 2, this characteristic can introduce a further error. Due to these uncertainties, in this work only solution procedures applying the absorption coefficient are used to investigate radiative transfer in absorbing-scattering media.

### 2.2.2 Narrow-Band Correlated-k

As for the SNB model, in the Narrow-Band Correlated-k (NBCK) model the considered spectral range is discretized in narrow-bands, in which the blackbody intensity and particle radiative properties are essentially constant. As depicted exemplary in Figure 2, the absorption coefficient of water vapor exhibits a strong erratic behavior with respect to wavenumber even in the narrow wavenumber interval between 3360 and 3400 cm<sup>-1</sup>. Additionally, the absorption coefficient attains the same value multiple times, and, thus, the solution of the RTE would yield

the same radiative intensity each time. Therefore, the idea of the NBCK model is to reorder the absorption coefficient in each narrow-band to generate a monotonically increasing function, the narrow-band k-g distribution, with regard to a cumulative distribution function  $g^{NB}$ .

As illustrated in Figure 3 by the red curve, this is accompanied by first introducing the absorption coefficient distribution function  $f^{NB}(\underline{\phi}_0, k_l)$ :

$$f^{NB}(\underline{\phi}_0, k_l) = \frac{1}{\Delta\eta} \int_{\Delta\eta} \delta[k_l - \kappa_{g,\eta}(\underline{\phi}_0)] d\eta, \quad (18)$$

where  $\underline{\phi}_0$  denotes a set of variables at a reference state (namely the mole fractions of the radiative participating gas species, total pressure, and temperature) that affect the absorption coefficient of the gas phase,  $k_l$  is a distinct value of the absorption coefficient,  $\Delta\eta$  the narrow-band width and  $\delta[k_l - \kappa_{g,\eta}(\underline{\phi}_0)]$  the Dirac-delta function. Physically,  $f^{NB}$  represents the probability that the gas absorption coefficient  $\kappa_{g,\eta}$  attains a value within the infinitesimal interval of  $k_l$  and  $k_l + dk_l$ . Since the distribution function still shows poor characteristics for numerical handling (erratic function with values tending to infinity due to minima and maxima

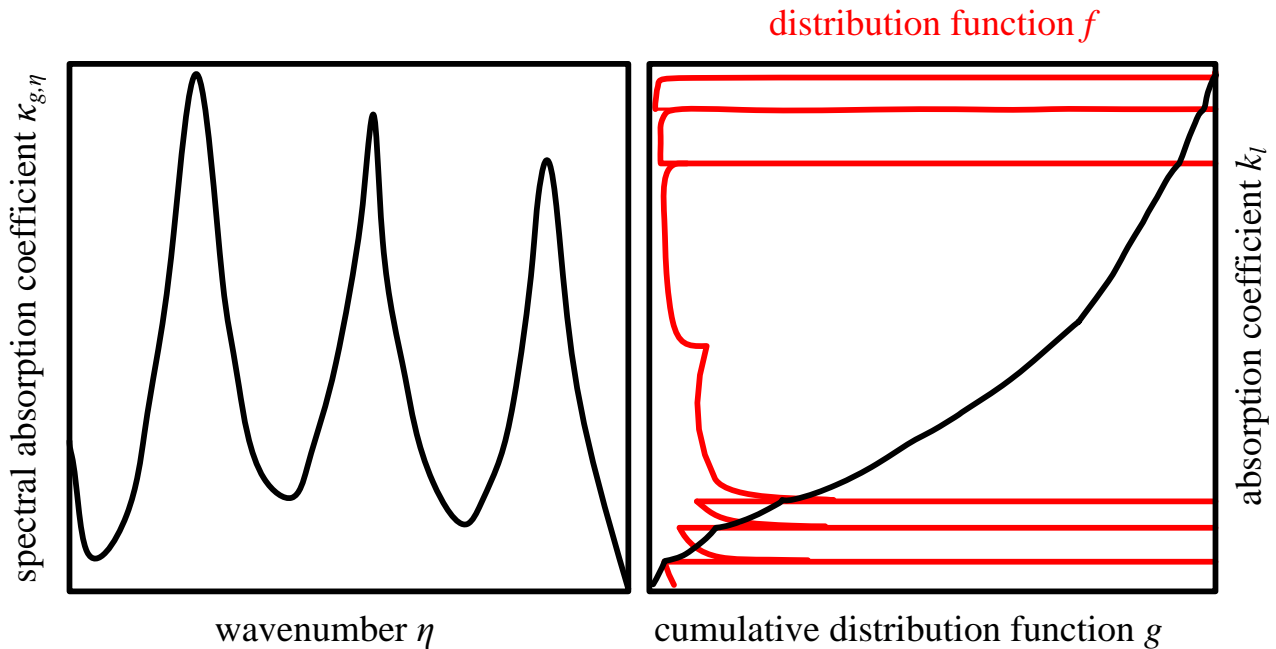


Figure 3: Illustration of correlated-k methodology within narrow-band context; adopted from [77], p. 337

of the original gas absorption values at distinct wavenumbers), the cumulative distribution function  $g^{NB}(\underline{\phi}_0, k_l)$  is considered:

$$g^{NB}(\underline{\phi}_0, k_l) = \int_0^{k_l} f^{NB}(\underline{\phi}_0, k'_l) dk'_l = \frac{1}{\Delta\eta} \int_{\Delta\eta} H[k_l - \kappa_{g,\eta}(\underline{\phi}_0)] d\eta. \quad (19)$$

Here,  $H[k_l - \kappa_{g,\eta}(\underline{\phi}_0)]$  is the Heaviside's unit step function.  $g^{NB}$  can be interpreted as the fraction of the narrow-band, where the absorption coefficient  $\kappa_{g,\eta}$  is smaller than the value of  $k_l$ . Thus, the averaged spectral intensity over a narrow-band,  $I_{\Delta\eta}$ , can be obtained through an integral over  $g^{NB}$  rather than over the wavenumber:

$$I_{\Delta\eta} = \frac{1}{\Delta\eta} \int_{\Delta\eta} I_\eta d\eta = \int_0^1 I_g dg^{NB}, \quad (20)$$

where

$$I_g = \frac{1}{\Delta\eta} \int_{\Delta\eta} I_\eta \delta[k_l - \kappa_{g,\eta}(\underline{\phi}_0)] d\eta / f^{NB}(\underline{\phi}_0, k_l). \quad (21)$$

The following RTE has to be solved to obtain each  $I_g$ :

$$\frac{dI_g}{ds} = [k_g^*(\underline{\phi}, g^{NB}) + \kappa_{p,\Delta\eta}] I_{b,\Delta\eta} - \beta_{\Delta\eta} I_g + \frac{\sigma_{p,\Delta\eta}}{4\pi} \int_{4\pi} I_g(\vec{s}_i) \Phi_{\Delta\eta}(\vec{s}_i, \vec{s}) d\Omega_i. \quad (22)$$

If only gas radiation is taken into account, Equation (22) reduces to:

$$\frac{dI_g}{ds} = k_g^*(\underline{\phi}, g) [I_{b,\Delta\eta} - I_g]. \quad (23)$$

A formal development of Equations (22) and (23) can be found in [92] and [77]. The correlated-k assumption states that at every wavenumber where the spectral gas absorption coefficient for a reference state,  $\kappa_{g,\eta}(\underline{\phi}_0)$ , has one and the same value  $k$ , the spectral gas absorption coefficient for the local state,  $\kappa_{g,\eta}(\underline{\phi})$ , always also has one unique value  $k_g^*(\underline{\phi}, g^{NB}(\underline{\phi}_0, k_l))$ , which may be a function of  $k_l$  but not the wavenumber  $\eta$  [93]. Thus, it can be shown that both  $k_l$  and  $k_l^*$  can be calculated from the same cumulative distribution function, since the following relation is valid:

$$g^{NB}(\underline{\phi}_0, k_l) = \int_0^{k_l} f^{NB}(\underline{\phi}_0, k'_l) dk'_l = \int_0^{k_l^*} f^{NB}(\underline{\phi}, k'_l) dk'_l = g^{NB}(\underline{\phi}, k_l^*). \quad (24)$$

Through inversion of Equation (24), the corresponding absorption variables  $k_l^*$  and  $k_l$  are obtained.

Since  $g^{NB}$  is a monotonically increasing function, the integral in Equation (20) can be calculated numerically with a Gauss-Legendre quadrature scheme at specified quadrature points  $g_G^{NB}$  and their associated weights  $w_G$ :

$$I_{\Delta\eta} = \sum_{G=1}^{N_G} I_{g,G} w_G g_G^{NB}, \quad (25)$$

where  $N_{Gi}$  is the order of the quadrature scheme. In this work, a Gauss quadrature scheme of 7<sup>th</sup> order is used. The total intensity, and analogously the total radiative net wall heat flux and source term (Equations (11) and (12)), is approximated as

$$I = \sum_{\Delta\eta} I_{\Delta\eta}. \quad (26)$$

In the Statistical Narrow-Band Correlated-k (SNBCK) model, the fact is used that the absorption coefficient distribution function  $f^{NB}$  can be mathematically interpreted as the inverse Laplace transform of the spectral averaged transmissivity of the considered narrow-band. Domoto [94] derived a simple closed form of  $f^{NB}$  for the Malkmus SNB model [89] and Lacis and Oinas [22] provided the following expression of its  $g^{NB}$

$$g^{NB}(\phi_0, k_l) = \frac{1}{2} \operatorname{erfc} \left[ \frac{\sqrt{\bar{\beta}_l}}{2} \left( \sqrt{\frac{\bar{k}_l}{k_l}} - \sqrt{\frac{k_l}{\bar{k}_l}} \right) \right] + \frac{1}{2} e^{\bar{\beta}_l} \operatorname{erfc} \left[ \frac{\sqrt{\bar{\beta}_l}}{2} \left( \sqrt{\frac{\bar{k}_l}{k_l}} + \sqrt{\frac{k_l}{\bar{k}_l}} \right) \right], \quad (27)$$

where  $\bar{\beta}_l$ ,  $\bar{k}_l$  are the SNB parameters given in Equations (15) and (17) and  $\operatorname{erfc}$  the complementary error function. Thus, a SNB parameter database can be applied to calculate  $g^{NB}$  for specified reference states and the according  $k - g^{NB}$  distribution functions are obtained through inversion of Equation (27).

To accelerate the solution procedure of the NBCK model, a narrow-band  $k - g^{NB}$  distribution database (NBKD) is used in this work. This database was generated from the SNB database of Rivière and Soufiani [81], considering in total 450 narrow-bands for each radiating gas species (carbon dioxide and water vapor) in the spectral wavenumber range between 12.5 and 11262.5  $\text{cm}^{-1}$  with a bandwidth  $\Delta\eta$  of 25  $\text{cm}^{-1}$ . The applied NBKD comprises pre-generated narrow-band  $k - g^{NB}$  distributions for six mole fractions (0, 0.1, 0.25, 0.5, 0.75 and 1.0) of  $\text{CO}_2$  and  $\text{H}_2\text{O}$ , 38 temperatures ranging between 300 and 4000 K (by a uniform temperature step of

100 K) and stored for 100 values of  $g^{NB}$  corresponding to a 100-point Gauss quadrature scheme.

For the solution of the narrow-band RTE, Equations (22) and (23), the blackbody intensity and the particle radiative properties are evaluated at the center of the considered narrow-band. The local absorption coefficient of the gas phase is obtained from the NBKD by carrying out linear interpolations on the mole fraction and spline interpolations on the temperature. If a gas mixture is present, a mixed  $k_{mix} - g_{mix}^{NB,g}$  distribution is then computed by applying the mixing scheme of Modest and Riazzi [37], which was derived from the assumption that the transmissivity of a mixture is the product of the transmissivities of each gas species in the mixture:

$$\begin{aligned} g_{mix}^{NB,g}(\underline{\phi}, k_{mix}) &= \int_{g_{H_2O}=0}^1 \int_{g_{CO_2}=0}^1 H[k_{mix} - (k_{CO_2} + k_{H_2O})] dg_{CO_2} dg_{H_2O} \\ &= \int_{g_{H_2O}=0}^1 g_{CO_2}(k_{mix} - k_{H_2O}) dg_{H_2O} \end{aligned} \quad (28)$$

### 2.2.3 Wide-Band Correlated-k based on spectroscopic database HITEMP 2010

The wide-band correlated-k model based on the spectroscopic database HITEMP 2010 (denoted as WBCK\_2010 hereafter) is similar to the NBCK model described in the former subsection, but with a significantly lower resolution regarding the discretization of the spectral range. In this work, the following spectral decomposition is applied with a total amount of  $N_{WB} = 17$  wide-bands: 1 wide-band of  $250 \text{ cm}^{-1}$  width between  $12.5$  and  $262.5 \text{ cm}^{-1}$ , 10 wide-bands of  $500 \text{ cm}^{-1}$  width between  $262.5$  and  $5262.5 \text{ cm}^{-1}$ , and 6 wide-bands of  $1000 \text{ cm}^{-1}$  width between  $5262.5$  and  $11262.5 \text{ cm}^{-1}$ . In each wide-band, the blackbody intensity and particle radiative properties are assumed to be constant and are evaluated at the wide-band centers, although this assumption is expected to become less valid in comparison with the narrow-band models.

A specific database of mixed wide-band k-distributions (WDKD) is used, which is generated from the NBKD database described in Subsection 2.2.2 by using a lumping strategy [19]:

$$g_i^{WB,g}(\underline{\phi}, k) = \sum_{j=1}^{NB_i} \frac{\Delta\eta_{NB,j}}{\Delta\eta_{WB}} g_j^{NB,g}(\underline{\phi}, k), \quad (29)$$

where  $NB_i$  is the number of narrow-bands within the  $i^{th}$  wide-band.  $g_i^{WB,g}$  and  $g_j^{NB,g}$  are the cumulative  $k$ -distributions over the  $i^{th}$  wide-band and the  $j^{th}$  narrow-band, respectively, of the considered gas species. The gas mixture is treated at the narrow-band level by using the mixing scheme developed by Modest and Riazzi [37], see Equation (28). For each lumped wide-band, the absorption coefficients of specified  $CO_2$ - $H_2O$  mixtures, computed from the NBKD database of known mole fractions, are stored in the WDKD database at the 7 Gauss points used to solve the wide-band RTE. At each computational grid node, for each wide-band and quadrature point, the absorption coefficient required to solve the wide-band RTE is extracted from the WBKD database by using linear interpolations on  $Y_{CO_2}$  and  $Y_{H_2O}$  and a spline interpolation on  $T$ .

#### 2.2.4 Full-Spectrum Correlated-k Model

Similar to the NBCK and the WBCK\_2010 models, in the full-spectrum correlated-k model (FSCK) the spectral absorption coefficients are rearranged to yield a monotonic increasing function of the absorption coefficient values with respect to the cumulative distribution function. Since the FSCK model is a global model, considering averaged radiative properties for the whole spectral range of interest, the assumptions of constant blackbody intensity and constant particle radiative properties across the whole wavenumber range are not valid. Thus, a full-spectrum  $k$  distribution function weighted with the Planck blackbody function defined as:

$$f(T, \underline{\phi}, \underline{\phi}_s, k) = \int_0^\infty I_{b\eta}(T) \delta[k - \kappa_\eta(\underline{\phi}, \underline{\phi}_s)] d\eta \bigg/ \int_0^\infty I_{b\eta}(T) d\eta \quad (30)$$

and a full-spectrum Planck-function weighted cumulative  $k$ -distribution defined as:

$$g(T, \underline{\phi}, \underline{\phi}_s, k) = \int_0^k f(T, \underline{\phi}, \underline{\phi}_s, k') dk', \quad (31)$$

are introduced. Here,  $\underline{\phi}_s$  is a set of state variables that affect the absorption coefficient of the solid phase. The spectral absorption coefficient considered in Equation (30),  $\kappa_\eta = \kappa_{g,\eta} + \kappa_{p,\eta}$ , includes the contributions from both the gas and solid phases. The resulting full-spectrum RTE and the spectrally integrated intensity,  $I$ , are expressed as [37]:

$$\frac{dI_g}{ds} + [k^*(T_0, \underline{\phi}, \underline{\phi}_s, g_0) + \sigma_p] I_g = k^*(T_0, \underline{\phi}, \underline{\phi}_s, g_0) a(T, T_0, g_0) I_b(T) + \frac{\sigma_p}{4\pi} \int_{4\pi} \Phi_p I_g d\Omega' \quad (32)$$

$$I = \int_0^1 I_g, \quad (33)$$

where the subscript 0 refers to the reference state,  $I_b = \frac{\sigma_{SB} T^4}{\pi}$  designates the total blackbody intensity at local temperature  $T$  with the Stefan-Boltzmann constant  $\sigma_{SB}$ , and  $I_g$  is defined as:

$$I_g = \int_0^\infty I_\eta \delta(k - \kappa_\eta) / f(T, \underline{\phi}, \underline{\phi}_s, k). \quad (34)$$

It is noted that  $f$  and  $g$  are dependent on the temperature at which the blackbody function is evaluated. Since both functions are derived for a reference state, the following weighting function

$$a(T, T_0, g_0) = \frac{dg(T, \underline{\phi}_0, \underline{\phi}_{s,0}, k)}{dg(T_0, \underline{\phi}_0, \underline{\phi}_{s,0}, k)} \quad (35)$$

is introduced in the FSCK context to take the difference in local and reference temperature into account. Considering a black surface, the following boundary conditions are given at the enclosing surfaces:

$$I_g = I_{wg} = a_w(T_w, T, g) I_{bw}. \quad (36)$$

As indicated in Equation (32), scattering properties (scattering coefficients and phase functions) of the particle phases are treated as gray. This assumption is acceptable even for extremely non-gray scatters, as was demonstrated by Modest and Riazzi [37] who considered gray (Planck-mean) scattering coefficients and phase functions. The definition of Planck-mean scattering coefficient and phase function is given in Section 2.3.4.

Since the computation of full-spectrum k-distributions is very time consuming, the full-spectrum k-distributions are generated from the NBKD database described in Section 2.2.2. The procedure is the same as the one for the NBCK method up to the stage where narrow-band  $g_{mix}^{NB,g} - k_{mix}$  distributions are obtained. The narrow-band k-distribution of the gas-particle mixture ( $g_{mix}^{NB,g-p} - k_{mix}$ ) is then computed by adding the narrow-band solid absorption coefficients of all solid phases to the narrow-band gas k-distribution over each narrow-band [37]. The full-spectrum  $g_{mix}^{FS,g-p} - k_{mix}$  distributions are then assembled from the narrow-band  $g_{mix}^{NB,g-p} - k_{mix}$  distributions by using the following relationship [37]:

$$g_{mix}^{FS,g-p}(T, \underline{\phi}, \underline{\phi}_s, k_{mix}) = \sum_{j \in [all\ NBs]} \frac{I_{bj}(T)}{I_b(T)} g_{mix}^{NB,g-p}(T, \underline{\phi}, \underline{\phi}_s, k_{mix}) \quad (37)$$

In this study, a 10-point Gauss quadrature scheme is used for integration over the g-space. The reference state is defined by the mole fractions of the gas species (CO<sub>2</sub> and H<sub>2</sub>O) and the cross-sectional area per volume of the coal/char and ash particles each averaged over the flame volume. The reference temperature is calculated as the blackbody emission weighted temperature including the contributions of gas and solid phases [77]. The extension of this scheme to a multi-temperature medium can be found in the work of Cai and Modest [95].

### 2.2.5 Weighted-Sum-of-Gray-Gases Model

The idea of the WSGG model is to approximate the non-gray radiative characteristics of the gas-particle mixture by a mixture of few gray gas-particle phases and one transparent gas. The transparent gas accounts for the spectral windows, where no absorption of the gas phase takes place. For each gray gas-particle phase  $k$ , the following RTE has to be solved (if gray particle scattering is assumed):

$$\frac{dI_k}{ds} = a_{gp,k}\kappa_{gp,k}I_b - (\kappa_{gp,k} + \sigma_p)I_k + \frac{\sigma_p}{4\pi} \int_{4\pi} I_k(\vec{s}_i)\Phi_p(\vec{s}_i, \vec{s})d\Omega_i, \quad (38)$$

where  $a_{gp,k}$ ,  $\kappa_{gp,k}$ ,  $\sigma_p$  and  $\Phi_p$  are the gray weighting factors and absorption coefficients of gases and particles, gray particle scattering coefficient and gray particle phase function. The weighting factor  $a_{gp,k}$  represents the fraction of the total blackbody intensity for which the absorption coefficient attains the values of  $\kappa_{gp,k}$ . In the following description only non-gray gas radiation will be considered, thus, Equation (38) reduces to [30]:

$$\frac{dI_k}{ds} = \kappa_{g,k}(a_{g,k}I_b - I_k). \quad (39)$$

To solve Equation (39), parameter sets for  $\kappa_{g,k}$  and  $a_{g,k}$  are needed. These parameter sets are traditionally derived by fitting total emissivity data. Generally, this emissivity data is either computed, e.g. from a high-resolution spectroscopic database like HITEMP 2010 [80], or obtained from experimental data. For this purpose, the total emissivity  $\varepsilon$ , for a given path length  $L$  at a temperature  $T$ , is approximated in the WSGG context as a weighted sum of gray gases:

$$\varepsilon(L, T) = \sum_{k=0}^K a_{g,k}(T) \cdot [1 - e^{-\kappa_{g,k}L}], \quad (40)$$

where  $K$  is the number of considered gray gases. The weighting factors are approximated by a polynomial function of temperature as

$$a_{g,k}(T) = \sum_{l=1}^L b_{g,k,l} \left( \frac{T}{T_0} \right)^{l-1}. \quad (41)$$

Here,  $b_{g,k,l}$ ,  $T_0$  and  $L$  (generally  $L = 3$ ) are the polynomial coefficients, reference temperature and order of the polynomial function. Since Kirchhoff's law states that the absorptivity  $\alpha(L, T)$  equals the emissivity  $\varepsilon(L, T)$  and for an infinitely thick medium ( $\kappa_{g,k}L \rightarrow \infty$ ) the absorptivity approaches unity, the sum of the weighting factors yields unity for this approximation:

$$\sum_{k=0}^K a_{g,k} = 1. \quad (42)$$

This relation is used to compute the weighting factor  $a_{g,0}$  of the transparent gas (for which  $\kappa_{g,k} = 0$ ):

$$a_{g,0} = 1 - \sum_{k=1}^K a_{g,k}. \quad (43)$$

A commonly used parameter set for air-fired combustion scenarios in commercial CFD software was derived by Smith et al. [82], denoted as “WSGG4\_Smith” hereafter. They considered three gray gases and one transparent gas, where a polynomial function of order three was used to approximate the weighting factors, applying 1 K as the reference temperature in Equation (41). The parameter set is valid for a temperature range between 600 and 2400 K, pressure path lengths of 0.001–10 atm m, fixed H<sub>2</sub>O to CO<sub>2</sub> molar ratios ( $MR = Y_{H_2O}/Y_{CO_2}$ ) of 1 and 2, for vanishing mole fractions of H<sub>2</sub>O and CO<sub>2</sub>, and for pure water vapor. The total emissivities for the fitting procedure were computed with the exponential wide-band model (EWBM) [25]. Yin [96], referred to as “WSGG5\_Yin2013” hereafter, further refined the WSGG parameter set for air-combustion processes by deriving appropriate parameters for temperatures between 500 and 3000 K and pressure path lengths of 0.001–60 atm m. Besides the mole fractions considered by Smith et al. [82], a fixed H<sub>2</sub>O to CO<sub>2</sub> molar ratio of 0.005 and a H<sub>2</sub>O mole fraction of 0.05 were included. A value of 1200 K was chosen as the reference temperature to obtain the polynomial coefficients in Equation (41) for a polynomial function of third order to enhance the accuracy of the gained coefficients. Furthermore, the non-gray gas is approximated with four gray gases and one transparent gas, and the total emissivity data were computed with the EWBM. In this work, a linear interpolation is applied to calculate the absorption coefficients and weighting factors of the WSGG4\_Smith and WSGG5\_Yin2013 parameter sets for the investigated molar ratios. The proposed stepwise interpolation [96] for

the WSGG5\_Yin2013 model is not used, since it yielded unphysical oscillations of the radiative intensity if the investigated molar ratios were close to the transition values of the proposed stepwise procedure.

Since oxy-fuel combustion atmospheres are characterized by much higher concentrations of the radiative participating gases CO<sub>2</sub> and H<sub>2</sub>O, much effort has recently been put into deriving new gas parameter sets for the WSGG model. Yin et al. [48], designated as “WSGG5\_Yin2010” hereafter, created emissivity charts from the EWBM for six fixed H<sub>2</sub>O to CO<sub>2</sub> molar ratios and provided WSGG parameters applicable for temperatures between 500 and 3000 K and pressure path lengths ranging from 0.001 to 60 atm m. To account for the influence of a variable distribution of the H<sub>2</sub>O to CO<sub>2</sub> molar ratio (between 0.125 and 2) on the WSGG parameters ( $\kappa_{g,k}$  and  $a_{g,k}$ ), Johansson et al. [49] derived a parameter set to compute the absorption coefficients and weighting factors as functions of the molar ratio  $MR$ . Here,  $\kappa_{g,k}$  is approximated as a linear function of  $MR$

$$\kappa_{g,k} = K1_{g,k} + K2_{g,k}MR \quad (44)$$

and  $b_{g,k,l}$  are expressed as quadratic functions of  $MR$

$$b_{g,k,l} = B1_{g,k,l} + B2_{g,k,l}MR + B3_{g,k,l}MR^2. \quad (45)$$

The non-gray radiative gas mixture is approximated with four gray gases and one transparent gas. The associated parameter set will be denoted as “WSGG5\_Johansson” hereafter and is applicable for a temperature range of 500 to 2500 K and pressure path lengths between 0.01 to 60 bar m. The emissivities for the fitting procedure were obtained from a SNB model with the EM2C 1997 spectroscopic database [97]. Kangwanpongpan et al. [51] conducted LBL calculations with spectral line data from the spectroscopic database HITEMP 2010 to compute emissivity data for a broader temperature (400–2500 K), molar ratio (0.125–4) and pressure path length range (0.001–60 bar m). The provided WSGG parameter set for four gray gases and one transparent gas, denoted as “WSGG5\_Kangwanp” from here on, additionally approximates the dependence of  $\kappa_{g,k}$  from  $MR$  as a quadratic function. Similarly, Bordbar et al. [53] created emissivity charts obtained from LBL calculations applying the HITEMP 2010 spectroscopic database and used polynomial functions of fourth order to model the molar ratio dependence of  $\kappa_{g,k}$  and  $b_{g,k,l}$ . The derived parameter set for four gray gases and one transparent gas, referred as “WSGG5\_Bordbar” hereafter, is valid for a temperature range between 500 and 2400 K, pressure path lengths from 0.01 to 60 bar m and a broader molar ratio range of 0.01 to 4.

The weighting factors  $a_{g,k}$  in Equation (41) are computed with a reference temperature of 1200 K when the parameter sets of the WSGG5\_Yin2010, WSGG5\_Johansson and WSGG5\_Bordbar models are used, whereas  $T_0 = 2000 \text{ K}$  is applied in the WSGG5\_Kangwanp implementation.

Cassol et al. [98] used the “multiplication” approach to derive separate parameter sets for H<sub>2</sub>O and CO<sub>2</sub> (and soot), which are each valid for temperatures between 400 and 2500 K, partial pressure path lengths from 0.001 to 10 bar m and, in consequence, for molar ratios ranging between 0.001 and 1000. In this approach, designated as “WSGG25\_Cassol” hereafter, the local absorption coefficient of the gas mixture is calculated as the sum of each radiating gas:

$$\kappa_{g,k} = \kappa_{H_2O,k_{H_2O}} + \kappa_{CO_2,k_{CO_2}}, \quad (46)$$

and the local weighting factor is evaluated as the product of weighting factors of each gas species:

$$a_{g,k} = a_{H_2O,k_{H_2O}} \times a_{CO_2,k_{CO_2}}, \quad (47)$$

Each gas species is approximated by four gray gases and one transparent gas, thus, in total 25 RTEs, as given in Equation (39), have to be solved for a medium containing two radiating gases.  $T_0 = 1 \text{ K}$  is used to obtain the weighting factors of each gas species with Equation (41). In Table 1 an overview of the major differences of the considered WSGG gas parameter sets is given.

A commonly used form of the WSGG model in computational fluid dynamics simulations is the gray WSGG model, abbreviated as “WSGG1\_Smith” hereafter. Here, the gas mixture is considered as gray rather than a sum of gray gases. The mean absorption coefficient is computed from Beer’s law by restating Equation (40) as

$$\kappa_{g,mean} = -\frac{\ln(1 - \varepsilon)}{L_{mean}}, \quad (48)$$

where the mean path length  $L_{mean} = 3.6 V/A$  is obtained with the volume  $V$  and the surface area  $A$  of the considered enclosure and the total emissivity is calculated via Equation (40) with the parameters of Smith et al. [82] in this work.

**Table 1: Major differences in the parameter sets of representative WSGG models for temperature range, H<sub>2</sub>O to CO<sub>2</sub> molar ratios, pressure path lengths, number of considered gray gases and the source of the reference total gas emissivity [43]**

Parameter set	Temperature (K)	H <sub>2</sub> O/CO <sub>2</sub> molar ratio	Pressure path length (bar m)	Number of gray gases	Source of the reference total gas emissivity
WSGG4_Smith	[600, 2400]	1, 2	[0.001, 10]	3+1	EWBM
WSGG5_Yin2010	[500, 3000]	0.125, 0.25, 0.75, 1, 2, 4	[0.001, 60]	4+1	EWBM
WSGG5_Johansson	[500, 2500]	[0.125, 2]	[0.01, 60]	4+1	SNB EM2C 1997
WSGG5_Kangwanp	[400, 2500]	[0.125, 4]	[0.001, 60]	4+1	LBL HITEMP 2010
WSGG5_Yin2013	[500, 3000]	0.05, 1, 2	[0.001, 60]	4+1	EWBM
WSGG5_Bordbar	[500, 2400]	[0.01, 4]	[0.01, 60]	4+1	LBL HITEMP 2010
WSGG25_Cassol	[400, 2500]	[0.001, 1000]	[0.001, 10]	(4+1)×(4+1)	LBL HITEMP 2010

### 2.2.6 Wide-Band Correlated-k Model based on Exponential Wide-Band Model

The wide-band correlated-k model based on the exponential wide-band model (EWBM) is similar to the WBCk\_2010 model with respect to the common characteristic that the reordering mechanism of the absorption coefficients is performed along an artificial wavenumber for entire wide-bands. The major difference lies in applying the EWBM model parameters and its database rather than employing the spectroscopic database HITEMP 2010 to compute the trend of the absorption coefficient along wavenumber for the considered gases.

In the EWBM, see e.g. [25], [99], the fact is used that spectral absorption and emission of thermal radiation occur particularly in certain distinct vibration-rotation bands for radiating gas species. Each of these vibration-rotation bands is considered as one wide-band. However, not the spectral lines within each wide-band are considered, but the mean line strength to spectral line spacing ratio,  $S/\delta_{EWBM}$ , of the whole wide-band is approximated with one of three possible exponential functions. These three functions allow the modelling of the assumed trend of  $S/\delta_{EWBM}$  for wide-bands with band heads positioned in the wavenumber spectrum at a lower limit  $\eta_l$ , upper limit  $\eta_u$ , or in the band center  $\eta_c$ :

$$\frac{S}{\delta_{EWBM}} = \begin{cases} \frac{\alpha}{\omega} e^{-(\eta-\eta_l)/\omega} & (\text{lower limit}) \\ \frac{\alpha}{\omega} e^{-(\eta_u-\eta)/\omega} & (\text{upper limit}) \\ \frac{\alpha}{\omega} e^{-2|\eta_c-\eta|/\omega} & (\text{center}) \end{cases} \quad (49)$$

Here, the EWBM model parameters  $\alpha$  and  $\omega$  denote the integrated band intensity and the bandwidth parameter of the considered wide-band, respectively. The total band absorption of each wide-band is computed with the line width to spacing ratio  $\beta$ , the third EWBM parameter taking into account possible line overlapping within the considered wide-band. Edwards and Menard [29] provided asymptotic relations for total band absorption, the “four-region approximation”, in terms of non-dimensional total band absorption with respect to the line width to spacing ratio and optical thickness at the band head. The EWBM model utilizes the transmissivity of a wide-band for solving the RTE given by Equation (8) with a ray-tracing type solution procedure, similar to the one described in sSubsection 2.4.1, which is very time consuming. To reduce the computational effort, a reordering scheme of the absorption coefficient within a wide-band is needed to apply an absorption coefficient-based solution algorithm for the RTE, as described in Subsections 2.4.2 and 2.4.3. In this work, the correlation of Denison and Fiveland [100] is used to reorder the wavenumber around the band head. They proposed the following equation for the dimensionless wavenumber  $\xi^* = \xi/\omega$ , which best fitted the “four-region approximation”:

$$\xi^*(\kappa^*) = \sum_{i=1}^{n_p} C_{i,1} E_1(p_i \kappa^*) + C_{1,2} \frac{e^{-p_1 \kappa^*}}{p_1}. \quad (50)$$

Here,  $E_1$  is the first-order exponential function,  $\kappa^* = \kappa/(\rho\alpha/\omega)$  the dimensionless absorption coefficient with respect to the EWBM parameters of the encountered wide-band and the density  $\rho$  of the considered gas species. The number of poles  $n_p$ , the poles  $p_i$  and the coefficients  $C_{i,1}$  and  $C_{1,2}$  are given by Denison & Fiveland [100]. A discretization of the absorption coefficient values is needed to compute  $\xi^*$  with Equation (50). The discretization with 19 logarithmically spaced absorption coefficients  $\kappa_j$  provided by Ströhle [101] is used in this work. These basic absorption coefficients are computed as:

$$\kappa_j = \frac{\kappa_{max}}{e^{j-1}} \frac{1}{(n_k - 1)} \ln \left( \frac{\kappa_{max}}{\kappa_{min}} \right); j = 1, 2, \dots, 19 \quad (51)$$

and are bounded by the limiting absorption coefficients  $\kappa_{j-1/2}$ :

$$\kappa_{j-1/2} = \frac{\kappa_{max}}{e^{j-1/2}} \frac{1}{(n_k - 1)} \ln \left( \frac{\kappa_{max}}{\kappa_{min}} \right). \quad (52)$$

The maximum and minimum values,  $\kappa_{max}$  and  $\kappa_{min}$ , are calculated from the given correlation by Ströhle [101]:

$$\begin{aligned}\kappa_{max} &= \max(p_{H_2O} \cdot 500m^{-1}, p_{CO_2} \cdot 1000m^{-1}), \\ \kappa_{min} &= 10^{-6}\kappa_{max}\end{aligned}\quad (53)$$

where the partial pressures of water vapor and carbon dioxide are volume averaged values of the considered domain. The values of  $\kappa_{j-1/2}$  are used in Equation (50) to compute the lower and upper limiting wavenumbers of each wavenumber interval  $\Delta\eta_i$  within the wide-bands of the considered gases. Accordingly, for each  $\Delta\eta_i$  the associated constant value of  $\kappa_j$  is assigned. Since the blackbody intensity varies over the vibration-rotation bands, the limiting reordered wavenumbers of each  $\Delta\eta_i$  are used to calculate the blackbody fractions and the corresponding weight factors to solve the RTE given in Equation (39). If overlapping of different bands of the gas species is present, the basic absorption coefficient for this  $\Delta\eta_i$  is the sum of the basic absorption coefficients of all overlapping bands. It is noted here, that in case of an inhomogeneous medium, the intervals  $\Delta\eta_i$  are determined once for a reference condition and held constant. The reference condition  $\underline{\phi}_0$ , as investigated by Ströhle [101], is estimated as the volume average of the considered physical quantity over the whole domain weighted by the emissive power in terms of  $T^4$  and the partial pressure of the absorbing gas  $p_{abs}$

$$\underline{\phi}_0 = \frac{\int_V \phi T^4 p_{abs} dV}{\int_V T^4 p_{abs} dV}. \quad (54)$$

The described procedure is quite time consuming. Thus, an optimization method is carried out [101], where the number of basic absorption coefficients is reduced from 19 to 3 based on the fit of the total emissivities. Here, the values of  $\kappa_j$  are adopted to minimize the error between the emissivities,  $\varepsilon_{3,L}$ , obtained with the three optimized absorption coefficients, and the emissivities,  $\varepsilon_{19,L}$ , computed with the 19 basic absorption coefficients over a range of path lengths:

$$error = \sum_L \left(1 - \frac{\varepsilon_{3,L}}{\varepsilon_{19,L}}\right)^2. \quad (55)$$

A downhill simplex method [102] is applied for error minimization, where the path length is varied from the minimum cell size to the maximum path length of the considered geometry. The emissivities are calculated as for the WSGG model given in Equation (40).  $\kappa_{max}$  and  $\kappa_{min}$  for the optimized basic absorption coefficients are computed as [101]

$$\begin{aligned}\kappa_{max} &= \max(p_{H_2O}^{0.2} \cdot 25m^{-1}, p_{CO_2}^{0.2} \cdot 50m^{-1}) \\ \kappa_{min} &= 10^{-2}\kappa_{max}\end{aligned}\quad (56)$$

In this work, three WBCK formulations from Ströhle [28] are adopted, which are described briefly in the following subsections.

### 2.2.6.1 Spectral formulation

In the “spectral formulation”, denoted as WBCK\_SPF hereafter, the blackbody fractions  $F[\Delta\eta_i, T(x)]$ , based on the local temperature  $T(x)$  at location  $x$ , are used to calculate the local weights  $a_i(x)$  in the considered wavenumber interval  $\Delta\eta_i$ :

$$a_i(x) = F[\Delta\eta_{i,l}, T(x)] - F[\Delta\eta_{i,u}, T(x)]. \quad (57)$$

Here,  $\Delta\eta_{i,l}$  and  $\Delta\eta_{i,u}$  are the lower and upper limiting wavenumbers of the considered wavenumber interval. The local absorption coefficients  $\kappa_i(x)$  are assumed constant in the considered  $\Delta\eta_i$  and are computed as the sum of the basic absorption coefficients at  $\Delta\eta_i$  multiplied by the ratio of the local partial pressure  $p_l(x)$  to the reference partial pressure  $p_{l,0}$  of the considered species  $l$ :

$$\kappa_i(x) = \sum_l \kappa_j(\Delta\eta_i, l) \frac{p_l(x)}{p_{l,0}}. \quad (58)$$

It is noted that the number of RTEs to be solved depends on the thermal conditions of the problem, but ranges between 209 and 418 [28].

### 2.2.6.2 Gray gases formulation

In the “gray gases” formulation, referred to as WBCK\_GGF, all wavenumber intervals with the same basic absorption coefficient  $\kappa_j$  are assigned to one gray gas  $k$ . The weight factor  $a_k(x)$  for each gray gas is computed by summing up the blackbody fractions of the assigned wavenumbers:

$$a_k(x) = \sum_i (F[\Delta\eta_{i,l}, T(x)] - F[\Delta\eta_{i,u}, T(x)]) \text{ for } \kappa_{j-1/2} < \kappa_j(\Delta\eta_i) \leq \kappa_{j+1/2}. \quad (59)$$

The local absorption coefficient of the gray gas  $\kappa_k(x)$  is proportional to the basic absorption coefficient and the ratio of the summed partial pressures of all absorbing gases  $p_{abs}(x)$  at the considered location and its reference value  $p_{abs,0}$ :

$$\kappa_k(x) = \kappa_j \frac{p_{abs}(x)}{p_{abs,0}}. \quad (60)$$

This formulation is suitable for gas mixtures with spatially constant ratios of partial pressures of all absorbing gases, since variations of each absorbing gas are not accounted for using the summed partial pressures. Generally, 20 RTEs (19 gray gases and 1 transparent gas) should be solved in the gray gas formulation. After the optimization procedure, however, only four RTEs

are computed. This optimized version is used to provide the results of the WBCK\_GGF model in this work.

### 2.2.6.3 Multiple gases formulation

In contrast to the WBCK\_GGF, the “multiple gases” formulation (WBCK\_MGF) approximates each absorbing gas  $l$  by  $N_l$  gray gases. An interval  $\Delta\eta_i$  in an overlapping region is solely assigned to the absorbing gas with the largest basic absorption coefficient  $\kappa_{j,l}(\Delta\eta_i)$  in this region. The local weight  $a_{i,l}(x)$  for a gray gas of the corresponding absorbing gas is calculated by:

$$\begin{aligned} a_{i,l}(x) &= \sum_i (F[\Delta\eta_{i,l}, T(x)] - F[\Delta\eta_{i,w}, T(x)]) \\ &\text{for } \kappa_{j-1/2} < \kappa_{j,l}(\Delta\eta_i) \leq \kappa_{j+1/2} \text{ and} \\ \kappa_{j,l}(\Delta v_i) &= \max[\kappa_{l'}(\Delta\eta_i)]; \quad m' = 1, N_l \end{aligned} \quad (61)$$

To compute the local gray absorption coefficient  $\kappa_{k,l}(x)$ , the basic absorption coefficient is scaled with the ratio of the corresponding partial pressure of the absorbing gas  $p_l(x)$  and its reference value  $p_{l,0}$ :

$$\kappa_{k,l}(x) = \kappa_{j,l} \frac{p_l(x)}{p_{l,0}}. \quad (62)$$

In total 39 ( $2 \times 19$  gray gases and 1 clear gas) RTEs have to be solved, if a gas mixture of two absorbing gases, which is almost always the case in combustion systems burning fossil fuels, is considered. Application of the optimization procedure reduces the number of RTEs to only 7. The optimized WBCK\_MGF is used in this thesis to calculate the simulation results given in Section 3.

## 2.3 Particle radiation modelling

Particle radiative properties in comparison to gas radiation properties vary more smoothly within the wavenumber spectrum. However, scattering by the presence of particles have to be accounted for in addition to particle absorption. The scattering process of each particle matter is described by the associated scattering coefficient and the scattering phase function. The latter one represents the probability of incoming radiation from a distinct direction to be scattered into each other direction. The models and particle material properties used in this work to compute the particle radiative properties for solving the RTE given in Equation (1) are described in the following subsections. In this thesis, all particles are assumed to be spherical in shape and homogeneous in composition. More general particle radiation

models including non-sphericity and inhomogeneity are described e.g. in the books of Bohren and Huffmann [103] or Mishchenko et al. [103]. In addition, independent scattering is assumed, i.e., scattering of a single particle is dependent solely on the incident external field and not on possible secondary fields of neighboring particles.

### 2.3.1 Mie Theory

In his work [104], Mie provided a theory to describe the radiative properties of absorption and scattering for spherical, homogeneous particles incident by plane-polarized electromagnetic waves. To find a solution for this problem, Maxwell's equations, see e.g. [103] or [105], expressed in spherical coordinates have to be solved and the incident plane-polarized electromagnetic wave has to be formulated in spherical vector harmonics. This yields to the problem of finding solutions to the vector wave equation. The scattered and internal fields can be computed from the incident electromagnetic wave if across the particle boundary the condition is satisfied that the tangential components of the electric and magnetic fields are continuous. In this subsection only the expressions of the scattered field are provided, since the internal fields are not of interest in this work.

In general, the Mie coefficients  $a_n$  and  $b_n$  have to be computed to derive the scattered electric and magnetic fields resulting from the incident electromagnetic field. With the known incident field and the according particle material properties, the associated extinction, scattering and absorption efficiencies as well as the scattering phase function are obtained. The spectral Mie coefficients  $a_{n,\eta}$  and  $b_{n,\eta}$  for computational evaluation are expressed as:

$$a_{n,\eta} = \frac{m_{p,\eta}\psi_n(m_{p,\eta}x_{p,\eta})\psi'_n(x_{p,\eta}) - \psi_n(x_{p,\eta})\psi'_n(m_{p,\eta}x_{p,\eta})}{m_{p,\eta}\psi_n(m_{p,\eta}x_{p,\eta})\xi'_n(x_{p,\eta}) - \xi_n(x_{p,\eta})\psi'_n(m_{p,\eta}x_{p,\eta})} \quad (63)$$

$$b_{n,\eta} = \frac{\psi_n(m_{p,\eta}x_{p,\eta})\psi'_n(x_{p,\eta}) - m_{p,\eta}\psi_n(x_{p,\eta})\psi'_n(m_{p,\eta}x_{p,\eta})}{\psi_n(m_{p,\eta}x_{p,\eta})\xi'_n(x_{p,\eta}) - m_{p,\eta}\xi_n(x_{p,\eta})\psi'_n(m_{p,\eta}x_{p,\eta})}. \quad (64)$$

Here, the size parameter  $x_{p,\eta} = 2\pi r_p \cdot \eta$ , calculated with the particle radius  $r_p$ , and the particle spectral complex index of refraction  $m_{p,\eta} = n_{p,\eta} - i k_{p,\eta}$ , where  $n_{p,\eta}$  is the real part of the spectral complex index of refraction and  $k_{p,\eta}$  is the spectral absorptive index of the considered material, have to be provided for the investigated coal/char and ash particles, see Subsection 2.3.5.  $\psi_n$  and  $\xi_n$  are the Riccati-Bessel functions and the prime denotes the first derivative of each function with respect to its argument. The Riccati-Bessel functions are linked to the spherical Bessel,  $j_n$ , and Hankel,  $h_n^{(1)}$ , functions, see e.g. [106], through:

$$\begin{aligned}\psi_n(z) &= zj_n(z) \\ \xi_n(z) &= zh_n^{(1)}(z)\end{aligned}\quad (65)$$

The particle spectral efficiencies of scattering,  $Q_{p,\eta,sca}$ , and extinction,  $Q_{p,\eta,ext}$ , are computed as:

$$Q_{p,\eta,sca} = \frac{2}{x_{p,\eta}^2} \sum_{n=1}^{\infty} (2n+1) (|a_{n,\eta}|^2 + |b_{n,\eta}|^2) \quad (66)$$

$$Q_{p,\eta,ext} = \frac{2}{x_{p,\eta}^2} \sum_{n=1}^{\infty} (2n+1) \Re\{a_{n,\eta} + b_{n,\eta}\}. \quad (67)$$

The particle spectral efficiency of absorption is obtained from the difference of the extinction and scattering efficiencies  $Q_{p,\eta,abs} = Q_{p,\eta,ext} - Q_{p,\eta,sca}$ . The spectral efficiencies are linked with the particle projected surface area to the according cross sections,  $C_{p,\eta}$ , as:

$$C_{p,\eta,ext/sca/abs} = Q_{p,\eta,ext/sca/abs} \cdot \pi r_p^2. \quad (68)$$

The spectral Mie phase function,  $\Phi_{p,\eta}^{Mie}(\vec{s}_i, \vec{s})$ , is obtained with the scattering efficiency as:

$$\Phi_{p,\eta}^{Mie}(\vec{s}_i, \vec{s}) = 2 \frac{i_{\parallel} + i_{\perp}}{x_{p,\eta}^2 Q_{p,\eta,sca}}, \quad (69)$$

where  $i_{\parallel}$  and  $i_{\perp}$  are the ratios of the scattered spectral intensities parallel and perpendicular to the scattering plane, respectively, with regard to the incident spectral intensity. Both ratios are dependent on the size parameter, complex index of refraction and the scattering angle  $\psi$ . Here, the scattering angle represents the angle between the directions  $\vec{s}_i$  and  $\vec{s}$ .  $i_{\parallel}$  and  $i_{\perp}$  can be obtained from the two complex amplitude functions  $S_1(\psi)$  and  $S_2(\psi)$  through:

$$i_{\parallel} = |S_1|^2 \quad (70)$$

$$i_{\perp} = |S_2|^2. \quad (71)$$

$S_1(\psi)$  and  $S_2(\psi)$  are computed with the spectral Mie coefficients as:

$$S_1(\psi) = \sum_{n=1}^{\infty} \frac{2n+1}{n(n+1)} (a_{n,\eta} \pi_n(\cos(\psi)) + b_{n,\eta} \tau_n(\cos(\psi))) \quad (72)$$

$$S_2(\psi) = \sum_{n=1}^{\infty} \frac{2n+1}{n(n+1)} (b_{n,\eta} \pi_n(\cos(\psi)) + a_{n,\eta} \tau_n(\cos(\psi))) \quad (73)$$

where  $\pi_n$  and  $\tau_n$  are angle-dependent functions defined with the Legendre polynomials  $P_n$  as:

$$\pi_n(\cos(\psi)) = \frac{dP_n(\cos(\psi))}{d\cos(\psi)} \quad (74)$$

$$\tau_n(\cos(\psi)) = \cos(\psi)\pi_n(\cos(\psi)) - \sin^2(\psi) \frac{d\pi_n(\cos(\psi))}{d\cos(\psi)}. \quad (75)$$

Another important property, especially for simplifying the modelling of the scattering process, is the spectral asymmetry factor  $g_{p,\eta}$ , which is the average cosine of the scattering angle. This property can be obtained from the spectral Mie coefficients and their conjugate complex counterparts  $a_{n,\eta}^*$ ,  $b_{n,\eta}^*$  through:

$$g_{p,\eta} = \frac{4}{x_{p,\eta}^2 Q_{p,\eta,sca}} \sum_{n=1}^{\infty} \left[ \frac{n(n+2)}{n+1} \Re\{a_{n,\eta} a_{n+1,\eta}^* + b_{n,\eta} b_{n+1,\eta}^*\} + \frac{2n+1}{n(n+1)} \Re\{a_{n,\eta} b_{n,\eta}^*\} \right]. \quad (76)$$

Values of  $g_{p,\eta} = 1$  and  $g_{p,\eta} = -1$  mean that all the incoming radiation is scattered solely into the forward and backward direction, respectively, whereas a value of  $g_{p,\eta} = 0$  represents isotropic scattering in all directions.

The computer program given by Bohren & Huffman [103] is used to calculate the extinction  $Q_{p,\eta,ext}$ , scattering  $Q_{p,\eta,sca}$ , and absorption  $Q_{p,\eta,abs}$  efficiencies as well as the Mie scattering phase function and the asymmetry factor for the considered particles in this work. Further details about the numerical computation of the involved infinite series and mathematical functions can be found there.

### Particle clouds

The aforementioned particle radiative properties are valid for a single, spherical and homogeneous particle. The absorption  $\kappa_{p,\eta}$  and scattering coefficients  $\sigma_{p,\eta}$  of the coal/char and ash particle clouds with spherical shape and homogeneous material are determined as:

$$\kappa_{p,\eta} = Q_{p,\eta,abs} f_{A,p} \quad (77)$$

$$\sigma_{p,\eta} = Q_{p,\eta,sca} f_{A,p}, \quad (78)$$

where  $f_{A,p}$  is the total projected surface area per volume of the considered uniform particle cloud.

### 2.3.2 Henyey-Greenstein Phase Function

Since the calculation of the Mie phase function is computationally very expensive, the Henyey-Greenstein phase function [64] is commonly used as an appropriate approximation for strongly forward scattering media. The spectral Henyey-Greenstein phase function  $\Phi_{p,\eta}^{HG}(\vec{s}_i, \vec{s})$  is an analytical anisotropic phase function defined as

$$\Phi_{p,\eta}^{HG}(\vec{s}_i, \vec{s}) = \frac{1 - g_{p,\eta}^2}{[1 + g_{p,\eta}^2 - 2g_{p,\eta} \cos(\psi)]^{3/2}}. \quad (79)$$

This function is used in this work to investigate its influence on the modelling of coal/char and ash particles, which tend to be strongly forward scatterers.

### 2.3.3 Transport Approximation

Furthermore, the particle scattering phase function is modelled with the “transport” approximation [65], [66] to reduce the computational effort to solve the RTE given in Equation (1). Herein, the phase function  $\Phi_{p,\eta}^{Tr}(\vec{s}_i, \vec{s})$  is approximated by the sum of an isotropic component and a term representing the forward scattering peak as:

$$\Phi_{p,\eta}^{Tr}(\vec{s}_i, \vec{s}) = (1 - g_{p,\eta}) + 2g_{p,\eta}\delta(1 - \cos(\psi)). \quad (80)$$

With this expression the spectral RTE can be re-written in a similar form as for an isotropic medium:

$$\frac{dI_\eta}{ds} = (\kappa_{g,\eta} + \kappa_{p,\eta})I_{b,\eta} - \beta_\eta^{Tr}I_\eta + \frac{\sigma_{p,\eta}^{Tr}}{4\pi} \int_{4\pi} I_\eta(\vec{s}_i) d\Omega, \quad (81)$$

with the “transport” scattering and extinction coefficients given as:

$$\sigma_{p,\eta}^{Tr} = \sigma_{p,\eta}(1 - g_{p,\eta}) \quad (82)$$

$$\beta_\eta^{Tr} = \beta_\eta - \sigma_{p,\eta}g_{p,\eta}. \quad (83)$$

Thus, the RTE to be solved is significantly simplified, since no additional calculations of the phase functions of coal/char and ash particles and their normalizations have to be conducted during the simulation procedure. In addition, the solution of the RTE in isotropic scattering problems associated with the transport approximation requires less numbers of iterations to reach convergence.

### 2.3.4 Approximate particle properties

Three different formulations are used to approximate the particle spectral radiative properties in this work. For all these approximate models, the Henyey-Greenstein phase function is applied, since it causes negligible differences from the Mie phase function of the considered radiative source terms and wall heat fluxes to be discussed in Section 3.3.1.2

In the first approach, denoted as “GrayAsymFactorModel” hereafter, the spectrally varying absorption and scattering coefficients of the particles, as computed by Mie theory, are used in conjunction with the gray Henyey-Greenstein phase function. The gray Henyey-Greenstein phase functions are evaluated from Equation (79), but instead of the spectral asymmetry factor the Planck-mean asymmetry factor  $g_{p,PM}$  is used:

$$g_{p,PM} = \frac{\int_{\eta} g_{p,\eta} Q_{p,\eta,sca} I_{b,\eta} d\eta}{\int_{\eta} Q_{p,\eta,sca} I_{b,\eta} d\eta} \quad (84)$$

The second gray formulation, denoted hereafter as “GrayParticleModel”, introduces the Planck-mean values for the absorption and scattering coefficients as well as the scattering phase functions of the coal/char and ash particles. The Planck-mean values [77] are defined as:

$$\kappa_{p,PM} = \frac{\int_{\eta} \kappa_{p,\eta} I_{b\eta} d\eta}{\int_{\eta} I_{b\eta} d\eta} \quad (85)$$

$$\sigma_{p,PM} = \frac{\int_{\eta} \sigma_{p,\eta} I_{b\eta} d\eta}{\int_{\eta} I_{b\eta} d\eta} \quad (86)$$

$$\Phi_{p,PM}^{HG}(\vec{s}_i, \vec{s}) = \frac{\int_{\eta} \sigma_{p,\eta} \Phi_{p,\eta}^{HG}(\vec{s}_i, \vec{s}) I_{b\eta} d\eta}{\int_{\eta} \sigma_{p,\eta} I_{b\eta} d\eta}. \quad (87)$$

The last formulation (denoted as “GrayCIRModel”) applies spectrally varying absorption and scattering coefficients as well as spectrally varying Henyey-Greenstein phase functions, but computed with gray complex indices of refraction. The aim is to investigate the influence of assuming gray refractive indices on the accuracy of the radiative source term and net wall heat flux distributions. Johansson et al. [58] showed that a constant refractive index for ash particles is inconsistent with the strong spectrally varying refractive index observed in experimental data, but no quantitative results were given on the accuracy in regard to radiative source term and net wall heat flux distributions. Therefore, the gray refractive indices  $m_{coal} = 1.85 - 0.22i$  and  $m_{ash} = 1.50 - 0.020i$  are applied for the coal/char and ash particles, respectively. These data were taken from Modest [77], which were originally provided by Mengüç and Viskanta [107] for bituminous coal and fly-ash. The efficiencies of absorption and scattering as well as

the asymmetry factor of the coal/char particles are well reproduced with respect to the use of a spectrally varying refractive index, whereas the properties, especially the absorption efficiencies, for ash particles show somewhat higher deviations from the efficiencies obtained with a spectrally varying refractive index due to the experimentally observed spectral fluctuations of the refractive index for ash particles.

Table 2: Correlations to calculate the complex indices of refraction for coal/char and ash particles at different wavelengths  $\lambda$  ( $\lambda$  in  $\mu\text{m}$ ).

Particle	$n_{p,\eta}$		$k_{p,\eta}$	
Coal/Char	1.8		$\lambda < 3$	0.07
Kentucky no. 9 Coal [108]			$3 \leq \lambda < 7$	$-0.1095 + 0.1794 \lambda$ $-0.05345 \lambda^2$ $+ 0.00458 \lambda^3$
			$7 \leq \lambda < 11$	$3.914 - 1.435 \lambda$ $+0.1764 \lambda^2$ $- 0.007046 \lambda^3$
			$11 \leq \lambda$ $< 22$	$2.462 - 1.137 \lambda$ $+ 0.1931 \lambda^2$ $-0.01514 \lambda^3$ $+ 0.0005604 \lambda^4$ $-0.7891 \times 10^{-5} \lambda^5$
			$\lambda \geq 22$	0.3
			Ash Combined data [109]–[111]	$6 < \lambda$
	$6 \leq \lambda < 8$	$1.5 - 0.35 (\lambda - 6)$	$2.6 \leq \lambda < 7$	$0.0119 + 0.00233 \lambda$
	$8 \leq \lambda < 11$	$0.8 + 0.5 (\lambda - 8)$	$7 \leq \lambda < 9$	$-3.39 + 0.488 \lambda$
	$11 \leq \lambda < 12$	$2.3 - 0.5 (\lambda - 12)$	$9 \leq \lambda < 11$	1.0
	$\lambda \geq 12$	1.8	$11 \leq \lambda$ $< 12$	$8.7 - 0.7 \lambda$
			$\lambda \geq 12$	0.3

### 2.3.5 Particle material properties

In this study, the refractive index of coal/char particles is calculated with the experimental data for Kentucky no. 9 coal given by Manickavasagam and Mengüç [108], since the proximate and elemental analyses fit well with the coal used in the CFD simulations to derive the test case investigated in Subsection 3.3. The real part of the refractive index was set to a constant value at  $n_{p,\eta} = 1.8$ , whereas the absorption index  $k_{p,\eta}$  varied spectrally according to the formula given by Manickavasagam and Mengüç [108]. For ash particles, the fitted correlation given by Gronarz et al. [58] was used to calculate the spectrally varying  $n_{p,\eta}$  and  $k_{p,\eta}$ . This correlation was fitted by Gronarz et al. to the combined data of Goodwin and Mitchner [110], Lohi et al. [111] and Gupta and Wall [109]. Table 2 depicts the correlations used in this work to calculate the spectral refractive indices of coal/char and ash particles.

## 2.4 Numerical Methods

The numerical solution procedures used in this work to solve the RTE, as given in Equation (1), are introduced in this subsection. The Discrete Transfer Method (DTM) is solely applied in conjunction with the SNB model to compute the radiative wall heat fluxes and the source terms within the computational domain regarding the transmissivity as the radiative property of interest. The Discrete Ordinates Method (DOM) is employed to obtain the results for the test cases, where only gas radiation is investigated and the absorption coefficient is the main radiative property to be considered in the formulation of the RTE. The Finite Volume Method (FVM) yields the same results as the DOM if only gas radiation is considered. However, it is solely used in this work to investigate also the contribution of the particle radiation to the total radiation. This is mainly due to the simpler possibility to assure the normalization of the in-scattering term, see e.g. the discussion in the work of Boulet et al. [112]. Nonetheless, further improvements for the DOM were introduced in literature, e.g. by Liu et al. [113] or Hunter and Guo [114], [115], to satisfy the normalization condition of the in-scattering term.

### 2.4.1 Discrete Transfer Method

The DTM was originally proposed by Lookwood and Shah [116]. The domain of interest is subdivided into a prescribed amount of control volumes. The thermodynamic properties (temperature, gas and particle concentrations) are considered as constant and are assessed at the midpoints in each control volume. Accordingly, the boundaries of the enclosure are discretized into surface elements, where the wall temperatures and emissivities are specified at

the midpoints of each surface element. In contrast to the Monte Carlo method, the angular space is accounted for with a fixed set of directions and the according rays are traced back from the point of interest until they reach a boundary surface element of the enclosure. A modified ray-tracing procedure similar to the one presented by Liu et al. [117], [118] is used in this work to compute the radiative intensities at each surface midpoint of the control volumes. The  $T_N$  quadrature scheme [119] is applied to obtain the directions for the angular space discretization.

Within the context of the SNB model, the associated discretized form of the RTE presented in Equation (8) is given as [120]:

$$\{I_{\Delta\eta,i+1}^m - I_{\Delta\eta,i}^m\} = (1 - \tau_{g,\Delta\eta,i \rightarrow i+1}^m)I_{b,\Delta\eta,P} + C_{\Delta\eta,P}^m \quad (88)$$

where

$$C_{\Delta\eta,P}^m = I_{w,\Delta\eta,1}^m (\tau_{g,\Delta\eta,1 \rightarrow i+1}^m - \tau_{g,\Delta\eta,1 \rightarrow i}^m) + \sum_{k=1}^{i-1} [(\tau_{g,\Delta\eta,k+1 \rightarrow i+1}^m - \tau_{g,\Delta\eta,m,k+1 \rightarrow i}^m) - (\tau_{g,\Delta\eta,k \rightarrow i+1}^m - \tau_{g,\Delta\eta,m,k \rightarrow i}^m)] I_{b,\Delta\eta,P} \quad (89)$$

Here, the indices  $i$ ,  $P$  and 1 represent the midpoint of the surface elements and the midpoint of the considered control volume as well as the surface element of the encountered boundary of the enclosure, respectively, and the superscript  $m$  the discretized angular direction. The directional component of the total heat flux vector at the surface element is calculated from

$$q_{x/y/z,i} = \sum_{all \Delta\eta} \left( \sum_{m=1}^M l_{x/y/z}^m I_{x/y/z,\Delta\eta,i}^m w^m \right) \Delta\eta \quad (90)$$

with  $l_{x/y/z}^m$  being the direction cosine with respect to the x, y or z axis, respectively, and  $w^m$  the quadrature weight of the associated direction. The radiative source term is computed with a central differencing scheme as:

$$\nabla \cdot q_{i+1/2} = \frac{(q_{x,i+1} - q_{x,i})}{\Delta x} + \frac{(q_{y,i+1} - q_{y,i})}{\Delta y} + \frac{(q_{z,i+1} - q_{z,i})}{\Delta z}, \quad (91)$$

where  $\Delta x/y/z$  are the widths of the considered control volume in the rectangular coordinate system.

### 2.4.2 Discrete Ordinates Method

The DOM [121], [122], as the DTM, divides the enclosure into a prescribed amount of control volumes with the constant thermodynamic and radiative properties given at the midpoints of each control volume as well as at the midpoints of the boundary surface elements. The angular discretization is given by a fixed set of directions. Commonly, the  $S_N$  [121] or  $T_N$  quadrature schemes [119] are applied to specify the set of directions with the according weights and direction cosine values. The RTE given in Equation (1) for a fixed direction of a 3D geometry given in the Cartesian coordinate system is expressed as [123]:

$$l_x^m \frac{\partial I^m}{\partial x} + l_y^m \frac{\partial I^m}{\partial y} + l_z^m \frac{\partial I^m}{\partial z} = -\beta I^m + S^m, \quad (92)$$

where the spectral dependence is skipped for convenience and to illustrate that any radiation model providing the absorption and scattering coefficients can be used with this solution procedure. The source function  $S^m$  is given by:

$$S^m = (\kappa_g + \kappa_p)I_b + \frac{\sigma_p}{4\pi} \sum_{m'} I^{m'} \Phi_p(m', m) w^{m'}, \quad (93)$$

Besides the prescribed direction, in the DOM the integration of the radiative intensity over the solid angle (in-scattering term, wall flux or radiative source term) is replaced by a weighted sum due to the applied angular quadrature scheme. Equation (92) can be further rearranged to yield the radiative intensity at the midpoint,  $I_p^m$ , of each control volume by integration over the whole control volume. The according expression for an angular direction pointing into the first octant is given after some manipulation by:

$$I_p^m = \frac{\frac{l_x^m I_w^m}{\Delta x} + \frac{l_y^m I_s^m}{\Delta y} + \frac{l_z^m I_d^m}{\Delta z} + \mu S_p^m}{\frac{l_x^m}{\Delta x} + \frac{l_y^m}{\Delta y} + \frac{l_z^m}{\Delta z} + \mu\beta}. \quad (94)$$

Here, the following relations were used to approximate the radiative intensity values at the control volume surfaces with the radiative intensity at the midpoint of each control volume:

$$I_p^m = \begin{matrix} \mu I_e^m - (1 - \mu)I_w^m \\ \mu I_n^m - (1 - \mu)I_s^m, \\ \mu I_u^m - (1 - \mu)I_d^m \end{matrix} \quad (95)$$

where  $\mu$  is the weighting factor of the applied spatial discretization scheme, see Subsection 2.4.4, and the same value is used for each direction in this work. The subscripts  $e$ ,  $w$ ,  $n$ ,  $s$ ,  $u$  and  $d$  represent the values at the control volume surfaces for surface normal vectors pointing

into the positive or negative x, y and z axis, respectively. The computation of the total heat flux vector is carried out as given in Equation (90), whereas the total radiative source term is calculated as:

$$\vec{V} \cdot \vec{q}_p = (\kappa_g + \kappa_p) \cdot \left[ 4\pi I_b - \sum_{m=1}^M I_p^m w^m \right]. \quad (96)$$

### 2.4.3 Finite Volume Method

The FVM, see e.g. [124], [125] applies the same spatial discretization method as the DOM. The distinct difference is the discretization of the angular space into angular control volumes. Here, the azimuthal,  $\theta$ , and polar,  $\varphi$ , angles are subdivided into a specified amount of values  $N_\theta$  and  $N_\varphi$ , respectively. In this work, an equally spaced distribution of the angles is used yielding the following values for the surface points of each angular control volume:

$$\theta_k = k \frac{\pi}{2N_\theta}, k = 0, \dots, 2N_\theta \quad (97)$$

$$\varphi_l = l \frac{2\pi}{2N_\varphi}, l = 0, \dots, 2N_\varphi. \quad (98)$$

Further angular discretization schemes were introduced in the literature, e.g. the  $FT_n$  scheme of Kim and Huh [126], to assure equal values for the solid angles in each direction. The RTE integrated over the angular control volume with solid angle  $\Delta\Omega^m$  to be solved by the FVM is given as [127]:

$$D_x^m \frac{\partial I^m}{\partial x} + D_y^m \frac{\partial I^m}{\partial y} + D_z^m \frac{\partial I^m}{\partial z} = (-\beta_{mod} I^m + S_{mod}^m) \Delta\Omega^m, \quad (99)$$

where the modified extinction coefficient and source function are used to avoid instabilities in the solution procedure [128]:

$$\beta_{mod} = \beta - \frac{\sigma_p}{4\pi} \Phi_p(m, m) \Delta\Omega^m, \quad (100)$$

$$S_{mod}^m = (\kappa_g + \kappa_p) I_b + \frac{\sigma_p}{4\pi} \sum_{\substack{m'=1 \\ m' \neq m}}^M I^{m'} \Phi_p(m', m) \Delta\Omega^{m'}. \quad (101)$$

The term  $D_{x/y/z}^m$  is given as

$$D_{x/y/z}^m = \int_{\Delta\Omega^m} (\hat{n}_{x/y/z} \cdot \vec{s}^m) d\Omega^m \quad (102)$$

and represents the integrated direction cosine of the direction vector  $\vec{s}^m = (\sin\theta^m \cos\varphi^m)\hat{i} + (\sin\theta^m \sin\varphi^m)\hat{j} + (\cos\theta^m)\hat{k}$  with the associated coordinate axis over the considered solid angle;  $\hat{i}$ ,  $\hat{j}$ ,  $\hat{k}$  being the unit vectors of the Cartesian coordinate system. The surface normal vector  $\hat{n}_{x/y/z}$  points into the direction perpendicular to the according surface area of the spatial control volume. The solid angle  $\Delta\Omega^m$  is obtained from:

$$\Delta\Omega^m = \int_{\Delta\Omega^m} d\Omega = \int_{\varphi_l}^{\varphi_{l+1}} \int_{\theta_k}^{\theta_{k+1}} \sin\theta d\theta d\varphi. \quad (103)$$

In contrast to the DOM, Equations (102) and (103) are computed analytically in the FVM rather than being tabulated. The expression of the radiative intensity at the midpoint of each control volume in the first octant is obtained after integrating Equation (99) over a control volume, and dividing by the discretized value of the control volume, using Equation (95) to approximate the surface values with the midpoint values:

$$I_p^m = \frac{\frac{D_x^m I_w^m}{\Delta x} + \frac{D_y^m I_s^m}{\Delta y} + \frac{D_z^m I_d^m}{\Delta z} + \mu \bar{S}_p^m \Delta\Omega^m}{\frac{D_x^m}{\Delta x} + \frac{D_y^m}{\Delta y} + \frac{D_z^m}{\Delta z} + \mu \bar{\beta} \Delta\Omega^m}. \quad (104)$$

Here, the expressions  $\bar{\beta}$  and  $\bar{S}_p^m$  include the averaged form of the in-scattering term  $\bar{\Phi}_p$ :

$$\bar{\Phi}_p(m', m) = \frac{\int_{\Delta\Omega^m} \int_{\Delta\Omega^{m'}} \Phi_p(m', m) d\Omega^{m'} d\Omega^m}{\Delta\Omega^m \Delta\Omega^{m'}}. \quad (105)$$

This expression satisfies the normalization criterion for the in-scattering term. The accuracy of  $\bar{\Phi}_p$  calculated by numerical integration is increased by subdividing each discretized solid angle into  $5 \times 5$  sub-angles in this work, see e.g. [129]. The total heat flux and the radiative source term in each control volume are computed as:

$$q_{x/y/z,p} = \sum_{m=1}^M I_{x/y/z,p}^m D_{x/y/z}^m \quad (106)$$

$$\vec{v} \cdot \vec{q}_p = (\kappa_g + \kappa_p) \cdot \left[ 4\pi I_b - \sum_{m=1}^M I_p^m \Delta\Omega^m \right]. \quad (107)$$

#### 2.4.4 Spatial Discretization Schemes

The DOM and FVM apply spatial discretization schemes to approximate the values at the midpoints of the surface elements of each control volume with the values at the midpoints of each control volume, see Equation (95). These spatial discretization schemes are similar to the ones used in CFD simulations to compute the conservation equations of mass, momentum and energy.

The STEP scheme is the counterpart of the first order upwind scheme applied in CFD and approximates the surface value with the midpoint value of the upstream control volume, which the considered ray already passed. Thus, a value of unity is used for  $\mu$  in Equation (95). This scheme is computationally robust and does not produce unphysical negative values for the radiative intensity, but needs finer spatial discretization due to the first order accuracy.

The DIAMOND scheme is similar to the central differencing scheme in CFD by interpolating the surface value with the midpoint values of the neighboring control volumes. This scheme has second order accuracy with setting  $\mu = 1/2$ , but can produce negative values of the radiative intensity. Fiveland [123] proposed conditions for the spatial discretization of each direction in a 3D environment to reduce the probability of negative radiative intensity values in the DOM context. Amongst others, Liu et al. [130] and Coelho [131] reviewed further methods with higher accuracy and computational stability, which need an iteration procedure like the CLAM scheme to obtain the surface values with the midpoint values of additional control volumes.

Furthermore, the mean flux scheme (MFS), proposed by Ströhle et al. [132] for unstructured grids, is used in this work for the DOM. Here, mean values are used for the upstream and downstream intensities entering and leaving the considered control volume, respectively, in Equation (95). The mean upstream intensity is computed by a weighted sum of the intensities entering the considered control volume. The weights correspond to the projected surface areas in each direction. The mean downstream intensity is obtained by re-expressing Equation (95) for the downstream intensity. This scheme allows the computational stability of the STEP scheme in conjunction to the second order accuracy of the DIAMOND scheme by assigning  $\mu = 1/2$ .

## 3 Results

In this chapter the simulation results of the different oxy-fuel scenarios are presented. First, a 3D virtual oxy-fuel gas turbine combustor with two different dry recycle conditions is considered. Here, the influence of short path lengths and high pressures on the accuracy of the simulation results of different gas radiation models is investigated. Then a 3D virtual coal-fired furnace is regarded both for air and oxy-fuel (dry and wet flue gas recycle) combustion scenarios to study the impact of long path lengths, encountered in real applications at atmospheric pressure, as well as the non-isothermal and inhomogeneous combustion conditions on the model accuracy of various gas radiation models. Finally, the influence of the presence of gases and particles on total thermal radiation as well as the modelling of each radiative contribution are examined with regard to accuracy and computational expense. For this purpose, a 2D square geometry representing the region above the last burner stage within an oxy-fuel coal-fired furnace with wet recycle is considered.

### 3.1 Gas radiation modelling in a 3D virtual oxy-fuel gas turbine combustor with dry recycle

In this section the 3D oxy-fuel test cases of Ströhle [28] are investigated. Herein, the virtual gas turbine combustor is approximated by a rectangular enclosure with dimensions  $L_x \times L_y \times L_z = 0.4 \text{ m} \times 0.2 \text{ m} \times 0.2 \text{ m}$ , confined by black walls at 700 K. The basis for the assumed scalar profiles are the CFD simulation results of Ströhle et al. [133]. To reduce the complexity of the original scalar distributions, the distributions are idealized to get well defined profiles as functions of space. The physical quantity  $\phi$  (temperature, mole fractions of  $\text{CO}_2$  or  $\text{H}_2\text{O}$ ) is distributed throughout the domain by the following relation:

$$\phi = f_r \phi_w + (1 - f_r) \phi_c, \quad (108)$$

where the radial factor  $f_r = \min(2r/L_y, 1)$  is calculated with the radial distance from the centerline  $r = \left[ (y - L_y/2)^2 + (z - L_z/2)^2 \right]^{0.5}$ .  $\phi_w$  and  $\phi_c$  are the states along the wall and the centerline, respectively:

$$\phi_w = f_m \phi_e + (1 - f_m) \phi_d, \quad (109)$$

$$\phi_c = f_m \phi_e + (1 - f_m) \phi_f \quad (110)$$

Here,  $f_m = x/L_x$  is the mixing factor,  $\phi_e$  the completely mixed state at the exit,  $\phi_d$  the state of the diluent, which describes the gas close to the wall, and  $\phi_f$  the state of the fuel/oxidizer mixture (FOM). Accounting for the reaction of the FOM, a stoichiometric methane-oxygen mixture, in the burning zone between the entry at  $x = 0 \text{ m}$  and the completely reacted state at  $x = L_x/2 = 0.2 \text{ m}$ , a linear profile is assumed:

$$\phi_f = f_b \phi_{f,b} + (1 - f_b) \phi_{f,i} \quad (111)$$

with the burnout factor  $f_b = \min(2x/L_x, 1)$  and  $\phi_{f,b}$  and  $\phi_{f,i}$  being the burnt and initial state of the FOM, respectively. The considered variables for both cases are listed in

Table 3.

Table 3: Mole fractions and temperatures for test cases of 3D oxy-fuel virtual gas turbine combustor

Variable	Case 1	Case 2
$Y_{CO_2,d}$	1	1
$Y_{CO_2,e}$	0.9565	0.9565
$Y_{CO_2,f,i}$	0.4	0.625
$Y_{CO_2,f,b}$	0.7856	0.88
$Y_{H_2O,d}$	0	0
$Y_{H_2O,e}$	0.0435	0.0435
$Y_{H_2O,f,i}$	0	0
$Y_{H_2O,f,b}$	0.2144	0.12
$T_d$ [K]	700	700
$T_e$ [K]	1450	1450
$T_{f,i}$ [K]	700	700
$T_{f,b}$ [K]	3564	2510
$T_w$ [K]	700	700

Additionally, the temperature as well as mole fractions of  $CO_2$  and  $H_2O$  distributions in the axial direction  $x$  along the centerline at  $y = z = 0.1 \text{ m}$  and in radial direction  $y$  along the line at  $x = 0.2 \text{ m}$ ,  $z = 0.1 \text{ m}$  are shown for both test cases in Figure 4(a) and (b). The major differences between the cases are the encountered maximum combustion temperatures (2507 K for Case 1, 1980 K for Case 2), the mole fractions of  $CO_2$  and  $H_2O$  in the completely burnt mixture and the different amount of  $Y_{CO_2,f,i}$  in the  $CO_2$ -enriched FOM at the inlet (0.4 for

Case 1, 0.625 for Case 2). The absorption and emission are only considered for CO<sub>2</sub> and H<sub>2</sub>O in both cases. The total pressure is set to 20 atm.

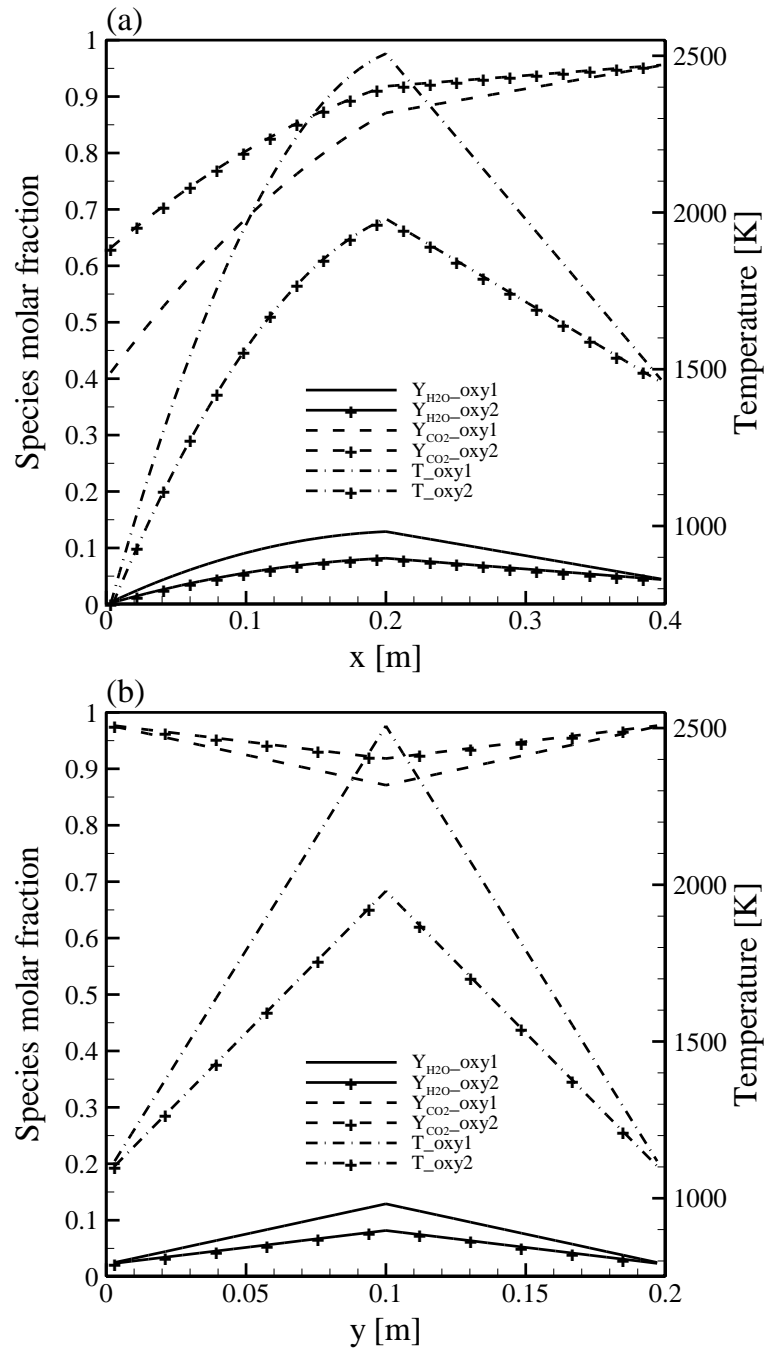


Figure 4: Axial (a) and radial (b) profiles of H<sub>2</sub>O molar fraction (solid), CO<sub>2</sub> mole fraction (dashed) and temperature (dash dotted) for oxy-fuel Case 1 (without symbols) and Case 2 (with symbols).

### 3.1.1 Results and discussion

The computational domain is resolved with 63 x 33 x 33 uniform control volumes for both cases and for all considered radiation models. The benchmark results of the SNB model were calculated using a 3D ray-tracing method, see Subsection 2.4.1, using T<sub>4</sub> (128 directions) [119] for angular discretization. Comparisons with the simulation results of the finer T<sub>7</sub>

(392 directions) scheme showed only minor differences with a relative difference of less than 0.7 %, conforming that the used  $T_4$  approximation is sufficiently fine for angular discretization. The discrete ordinates method (DOM) with the  $T_4$  scheme was used to calculate the RTE for the absorption coefficient based models (NBCK, FSCK, WBCK, and WSGG). Additionally, the angular discretization was carried out with the finer  $T_7$  scheme. Here, the same minor differences, as for the SNB simulation results, were observed in comparison to the  $T_4$  scheme.

### 3.1.1.1 Case 1 (dry recycle with 40 % CO<sub>2</sub> in fuel/oxidizer mixture)

As the first test case, the oxy-fuel fired virtual gas turbine combustor with 40 % CO<sub>2</sub> in the FOM is investigated. The SNB results were calculated using the updated SNB parameters of Rivière and Soufiani [81]. The benchmark results (SNB), shown in Figure 5, display the expected peak of the radiative source term along the centerline at  $x = 0.2 \text{ m}$ , since the highest combustion temperatures are encountered in this region. The second peak near the exit wall is caused by the large difference in temperature between the gas mixture near the wall (1450 K) and the wall itself (700 K). The NBCK results are in very good agreement with the benchmark data, proving its similar accuracy to that of the SNB model. The results of the FSCK, WBCK\_SPF and optimized WBCK\_MGF models are almost indistinguishable in the hottest region between  $0.1 \text{ m} < x < 0.3 \text{ m}$  along the centerline, as depicted in Figure 5(a). They slightly under-predict the radiative source peak by less than 10 % and are still considered in good agreement with the benchmark data. Outside this region, the NBCK and FSCK results are almost identical. Noteworthy are the same radiative source term distributions of the WBCK\_SPF and WBCK\_MGF models, although the WBCK\_MGF computes only 7 RTEs in comparison to 262 solved in the WBCK\_SPF. The optimized WBCK\_GGF is the least accurate model of the considered correlated-k approaches. It under-predicts the peak value by about 30 % and shows an overall discrepancy of about 22 % in comparison to the benchmark data. This observation was expected, since this WBCK formulation is suitable only for gas mixtures with a spatially constant ratio of partial pressures of all absorbing gases, which is not the case here.

The radiative source term results of the WSGG models, given in Figure 5(b), show significant deviations that are in the same order of magnitude as the WBCK\_GGF results. The high deviation of the WSGG model with the parameters of Johansson et al. (WSGG5\_Johansson) in the high temperature region by about 40 % is partially due to the underlying database used to derive the WSGG parameters. The used database, based on the 1997 EM2C SNB model parameters, is in accordance to HITEMP2010, which incorporates CSDS-1000 for CO<sub>2</sub>, based on the study of Chu et al. [16]. However, the benchmark SNB solution was obtained using the

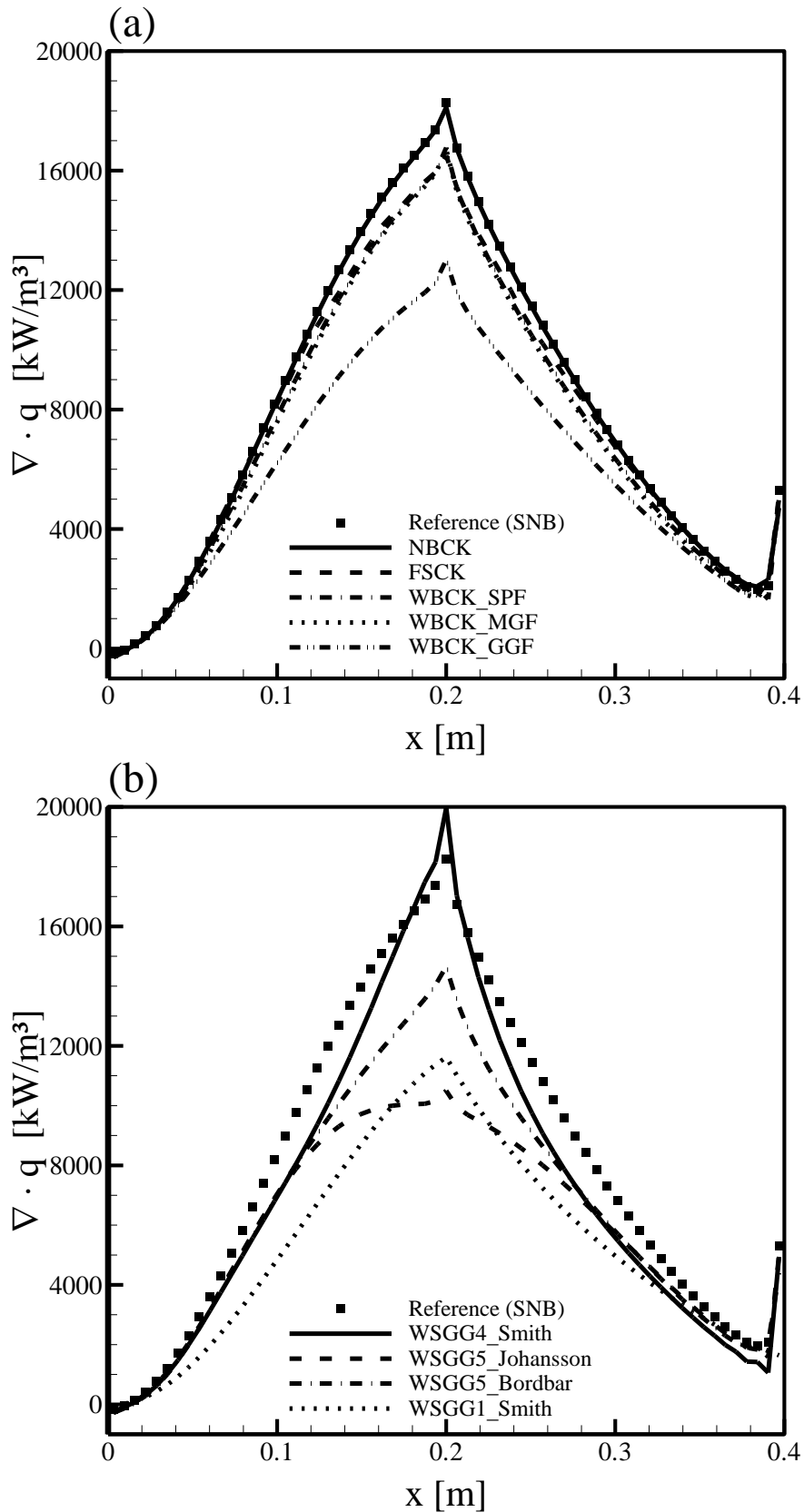


Figure 5: Comparison of the axial radiative source term distributions along the centerline calculated by the considered correlated-k, (a), and WSGG, (b), models with the SNB benchmark solution for Case 1.

2012 EM2C SNB model parameters, which were derived from CDS-4000 for CO<sub>2</sub>. Even so, the discrepancy of the WSGG5\_Johansson model caused by the difference in model parameters is expected to be fairly small. Another potential cause for the poor accuracy of WSGG5\_Johansson model in Case 1 is the high temperature difference of about 1800 K encountered between the central temperature and the wall. A similar behavior was also observed by Johansson et al. [49] for temperature differences of about 1500 K, whereas for lower temperature differences the accuracy improved. This conjecture is supported by the much better agreement between the results of WSGG5\_Johansson model and the benchmark solution in Case 2 presented in the following subsection. Much better agreement between the results of the WSGG model with the parameters of Bordbar et al. (WSGG5\_Bordbar), which are obtained from the HITEMP 2010 database, and the benchmark solution can be observed. The WSGG model with the parameters of Smith et al. (WSGG4\_Smith) slightly over-predicts the radiative source term at  $x = 0.2$  m by around 10 %, but under-estimates the source terms in regions away from the peak temperature. It should be noticed that application of the WSGG4\_Smith model, which was developed for air-fuel combustion scenarios, in this test case involves extrapolation of the model parameters. On the other hand, the WSGG5\_Bordbar under-predicts the source terms around the peak temperature regions. The overall agreement of the WSGG4\_Smith model with the benchmark data is similar to that of the newer WSGG5\_Bordbar model. Additionally, the results for the gray WSGG model based on the parameters of Smith et al. (WSGG1\_Smith) are also shown in Figure 5(b), since this gray approach has been commonly used in commercial CFD codes. Clearly, this approach significantly under-predicts the radiative source term distribution and is the least accurate model among all models investigated.

Figure 6 depicts the radial distributions of the radiative source term along the line at  $x = 0.2$  m and  $z = 0.1$  m for all investigated radiation models. The NBCK and FSCK models slightly over-predict the radiative source by a maximum of 6 % in a radial distance of 0.03 to 0.09 m from the wall. The WBCK formulations and the non-gray WSGG models show a similar behavior as for the axial radiative source term distributions. The WSGG4\_Smith model strongly under-predicts the radiative source term distribution, except at the radial position with  $y = 0.1$  m. The gray WSGG1\_Smith model significantly under-predicts the magnitude of the radial radiative source term distributions, in particular in the middle of the combustor at  $y = 0.2$  m observed in Figure 6(b).

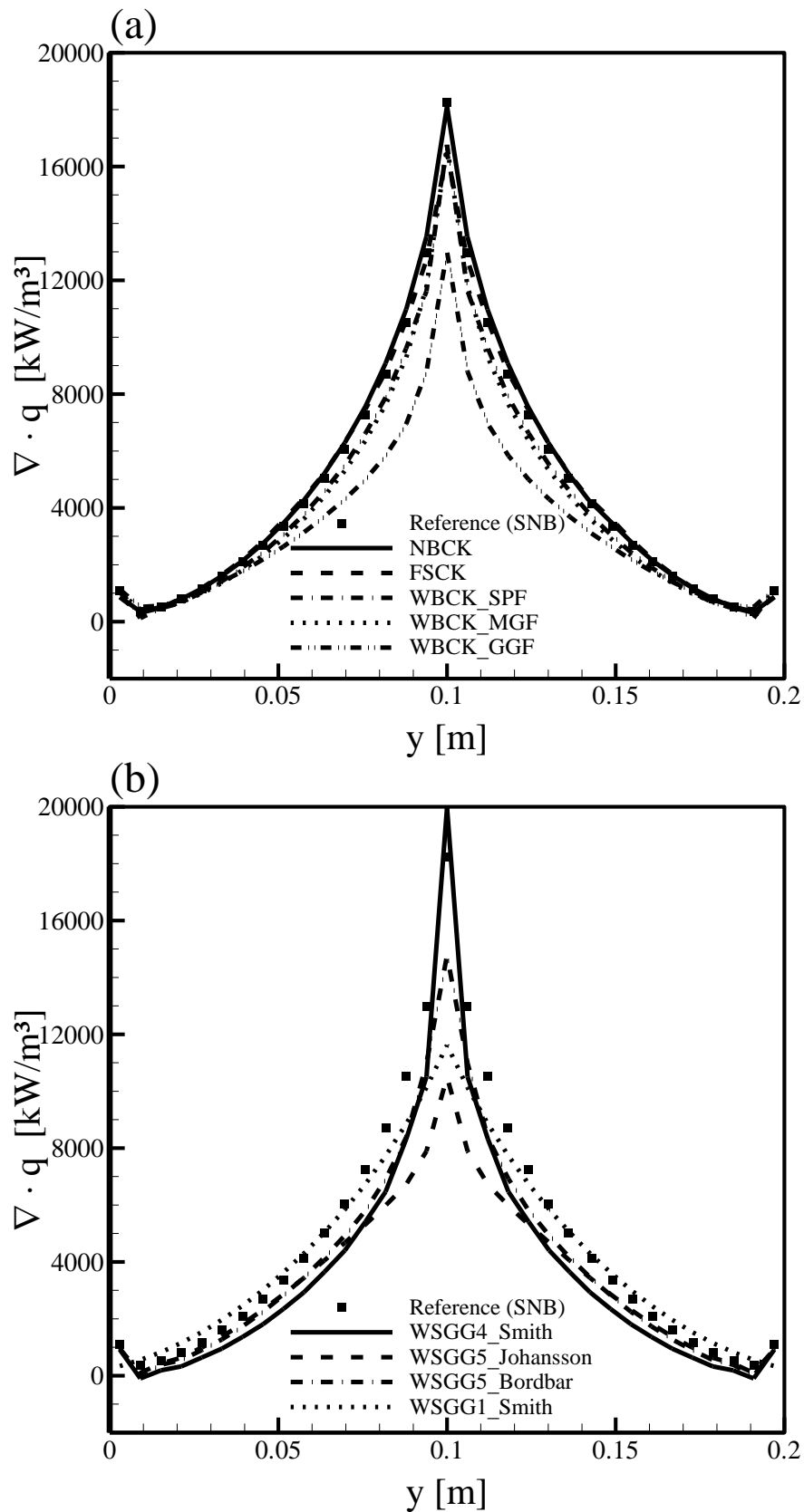


Figure 6: Comparison of the radial radiative source term distributions along the line at  $x = 0.2$  m and  $z = 0.1$  m calculated by the considered correlated-k, (a), and WSGG, (b), models with the SNB benchmark solution for Case 1.

In Figure 7 the wall heat fluxes along the centerline of the side wall at  $y = 0 \text{ m}$  and  $z = 0.1 \text{ m}$  are shown for all investigated radiation models. The results of the NBCK and FSCK models are almost identical to each other and are in good agreement with the benchmark data, with results of the NBCK and FSCK models being about 4 % higher in the peak temperature region, Figure 7(a). In comparison to these models, the WBCK\_SPF model slightly under-predicts the benchmark data by less than about 7 %. Higher deviations from the SNB results are observed for the WBCK\_MGF model, especially around the peak temperature at  $x = 0.2 \text{ m}$ . However, the overall accuracy of about 10 % is still slightly better than the WBCK\_GGF model, Figure 7(a).

Regarding the accuracy of WSGG models shown in Figure 7(b), the results of WSGG5\_Johansson and WSGG5\_Bordbar models are in close agreement with each other in the calculation of the net wall heat fluxes. The overall deviation of these two WSGG models of about 17 % is similar to that of the WBCK\_GGF formulation. It is remarkable to observe the very poor accuracy of the WSGG4\_Smith model in the prediction of the net wall heat flux, even though it performs quite well in the prediction of the centerline radiative source term shown in Figure 5(b). A possible explanation to the very different performance of WSGG4\_Smith model in the calculation of the source term, Figure 5(b), and the wall heat flux, Figure 7(b), is that its fairly good accuracy observed in Figure 5(b) is just a coincidence. However, the shape of the wall heat flux distribution is still correctly reproduced. The WSGG1\_Smith model over-predicts the wall heat flux around the peak temperature and then predicts a sharp drop towards the combustor exit, failing to predict the correct wall heat flux profile.

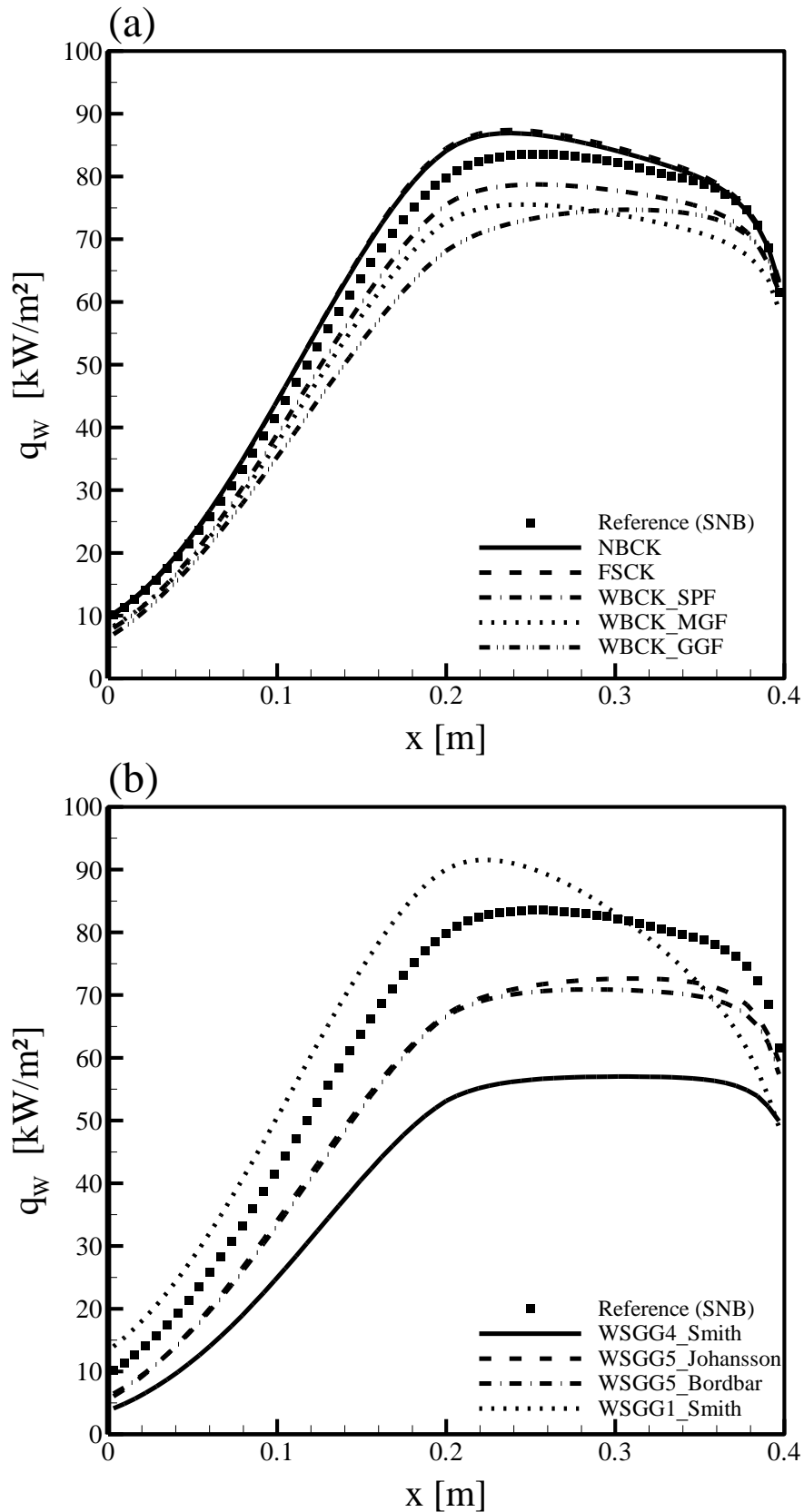


Figure 7: Comparison of the wall heat fluxes in radial direction  $y$  along the centerline of the side wall at  $y = 0$  m and  $z = 0.1$  m calculated by the considered correlated-k, (a), and WSGG, (b), models with the SNB benchmark solution for Case 1.

### 3.1.1.2 Case 2 (dry recycle with 62.5 % CO<sub>2</sub> in fuel/oxidizer mixture)

In the second oxy-fuel test case, the FOM enters the virtual gas turbine combustor with a higher CO<sub>2</sub> mole fraction of 62.5 %. Thus, the maximum combustion temperature of 1980 K is about 500 K lower than the one in Case 1. In Figure 8 the radiative source term distributions along the centerline are given. Similar to the observations made in Case 1, the NBCK results are in excellent agreement with the benchmark data, see Figure 8(a). The results of the FSCK model are again in very close agreement with those of the NBCK model and in remarkable agreement with the benchmark data. The WBCK\_SPF and WBCK\_MGF models are almost indistinguishable and are in relatively good agreement with the SNB results with a deviation lower than 8 %. Similar to Case 1, the WBCK\_GGF model shows the lowest accuracy among the correlated-k methods for the same reason as described for Case 1.

For the results of WSGG models, similar levels of agreement with the benchmark data can be observed for all the three non-gray WSGG models with an overall under-prediction of about 15 %, see Figure 8(b). In contrast to Case 1 shown in Figure 5(b), where the results of the WSGG5\_Johansson model show very large discrepancies and differ significantly from those of the WSGG5\_Bordbar model, the WSGG5\_Johansson and WSGG5\_Bordbar model results are very close to each other and are in fairly good agreement with the benchmark solution in Case 2. This observation supports the conjecture that the WSGG5\_Johansson model is better suited for problems where the maximum temperatures differences are lower than 1500 K, as in Case 2. Unlike its performance in Case 1 shown in Figure 5(b), the WSGG4\_Smith model displays quite large deviations from the benchmark solution, supporting the notion that its good performance in the prediction of the radiative source term in axial direction in Case 1 is likely a coincidence. The WSGG1\_Smith model once again significantly under-predicts the radiative source term, as in Case 1.

The radial distributions of the radiative source term along y-direction at  $x=0.2\text{ m}$  and  $z=0.1\text{ m}$  for Case 2 predicted by the approximate radiative models are compared with the SNB solution in Figure 9. Both the NBCK and the FSCK models slightly over-predict the magnitude of the source term, Figure 9(a). In contrast, the WBCK formulations and the non-gray WSGG models significantly under-predict the magnitude of the source terms similar to the axial distributions depicted in Figure 8. As for Case 1, the WSGG4\_Smith model predicts the lowest magnitude of the radiative source term in radial direction, especially in regions away from the walls. The gray WSGG1\_Smith model results in a much-flattened distribution of the radiative source term along the y-direction, Figure 9(b).

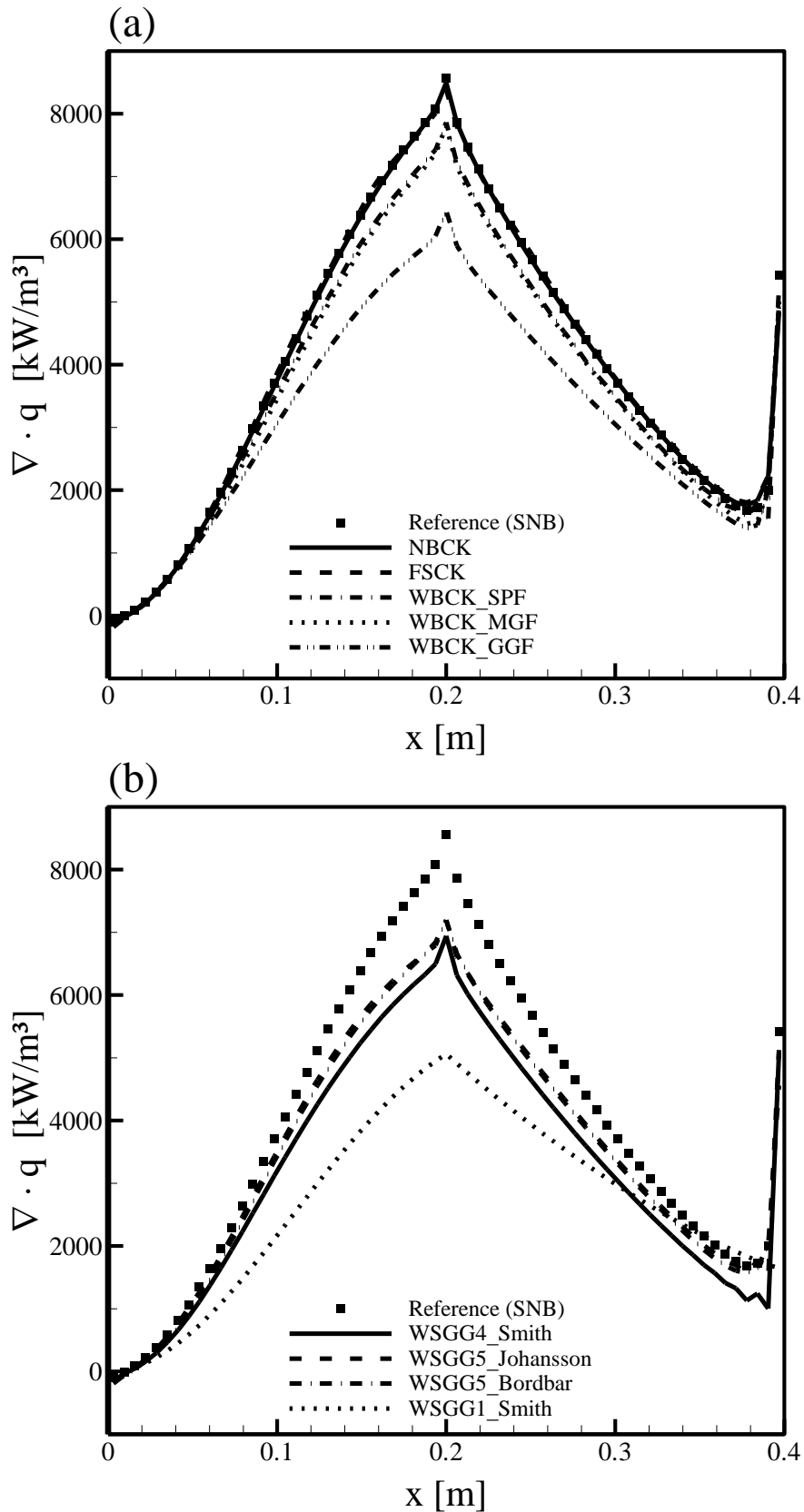


Figure 8: Comparison of the axial radiative source term distributions along the centerline calculated by the considered correlated-k, (a), and WSGG, (b), models with the SNB benchmark solution for Case 2.

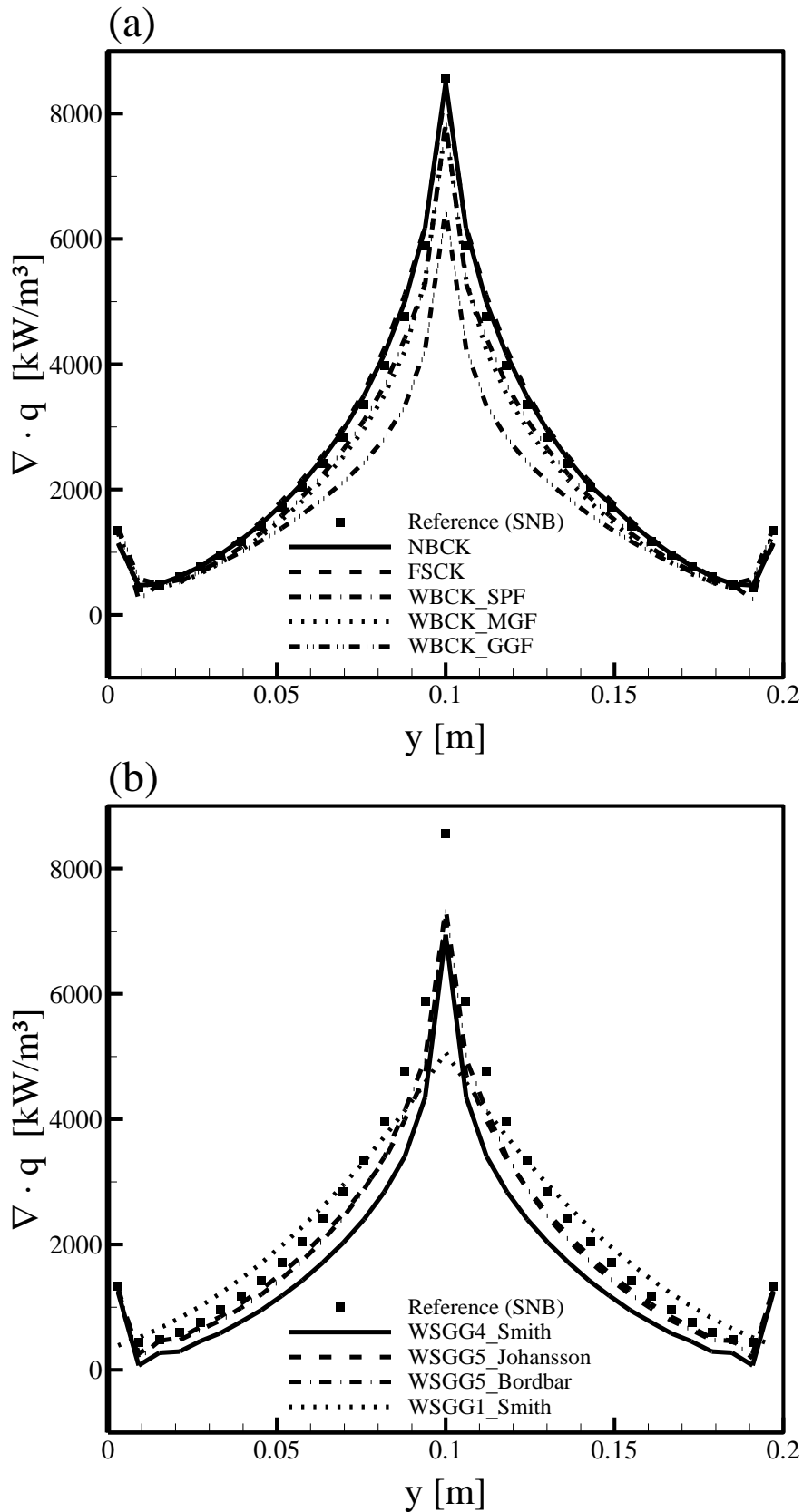


Figure 9: Comparison of the radial radiative source term distributions along the line at  $x=0.2$  m and  $z=0.1$  m calculated by the considered correlated-k, (a), and WSGG, (b), models with the SNB benchmark solution for Case 2.

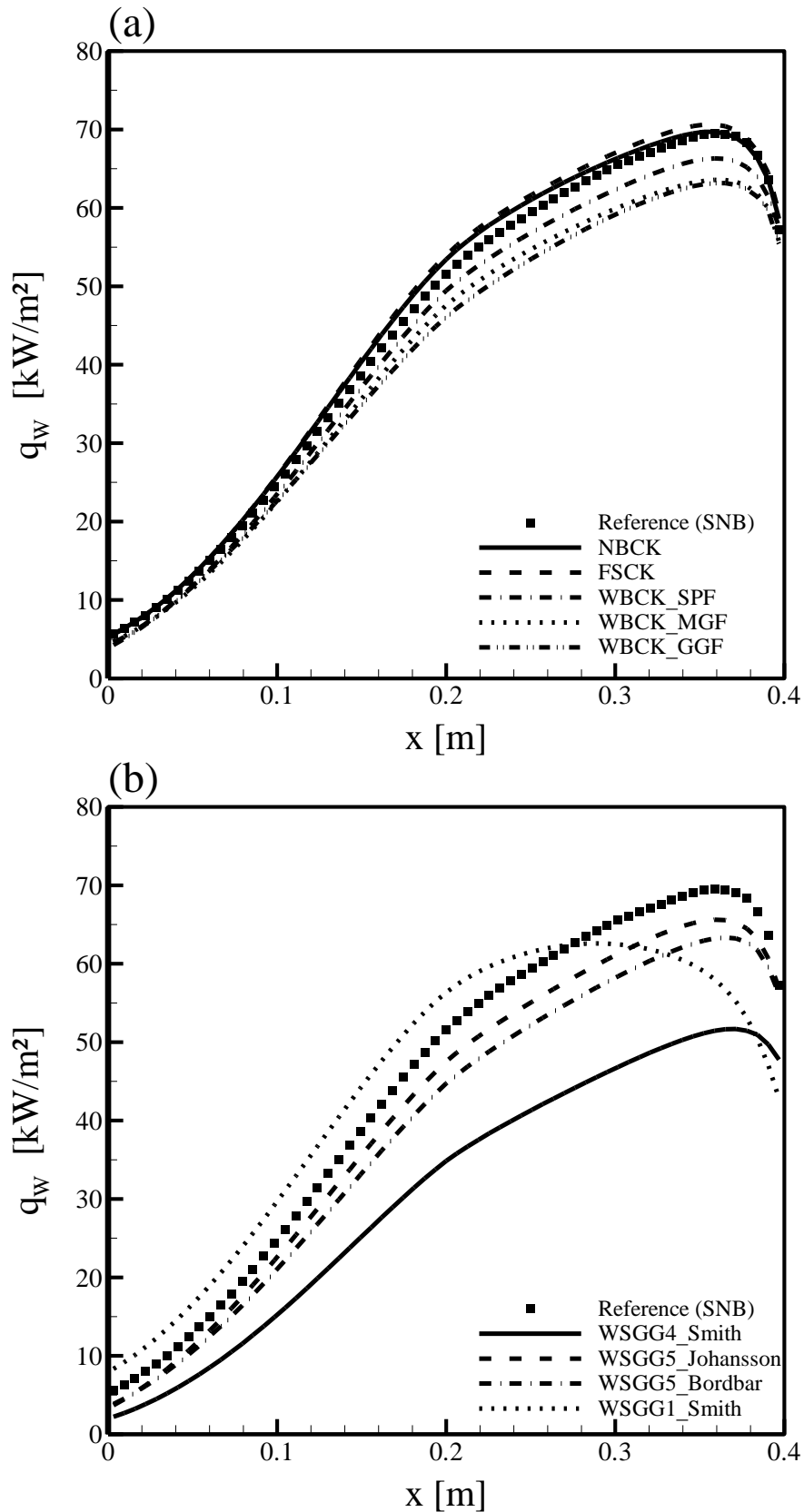


Figure 10: Comparison of the wall heat fluxes in radial direction  $y$  along the centerline of the side wall at  $y=0$  m and  $z=0.1$  m calculated by the considered correlated- $k$ , (a), and WSGG, (b), models with the SNB benchmark solution for Case 2.

Similar observations to those in Case 1 can be made for the wall heat fluxes along the centerline of the side wall at  $y=0$  m and  $z=0.1$  m, depicted in Figure 10(a) for the correlated-k approaches and in Figure 10(b) for the WSGG models. Here, the NBCK and FSCK models predict almost indistinguishable wall heat fluxes and are in very good agreement with the SNB results, Figure 10(a). The WBCK\_SPF, WBCK\_MGF and WBCK\_GGF formulations yield nearly the same wall heat fluxes and are in similar agreement with the benchmark data to that of the WSGG5\_Johansson and WSGG5\_Bordbar models. All these five models under-predict the wall heat fluxes by about 10 %. Similar to its performance in Case 1, the WSGG4\_Smith model is only able to predict the qualitatively correct profile of the wall heat flux, but suffers very large errors. The WSGG1\_Smith model again predicts an incorrect wall heat flux distribution, as observed in Case 1.

### 3.1.1.3 Overall performance

Detailed information about the number of RTEs solved and the accuracy of the investigated models are compared in Table 4. Herein, the mean values, including both test cases, of the relative errors for the radiative source terms along the axial combustor centerline  $\Delta_s$  and the wall heat fluxes along the centerline of a side wall  $\Delta_f$  are given. The mean relative errors are calculated as:

$$\Delta_s = \left( \left( \sum_l \frac{\nabla \cdot q_{SNB,l} - \nabla \cdot q_{Model,l}}{\nabla \cdot q_{SNB,l}} \right)_{Case1} + \left( \sum_l \frac{\nabla \cdot q_{SNB,l} - \nabla \cdot q_{Model,l}}{\nabla \cdot q_{SNB,l}} \right)_{Case2} \right) / 2, \quad (112)$$

$$\Delta_f = \left( \left( \sum_l \frac{q_{w,SNB,l} - q_{w,Model,l}}{q_{w,SNB,l}} \right)_{Case1} + \left( \sum_l \frac{q_{w,SNB,l} - q_{w,Model,l}}{q_{w,SNB,l}} \right)_{Case2} \right) / 2, \quad (113)$$

with  $\nabla \cdot q_{SNB,l}$ ,  $\nabla \cdot q_{Model,l}$ ,  $q_{w,SNB,l}$  and  $q_{w,Model,l}$  as the radiative source terms and wall heat fluxes of the reference SNB model and the investigated radiation model at each axial position, respectively.

As expected, the most accurate model is NBCK, but it is also the most expensive regarding the computational effort, since 3150 RTEs have to be solved for each discretized angular direction. The FSCK model predicts very accurately the radiation properties for both test cases at a fairly low computational cost. It should be pointed out that besides solving the RTEs the computational effort of the FSCK model also involves finding the cumulative distribution function of the CO<sub>2</sub>-H<sub>2</sub>O mixture at each control volume, which constitutes a substantial computational overhead of this model. The WBCK\_SPF is the most accurate one of the considered WBCK formulations, but the slightly better agreement in comparison to WBCK\_MGF

model does not justify the much higher computational effort. The FSCK model is more accurate than the WBCK\_MGF model at a similar computational cost. The prediction of radiative quantities with the WBCK\_GGF model is in the same order of accuracy and computational expense as the non-gray WSGG models. The WSGG5\_Bordbar and WSGG5\_Johansson models show better agreement with benchmark data than the WSGG4\_Smith model. The least time-consuming model is the gray WSGG approach, since only one RTE is solved for each direction. However, the strong reduction in computational effort is accompanied with poor accuracy.

**Table 4: The number of transfer equations per direction,  $n_t$ , and the mean relative errors, including Cases 1 and 2, for the radiative source,  $\Delta_s$ , and the radiative heat flux,  $\Delta_f$ , of the considered radiation models**

Model	$n_t$	$\Delta_s$ (%)	$\Delta_f$ (%)
SNB	-	-	-
NBCK	3150	0.8	2.5
FSCK	10	2.7	3
WBCK_SPF	160	6.5	6.5
WBCK_MGF	7	7.5	9.5
WBCK_GGF	4	20	12
WSGG4_Smith	4	17.5	35.5
WSGG5_Johansson	5	15.5	13.5
WSGG5_Bordbar	5	15	15.5
WSGG1_Smith	1	32.5	30

Among the investigated models, the most expensive are the SNB and NBCK models. Both need a large amount of CPU times to compute the radiative properties, since the transmissivities (SNB) and the absorption coefficients (NBCK) have to be calculated for each narrow-band. Keeping in mind that up to 449 bands for H<sub>2</sub>O and 323 bands for CO<sub>2</sub> have to be considered in the wavenumber range between 50 and 11250 cm<sup>-1</sup> [81] with a spectral resolution of 25 cm<sup>-1</sup> for each wavenumber interval. This is particularly true for SNB since the coupling of SNB with the 3D ray-tracing solver is very computationally demanding. Such a level of computation effort is impractical for CFD simulations. The WSGG models are the least time consuming among the considered models and have already been used in CFD simulations of large-scale applications, e.g. [134]. Although the computational efficiency of the FSCK model is seemingly somewhat similar to that of the WBCK\_MGF and WBCK\_GGF models, as well as close to that of the WSGG models, based on the number of the RTEs to be solved, it is in fact about an order of magnitude higher due to the treatment of mixtures of CO<sub>2</sub> and H<sub>2</sub>O in the present test cases. The time needed to calculate the spectral properties by the WBCK\_SPF method is about two orders of magnitude higher than that of the WSGG models.

### 3.1.2 Conclusions

The good accuracy of about 0.8 % relative error for the radiative source term and 2.5 % relative error for the wall heat flux of the NBCK model in both test cases manifests its capability to closely reproduce the benchmark results, but at a much lower computational expense than the SNB model, for 3D rectangular enclosures under oxy-fuel combustion conditions at high pressures. However, its computational expense is still too high to be used in CFD applications.

The FSCK model offers very good accuracy in both test cases, only slightly less than the NBCK model. Because of its good accuracy and fairly low computational expense, the FSCK model is recommended for radiation heat transfer calculations in oxy-fuel combustion systems for pressure path lengths up to about 10 bar m. It is found that the WBCK\_SPF and WBCK\_MGF formulations are in reasonably good agreement with the benchmark data, despite its different underlying database (EWBM). Deviations of the WBCK models from the SNB results are in general less than 10 %. In comparison with the FSCK results, the WBCK\_MGF model is somewhat less accurate at a more or less similar computational effort.

The WBCK\_GGF and the non-gray WSGG models have similar accuracy and similar computational efficiency. The improved WSGG parameters of Bordbar et al. [53] provide consistently the most accurate results of the considered WSGG models for both test cases. The WSGG model with the parameters of Johansson et al. [49] suffers larger deviations for the source term distribution in the first test case, likely because of the presence of higher temperatures differences of up to 1800 K between the combustor centerline and the walls. For lower temperature differences encountered in the second test case both WSGG models predict similar results. The parameters of Smith et al. [82] should not be used for oxy-fuel combustion, since the wall heat flux is strongly under-predicted by about 36 %. The commonly used gray WSGG model in commercial CFD codes is also not recommended for oxy-fuel calculations, since it is not able to reproduce qualitatively the wall heat flux distribution and suffers significant error in the radiative source term distributions.

Based on the presented results, the best practice to achieve high accuracy of radiation heat transfer calculations in CFD prediction of oxy-fuel combustion systems for pressure path lengths up to about 10 bar m at little to no increase in the overall computational cost is to first apply the WSGG model of Bordbar et al. [53] to achieve fairly converged solution and then to switch to the FSCK model.

### 3.2 Gas radiation modelling in a 3D virtual coal-fired furnace

Radiation heat transfer is investigated in the 3D test cases of a virtual coal-fired furnace from Ströhle et al. [135]. Herein, the furnace is approximated by a rectangular enclosure with the dimensions of  $L_x \times L_y \times L_z = 50\text{ m} \times 20\text{ m} \times 20\text{ m}$ , enclosed by black walls. The prescribed concentrations and temperature profiles were derived from a simplified combustion calculation for a coal-fired furnace burning a representative bituminous coal. The thermodynamic state of the unburned coal-oxidizer mixture was specified for all test cases at the inlet of the domain. At the outlet, the whole volatile and carbon matters were burnt and a typical outlet temperature before the first convective heat exchanger,  $T_e$ , was assigned. At the side walls, a typical temperature for water-cooled furnaces,  $T_w$ , was chosen. Fast release and combustion of volatiles as well as slow char combustion were assumed. With the aforementioned information, the concentrations of water vapor and carbon dioxide as well as the adiabatic combustion temperature could be calculated and used as the thermal input fields.

A physical quantity  $\phi$  of interest, namely temperature and mole fractions of  $\text{CO}_2$  and  $\text{H}_2\text{O}$ , is prescribed throughout the domain by the following assumed relation:

$$\phi = f_r \phi_w + (1 - f_r) \phi_c, \quad (114)$$

where the radial factor  $f_r = \left( \min(2r/L_y, 1) \right)^3$  is calculated with the radial distance from the centerline  $r = \left[ (y - L_y/2)^2 + (z - L_z/2)^2 \right]^{0.5}$ . To resemble the realistic distributions along the radial direction a polynomial function of third order is used.  $\phi_w$  and  $\phi_c$  are the thermodynamic states along the wall and the centerline, respectively. For the mole fractions of  $\text{H}_2\text{O}$  and  $\text{CO}_2$ , the distributions along the wall and centerline are given by:

$$\phi_{w,mf} = f_{b,v} \phi_{v,mf} + f_{b,char} \phi_{char,mf} + \phi_{i,mf}, \quad (115)$$

$$\phi_{c,mf} = f_{b,char} (\phi_{char,mf} + \phi_{v,mf}) + \phi_{i,mf}. \quad (116)$$

Here,  $f_{b,v} = (x/L_x)^{0.2}$  is the burnout factor of volatiles,  $\phi_{v,mf}$  the mole fraction generated by the combustion of volatiles,  $f_{b,char} = (x/L_x)^{0.5}$  the burnout factor of char,  $\phi_{char,mf}$  the mole fraction produced by the char combustion and  $\phi_{i,mf}$  the mole fraction at the inlet of the domain. The fast release and combustion of volatiles are taken into account by the fifth root function in the burnout factor of volatiles, whereas the slow combustion of carbon is modelled with a square root function in the burnout factor of char.

The temperature distribution along the centerline is calculated by:

$$T_c = (1 - f_a) \left[ f_{b,v} \frac{T_{ad}}{2} + f_{b,char} \frac{T_{ad}}{2} + (2 - f_{b,v} - f_{b,char}) T_i \right] + f_a T_e, \quad (117)$$

with the axial factor  $f_a = x/L_x$  and  $T_{ad}$ ,  $T_i$  and  $T_e$  being the adiabatic temperature (2663 K), temperatures at the inlet (600 K) and exit (1523 K) of the domain, respectively. The outlet of the virtual furnace is considered as a black wall at 1223 K, whereas the temperature of all other black walls,  $T_w$ , is set to 973 K. Table 5 lists the variables needed to compute the distributions of the physical quantities for the three test cases. Case 1 resembles conditions of a typical air-based coal-fired furnace, whereas Case 2 and Case 3 represent oxy-fuel conditions with dry and wet flue gas recirculation, respectively. The temperature distribution is the same in all the three test cases, see Figure 11 for illustration, and varies nonlinearly between minimum 973 K and maximum 1980 K within the domain. Thus, the major differences between the cases are due to the distributions of  $\text{CO}_2$  and  $\text{H}_2\text{O}$  at the inlet and within the domain.  $\text{CO}_2$  and  $\text{H}_2\text{O}$  are considered as the only radiating species, since the focus of this subsection is to investigate solely the impact of gas radiation models on radiation heat transfer. The  $\text{H}_2\text{O}$  to  $\text{CO}_2$  molar ratio ranges between 0.48 and 0.86 for Case 1, whereas molar ratios from 0.01 to 0.12 and 0.46 to 0.51 are encountered in Case 2 and 3, respectively. The pressure path length product is increased from 13 bar m in Case 1 up to about 55 bar m in Case 2 and 3 due to the higher sum of partial pressures. The total pressure of all the three test cases is kept at 1 atm.

Table 5: Mole fractions and temperatures for considered test cases of 3D coal-fired virtual furnace

Variable	Case 1	Case 2	Case 3
$Y_{i,\text{CO}_2}$	0	0.7085	0.5057
$Y_{V,\text{CO}_2}$	0.0636	0.0404	0.411
$Y_{Char,\text{CO}_2}$	0.0909	0.1128	0.1145
$Y_{i,\text{H}_2\text{O}}$	0	0	0.2436
$Y_{V,\text{H}_2\text{O}}$	0.0744	0.102	0.0635
$Y_{Char,\text{H}_2\text{O}}$	0	0	0
$T_{ad}$ [K]	2663	2663	2663
$T_i$ [K]	600	600	600
$T_e$ [K]	1523	1523	1523
$T_{w,outlet}$ [K]	1223	1223	1223
$T_w$ [K]	973	973	973

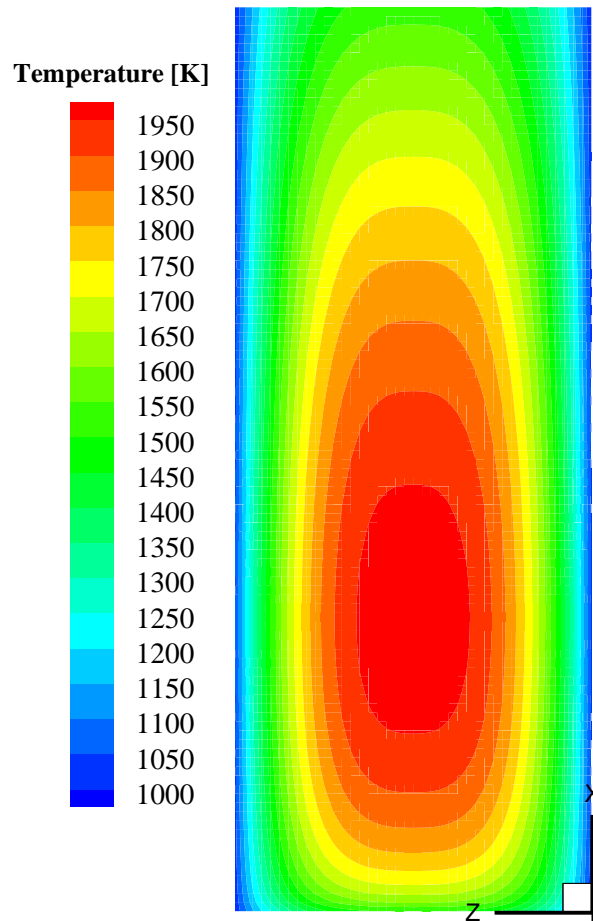


Figure 11: Temperature distribution in the three considered test cases.

### 3.2.1 Results and discussion

The simulation results were calculated with the discrete ordinates method (DOM) and  $T_7$  for angular discretization. A uniformly distributed grid of  $101 \times 41 \times 41$  control volumes was used for all the cases and all the radiation models considered. A mesh independence study revealed that the presented results are independent of the grid resolution, since a finer spatial discretization has a negligible influence on the simulation results.

#### 3.2.1.1 Case 1 (air-fuel combustion)

First the air-fired test case with a pressure path length of 13 bar m is investigated to evaluate the accuracy of the considered gas radiation models. The benchmark results, calculated with the NBCK model and the updated EM2C model parameters of Rivière and Soufiani [81], for the axial distribution of the radiative source term along the furnace centerline are compared with those of the approximate models in Figure 12. Two maxima can be observed, the first occurs at an axial position of about  $x = 16 \text{ m}$ , where the highest temperature of 1980 K is encountered. The second one close to the exit of the domain is due to the temperature difference of 300 K between the last control volume (1523 K) and the exit of

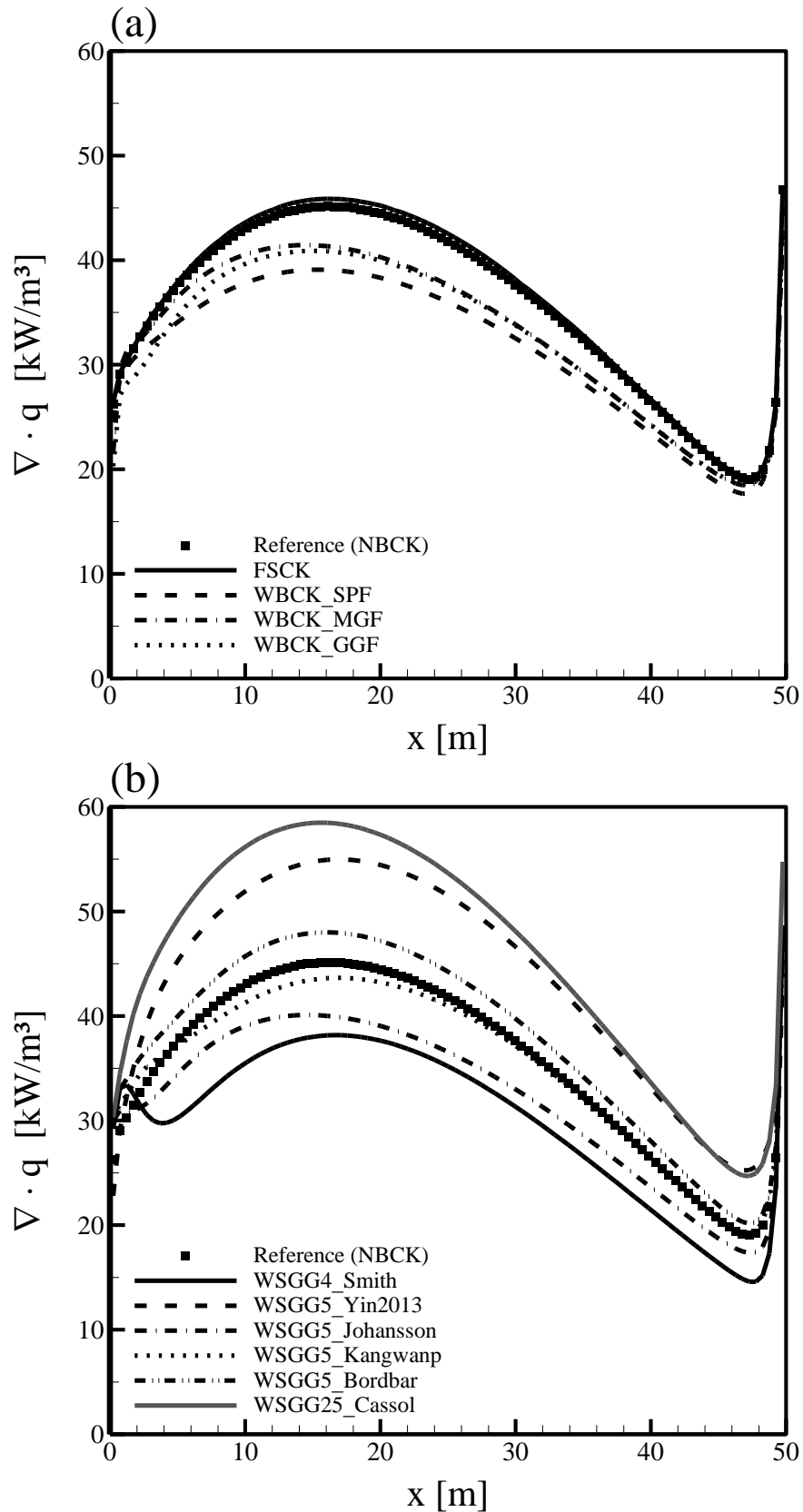


Figure 12: Axial distributions of the radiative source term along the centerline calculated by (a) the considered correlated-k models and (b) WSGG models with the NBCK benchmark solution for Case 1.

the domain, modelled as a black wall at 1223 K. The results of the FSCK model, depicted in Figure 12(a), are in very good agreement with the benchmark solution, slightly over-predicting the magnitude of the radiative source term around the first maximum at  $x = 16\text{ m}$  by about 2%. The WBCK models based on the EWBM database (WBCK\_SPF, WBCK\_MGF and WBCK\_GGF) predict the first maximum upstream of the peak temperature at about  $x = 14\text{ m}$ , Figure 12(a). The magnitude of the radiative source term at  $x = 16\text{ m}$ , where the maximum of the NBCK solution occurs, is under-predicted by approximately 13%, 8% and 10% with the WBCK\_SPF, WBCK\_MGF and WBCK\_GGF models, respectively. These results show that this version of the WBCK model can be considered for air-fired combustion applications with acceptable error. Furthermore, the optimization procedure is well suited to yield similar accuracy for the optimized WBCK models (WBCK\_MGF/GGF) with a higher computational efficiency in comparison to the more expensive WBCK\_SPF model.

The axial radiative source term distributions computed with the different WSGG parameter sets are given in Figure 12(b). These results show clearly that the different sets of parameters can lead to different solutions. The WSGG5\_Kangwanp parameter set yielded the best agreement with the benchmark data, slightly under-predicting the magnitude of the first source term maximum at  $x = 16\text{ m}$  by about 3%. The WSGG5\_Bordbar model is slightly less accurate, leading to an over-prediction of the magnitude of the maximum source term by about 6%. The WSGG5\_Johansson model shows higher deviations from the benchmark data. The first maximum is predicted at the axial centerline position about  $x = 14\text{ m}$ , upstream of the expected position at  $x = 16\text{ m}$ . Thus, the maximum value is underestimated by 11%. The higher deviations of the WSGG5\_Johansson model in comparison to the WSGG5\_Bordbar and WSGG5\_Kangwanp models could stem from the different underlying databases. The WSGG5\_Johansson parameter set was derived from the older EM2C database of Soufiani and Taine [97], whereas Bordbar et al. (2014) [53] and Kangwanpongpan et al. (2012) [51] used the new HITEMP 2010 spectroscopic database [80] to determine their WSGG parameter sets. The older EM2C database shows higher errors especially in predicting the total emissivity for  $\text{CO}_2$  when compared to LBL results based on the HITEMP 2010 spectroscopic database for higher pressure path length products. The WSGG4\_Smith model correctly predicts the axial position of the first maximum of the radiative source term at about  $x = 16\text{ m}$ , but under-predicts the absolute value by approximately 16%. In contrast to the other gas radiation models, an oscillation of the radiative source term can be observed for the WSGG4\_Smith model at the inlet of the furnace. This behavior is likely caused due to the fact that the

parameters were derived from the older EWBM database for only two distinct molar ratios of 1 and 2, whereas a linear interpolation is used in this work to account for variable mole fractions. Furthermore, the validation range of these parameters is limited to pressure path lengths up to 10 bar m. Both restrictions are violated in the present test cases. It is interesting to notice the different behavior of the WSGG5\_Yin2013 model in comparison to the WSGG4\_Smith model, as it is also based on the EWBM database but refined for a broader application range. WSGG5\_Yin2013 over-predicts the magnitude of the first maximum and generally the trend of the radiative source term by about 22 %. Although the parameter set for WSGG25\_Cassol was derived from comparison with the recent HITEMP 2010 spectroscopic database and requires to solve about 5 times more RTEs (25 RTE in total) than the other WSGG models, the predictions obtained with this model exhibit a poor agreement with the reference solution for the investigated air-fired test case. The magnitude of the first maximum of the radiative source term is over-predicted by about 30 %.

The net wall heat fluxes in radial direction  $y$  along the axial centerline of the side wall at  $y = 0 \text{ m}$  and  $z = 10 \text{ m}$  are depicted in Figure 13 for all considered radiation models. As expected, the net wall heat flux increases with rising temperature, reaching its peak value slightly downstream of the axial location of the highest temperature and then decreases towards the exit of the virtual furnace. The FSCK model results show a very good agreement with the benchmark solution, slightly over-predicting the peak value at  $x = 19 \text{ m}$  by approximately 2 %. The WBCK\_SPF/MGF/GGF models underestimate the peak value of the net wall heat flux by about 11 %, 8 % and 10 %, respectively. Noteworthy is that the optimized WBCK\_MGF/GGF show a similar accuracy as the WBCK\_SPF, although only 7 and 4 basic absorption coefficients in contrast to 288 are considered, respectively.

Figure 13(b) illustrates the simulation results of the WSGG models for the net wall heat flux distributions and similar observations can be made to those for the radiative source term distributions in Figure 12(b). The results of the WSGG5\_Kangwanp model are in very good agreement with the benchmark data, under-predicting the peak value by approximately 2 %. The WSGG5\_Bordbar results show a slightly higher deviation of +4 % for the peak value at  $x = 19 \text{ m}$ . The WSGG5\_Johansson model under-predicts the maximum value of the net wall heat flux by about 13 %. This is likely due to the use of an older underlying database [97] to derive the WSGG parameters. The WSGG4\_Smith model correctly reproduces the trend of the net wall heat flux distribution, but strongly underestimates the peak value by approximately 21 %. The reason for this behavior may be attributed to the limited range of the pressure path

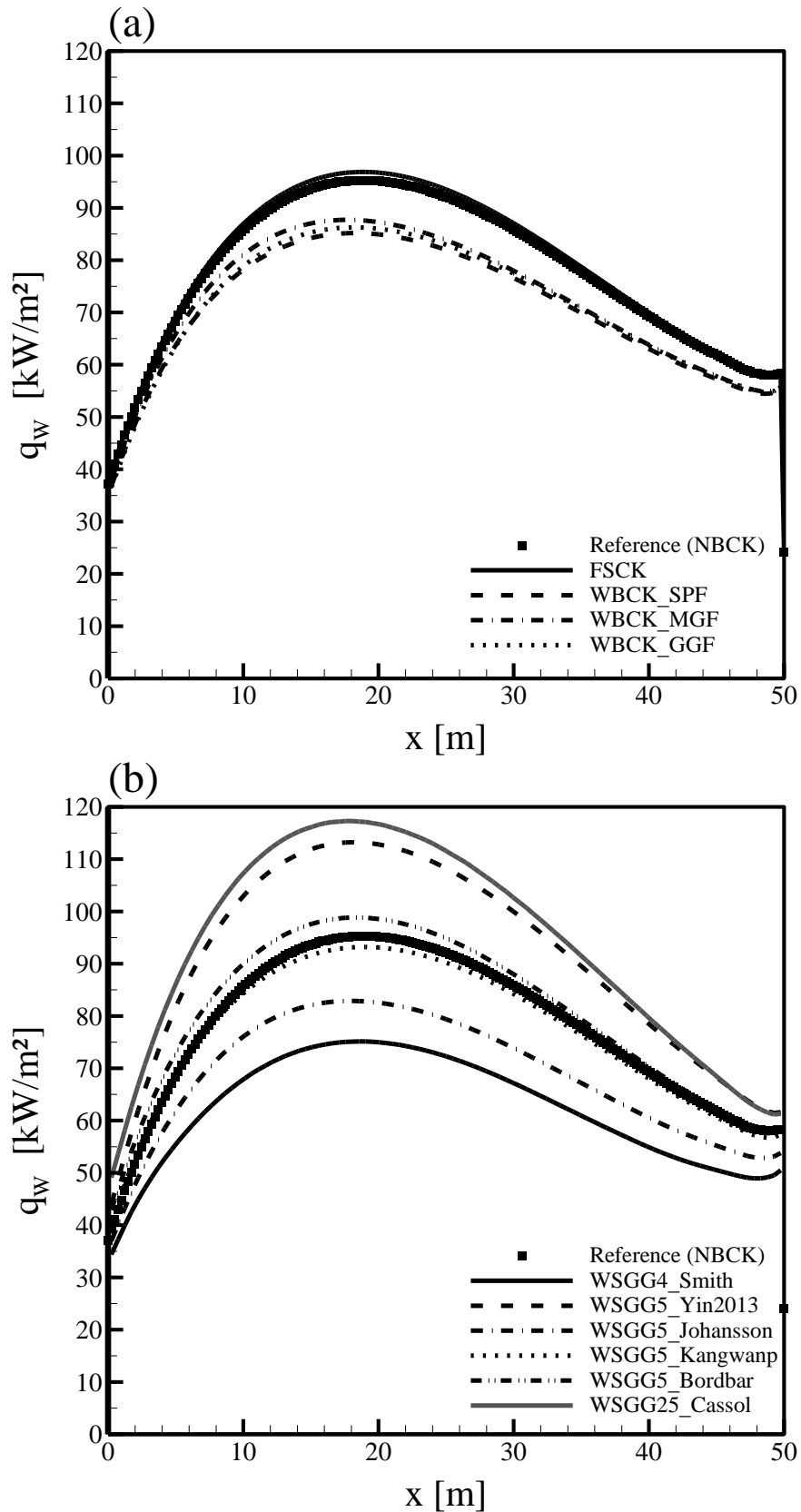


Figure 13: Distributions of the net wall heat flux in radial direction  $y$  along the centerline of the side wall at  $y = 0$  m and  $z = 10$  m calculated by (a) the considered correlated- $k$  and (b) WSGG models with the NBCK benchmark solution for Case 1.

length product up to only 10 bar m of its parameter set. In contrast, the WSGG5\_Yin2013 model over-predicts the net wall heat fluxes with a deviation of about 19 % for the maximum value, although its parameters were also derived from the EWBM as the WSGG4\_Smith parameters, but for longer pressure path lengths up to 60 bar m. Even so the parameter set derived for the WSGG25\_Cassol model is based on the HITEMP 2010 database, the simulation results of this model exhibit a high overestimation of the benchmark solution by about 23 % for the peak value at  $x = 19 m$ .

### 3.2.1.2 Case 2 (oxy-fuel combustion with dry recycle)

Case 2 represents a virtual furnace with oxy-fuel combustion and dry flue gas recirculation. The oxidizer at the inlet consists of about 71 % CO<sub>2</sub>. The pressure path length product in this case is much larger to reach about 55 bar m (about 4 times higher than for that in air-combustion), but the H<sub>2</sub>O/CO<sub>2</sub> molar ratio is reduced by a factor of 8 leading to values between 0.01 and 0.1. Regarding the source term distribution along the axial centerline of the virtual furnace, given in Figure 14, three maxima can be observed, instead of two, as well as increased magnitude of source term (about 16 % higher for the maximum value at  $x = 16 m$ ) in comparison to the air-fired test case. The first maximum at the entry of the virtual furnace ( $x = 0 m$ ) is caused by the high concentration of CO<sub>2</sub> in the new oxidizer mixture. The causes for the other two maxima are the same as those discussed for Case 1. The FSCK model results, depicted in Figure 14(a), are in good agreement with the benchmark solution with only a slight over-prediction of the second maximum at  $x = 16 m$  by approximately 2 %. The application of the EWBM database for the WBCK model results in significant loss of accuracy in an oxy-fuel combustion atmosphere with dry recycle. The WBCK\_SPF/MGF/GGF models not only predict flattened source term distributions along the axial centerline, but also significantly under-predict the magnitude of the source term at  $x = 16 m$ . The deviations of WBCK\_SPF/MGF/GGF are about 25 %, 24 % and 26 %, respectively. The poor performance of the WBCK models can be attributed to the use of the somewhat outdated EWBM database.

The use of the different WSGG parameter sets implies, as also observed for Case 1, a broad range of accuracy regarding the prediction of the radiative source terms under oxy-fuel combustion with dry recycle, as can be seen in Figure 14(b). The WSGG25\_Cassol model is able to capture the sharp gradients, but overestimates the magnitude of the radiative source term with a deviation of approximately 19 % for the maximum value at  $x = 16 m$ . The results of the WSGG5\_Kangwanp model are in best agreement with the benchmark solution among the investigated WSGG parameter sets. The magnitude of the second maximum value is

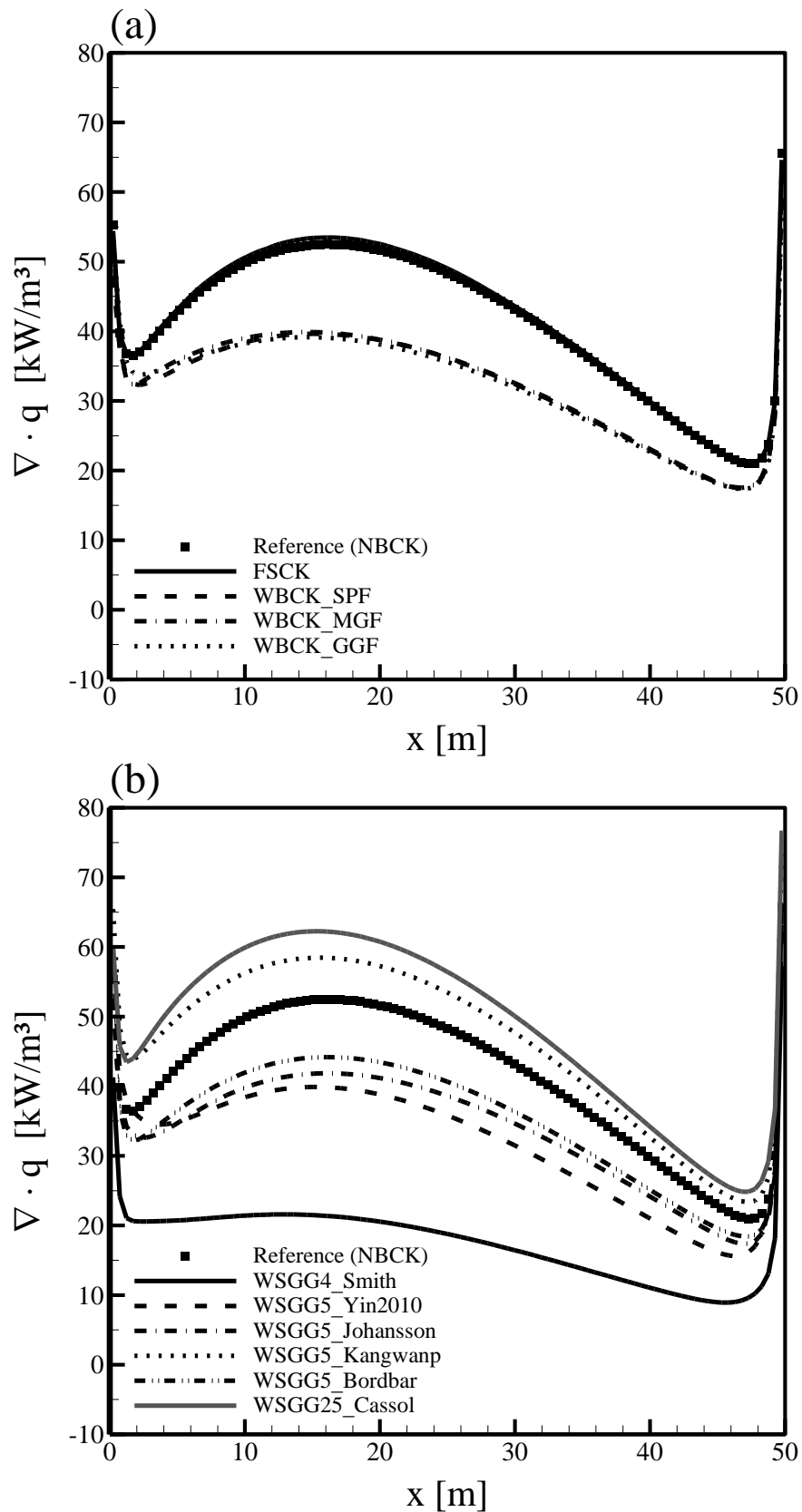


Figure 14: Axial distributions of the radiative source term along the centerline calculated by (a) the considered correlated-k models and (b) WSGG models with the NBCK benchmark solution for Case

overestimated by about 11 %. In contrast, the WSGG5\_Bordbar model under-predicts the magnitude of the maximum value at  $x = 16 \text{ m}$  with a difference of about 16 %, though both parameter sets were derived from the HITEMP 2010 spectroscopic database. A comparison between the emissivity for pressure path lengths higher than 20 bar m computed with the WSGG5\_Kangwanp and WSGG5\_Bordbar models shows that the former model provides predictions in better agreement with LBL solutions computed with HITEMP 2010. This can explain the better performance observed in this case for the WSGG5\_Kangwanp model. The use of the WSGG5\_Johansson model leads to even higher deviations of about 20 % from the benchmark data at  $x = 16 \text{ m}$ . The higher deviations could be partly caused by the encountered molar ratios, which are lower than 0.125 and, thus, outside of the range used to derive the WSGG5\_Johansson parameter set. Furthermore, the different underlying database could also lead to higher differences. As for the WBCK formulations based on the EWBM (see Figure 14(a)), the results obtained with the WSGG parameter sets derived from this database (WSGG5\_Yin2010 and WSGG4\_Smith) also strongly under-predict the magnitude of the radiative source term. Deviations of 24 % and 59 % can be observed for the WSGG5\_Yin2010 and WSGG4\_Smith models at  $x = 16 \text{ m}$ , respectively. Besides the different database, the parameter sets of the WSGG4\_Smith model were derived for air-combustion and up to only 10 bar m, which seem to be the main reasons for its very large error.

The net radiative wall heat fluxes in radial direction along the centerline of the side wall at  $y = 0 \text{ m}$  and  $z = 10 \text{ m}$ , depicted in Figure 15, for oxy-fuel conditions with dry recycle also increase compared to the air-fired case by about 15 % for the maximum value. Figure 15(a) shows that, as for Case 1, the FSCK model leads to only a slight over-prediction of the net wall heat fluxes by about 1 % for the maximum value at  $x = 18 \text{ m}$ . This is once again quite remarkable, since the FSCK model is much more computationally efficient than the NBCK reference model. The different formulations of the WBCK model under-predict the peak value of the radiative heat flux by about 25 %, 25 % and 24 % for the WBCK\_SPF/MGF/GGF models, respectively. As for Case 1, the optimization procedure strongly reduces the computational effort while maintaining the accuracy of the much more expensive WBCK\_SPF model.

The results of the WSGG models for the net radiative wall heat flux distributions along the centerline of the side wall at  $y = 0 \text{ m}$  and  $z = 10 \text{ m}$  are given in Figure 15(b). As expected from the radiative source term distributions in Figure 14(b), the radiative flux distributions of the WSGG5\_Kangwanp and WSGG25\_Cassol models over-predict the benchmark data by approximately 6 % and 10 % at the axial position  $x = 18 \text{ m}$ , respectively. The WSGG5\_Bordbar

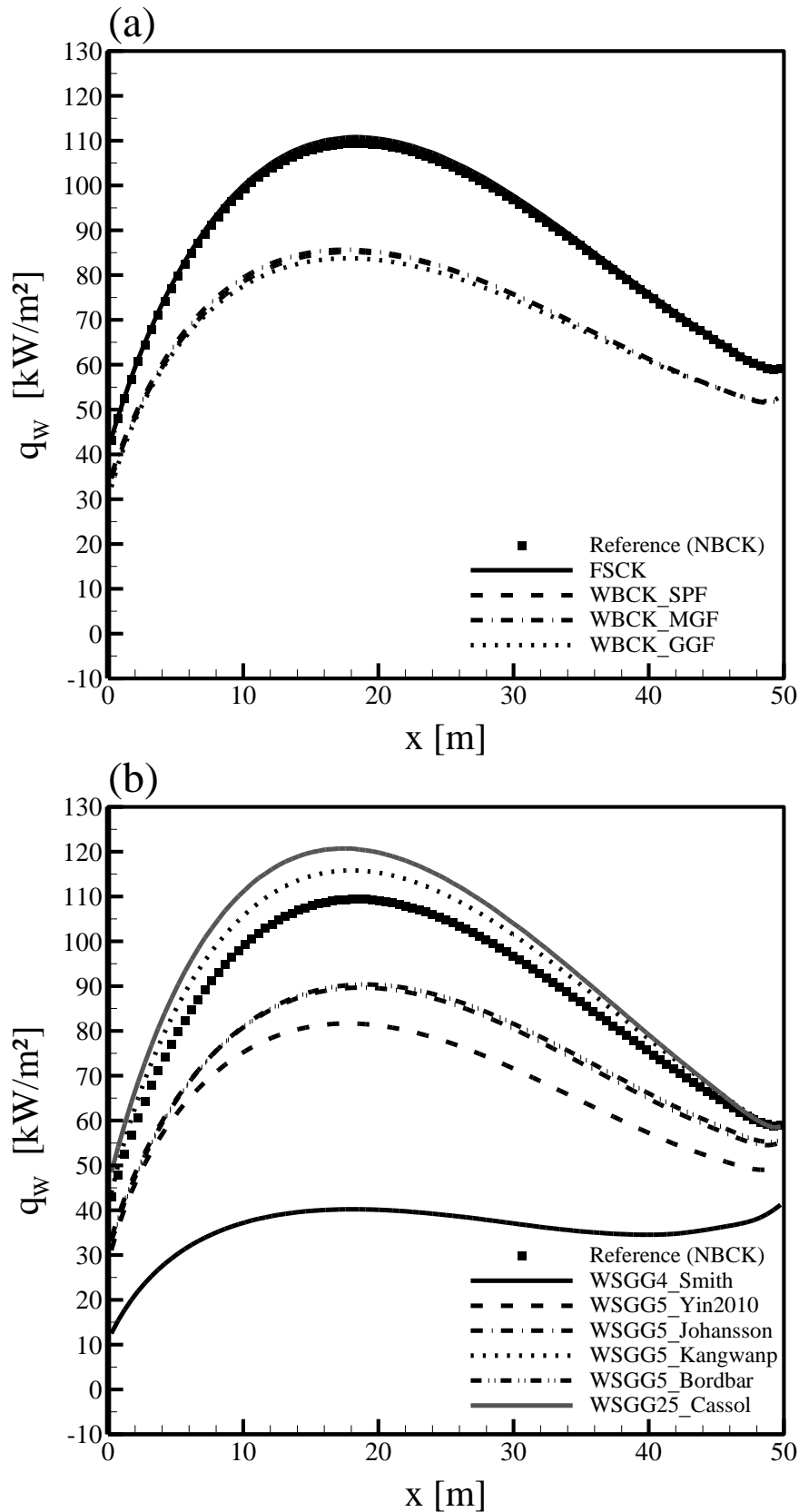


Figure 15: Distributions of the net wall heat flux in radial direction  $y$  along the centerline of the side wall at  $y = 0$  m and  $z = 10$  m calculated by (a) the considered correlated- $k$  and (b) WSGG models with the NBCK benchmark solution for Case 2.

and WSGG5\_Johansson models underestimate the maximum value at  $x = 18\text{ m}$  by about 18 %. The WSGG5\_Yin2010 model captures the general trend, but underestimates the peak value by about 25 %. The older WSGG4\_Smith model is not able to reproduce the correct trend of the wall heat flux and a severe underestimation of 63 % can be observed for the peak value.

### 3.2.1.3 Case 3 (oxy-fuel combustion with wet recycle)

The mole fraction distributions of  $\text{CO}_2$  and  $\text{H}_2\text{O}$  in Case 3 resemble typical oxy-fuel conditions with wet flue gas recycle. The oxidizer at the inlet is composed of a mixture of approximately 51 %  $\text{CO}_2$  and 24 %  $\text{H}_2\text{O}$ . In comparison to Case 2, the pressure path length is also about 55 bar m, but the  $\text{H}_2\text{O}/\text{CO}_2$  molar ratios are strongly enhanced by a factor of 10 for the minimum value at 0.446 and by 5 for the maximum value at 0.5. The axial distributions of the radiative source term are illustrated in Figure 16. From the benchmark solution, calculated by the NBCK model based on the updated EM2C parameters [81], three maxima can be observed for the same reasons as discussed in Case 2. The higher amount of  $\text{H}_2\text{O}$  further enhances the magnitude of the source term at  $x = 15\text{ m}$  by about 48 % relative to that of the air-fired Case 1. Similar to the other two test cases, the FSCK model is in very good agreement with the benchmark solution with the value of the second maximum at  $x = 15\text{ m}$  showing less than 1 % deviation. With the presence of higher  $\text{H}_2\text{O}$  mole fractions, further loss of accuracy can be observed for the WBCK\_SPF/MGF/GGF models. The magnitude of the second maximum at  $x = 15\text{ m}$  is strongly underestimated by approximately 33 % and 31 % for the WBCK\_SPF and WBCK\_MGF/GGF models, respectively.

In contrast to the other two test cases, the results of the WSGG25\_Cassol model for the radiative source term, given in Figure 16(b), are in overall good agreement with the benchmark solution, underestimating the second maximum at  $x = 15\text{ m}$  by only about 2 %, though some larger errors can be observed between  $x = 1\text{ m}$  and  $x = 4\text{ m}$ . Taking into account the performance in the other two cases and the fact that the parameters are valid for pressure path lengths up to only 10 bar m, the good performance of WSGG25\_Cassol in Case 3 seems to be a coincidence. The results of the WSGG5\_Kangwanp and WSGG5\_Bordbar models show a similar agreement with the benchmark data. They under-predict the value of the second maximum by about 3 % and 5.5 %, respectively. The reason for the better performance of the WSGG5\_Kangwanp model is likely, again, due to the better prediction of the gas emissivity for longer pressure path lengths. Compared to Case 2 in Figure 14(b), the WSGG5\_Johansson model shows poorer accuracy for oxy-fuel combustion with wet recycle. It can be seen in Figure 16(b) that the maximum at the axial position  $x = 15\text{ m}$  is underestimated by approximately

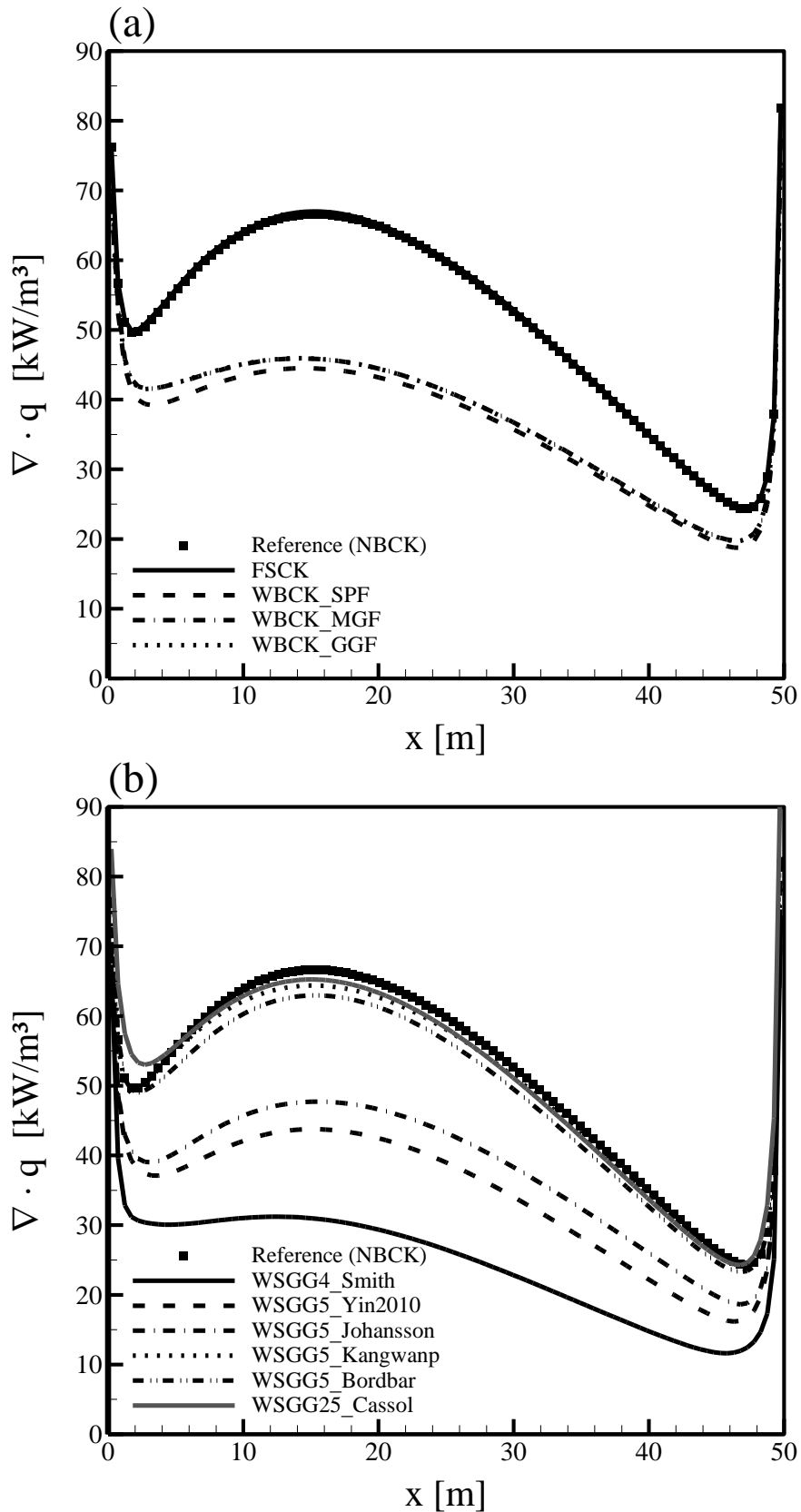


Figure 16: Axial distributions of the radiative source term along the centerline calculated by (a) the considered correlated-k models and (b) WSGG models with the NBCK benchmark solution for Case 3.

28 %. This behavior is likely a consequence of using the older database [97] to derive the parameter set, since it shows higher errors in estimating the total emissivity of CO<sub>2</sub> for higher pressure path lengths. The two WSGG models based on the EWBM database, i.e., WSGG5\_Yin2010 and WSGG4\_Smith, perform the worst and under-predict the maximum radiative source term by about 34 % and 53.5 %, respectively.

In Figure 17(a) contour plots of the radiative source term of the benchmark solution calculated by the NBCK model are provided for the central plane at the radial position  $y = 10 \text{ m}$ . The maximum values of  $82.15 \text{ kW/m}^3$  are located at the exit of the furnace at the radial positions  $z = 8.5 \text{ m}$  and  $z = 11.5 \text{ m}$ , since at these two locations the temperature difference between the exit, the side walls and the inner region are very high and the concentrations of radiating gases are the highest. Furthermore, in Figure 17(b)-(e) the normalized error of the FSCK, WBCK\_MGF, WSGG5\_Kangwanp and WSGG5\_Bordbar models are given, respectively, to illustrate the overall performance of these models. The normalized error of the radiative source term  $\Delta_{n,div}$  was calculated as

$$\Delta_{n,div} = \frac{\nabla \cdot q_{NBCK} - \nabla \cdot q_{Model}}{\nabla \cdot q_{NBCK,max}}, \quad (118)$$

where  $\nabla \cdot q_{NBCK}$ ,  $\nabla \cdot q_{NBCK,max}$  and  $\nabla \cdot q_{Model}$  are the radiative source terms of the NBCK model, its peak value and the considered gas radiation model. According to Figure 17(b) the FSCK model shows the best agreement with deviations less than 2 %. The WBCK\_MGF model shows the highest deviations among the gas radiation models within the central plane with up to about 25 % at the axial position  $x = 16 \text{ m}$ , confirming the results along the furnace centerline given in Figure 16(a) that the radiative source terms are strongly under-predicted. As can be observed in Figure 17(d) and (e), the WSGG5\_Kangwanp and WSGG5\_Bordbar model results, respectively, show a quite good agreement with the benchmark solution with maximum errors lower than 4.5 % for the majority within the furnace.

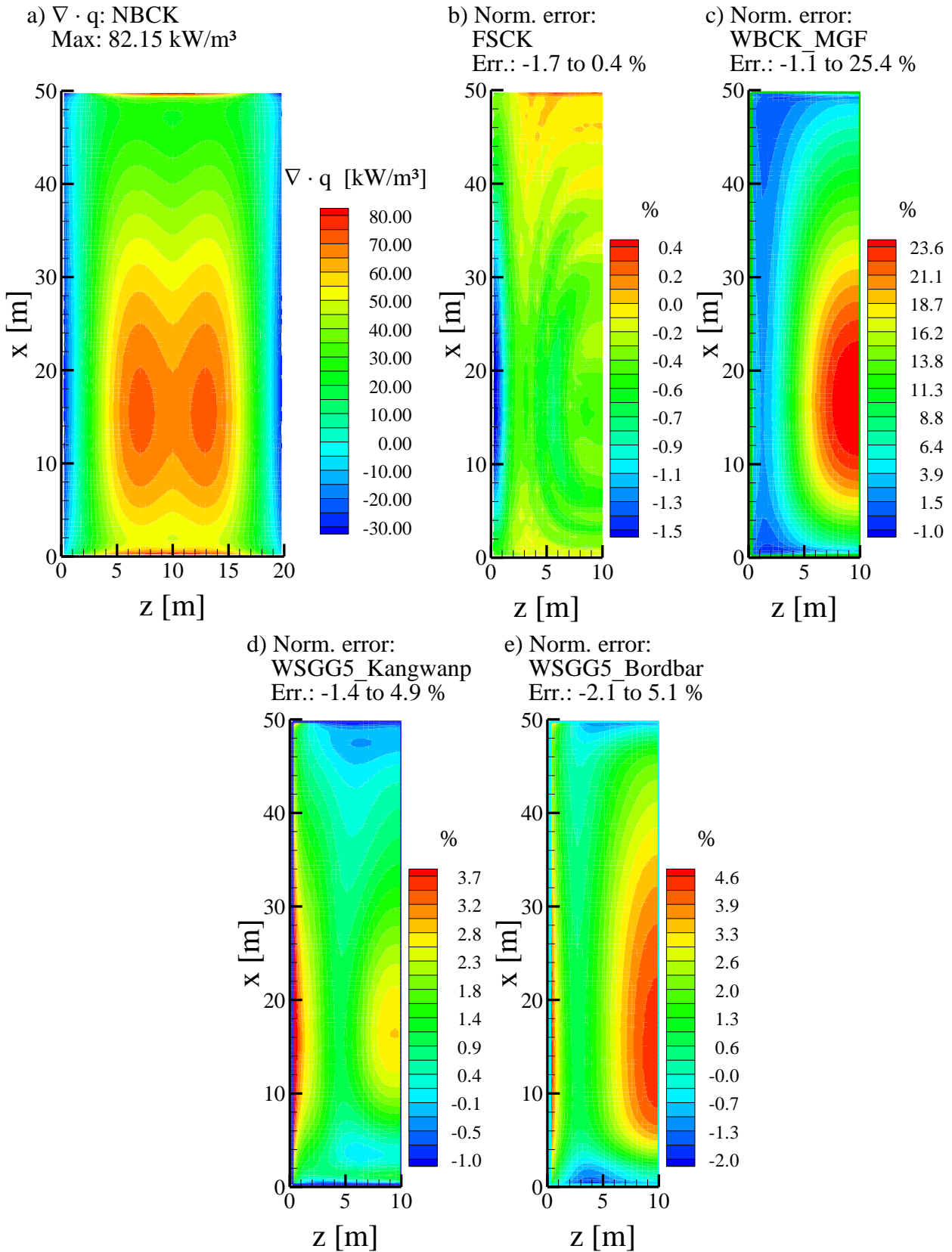


Figure 17: Reference solution of the radiative source term calculated by the NBCK model (a) and the normalized error of the FSKC (b), WBCK\_MGF (c), WSGG5\_Kangwanp (d) and WSGG5\_Bordbar (e) models for the central plane at the radial position  $y = 10 \text{ m}$ .

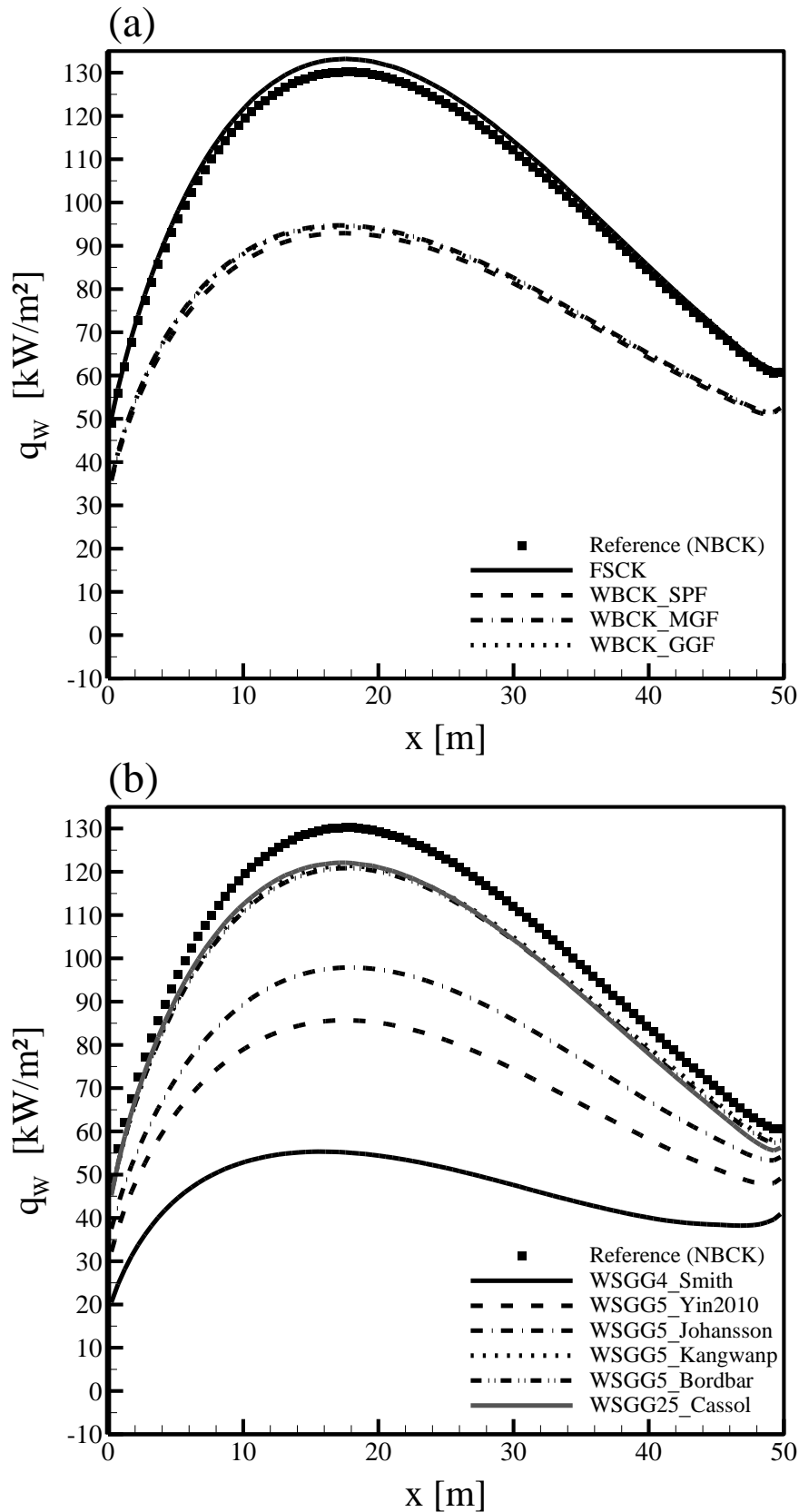


Figure 18: Distributions of the net wall heat flux in radial direction  $y$  along the centerline of the side wall at  $y = 0$  m and  $z = 10$  m calculated by (a) the considered correlated- $k$  and (b) WSGG models with the NBCK benchmark solution for Case 3.

Regarding the net radiative heat flux distribution in radial direction  $y$  along the axial centerline at the side wall with  $y = 0 \text{ m}$  and  $z = 10 \text{ m}$  in Figure 18, a further increase of the maximum value at  $x = 18 \text{ m}$  by about 37 % with respect to Case 1 can be observed. The FSCK model only slightly overestimates the net wall heat flux distributions and the maximum value at  $x = 18 \text{ m}$  by approximately 2 %. In contrast, the WBCK\_SPF/MGF/GGF models strongly under-predict the maximum radiative net wall heat flux by about 29 %, 27 % and 28 %, respectively.

The net radiative wall heat flux distributions of the WSGG models are illustrated in Figure 18(b). The best agreement with the benchmark solution among the investigated WSGG parameter sets is observed for the WSGG25\_Cassol, WSGG5\_Kangwanp and WSGG5\_Bordbar model results, consistent with their good performance for the centerline source term distributions shown in Figure 16(b). The maximum value is underestimated by approximately 6 to 7 %. According to Figure 18(b), the WSGG5\_Johansson model also underestimates the net radiative wall heat flux with a difference of approximately 25 % at the axial position  $x = 18 \text{ m}$ . The same behavior can be observed for the WSGG5\_Yin2010 model, which under-predicts the peak value by about 34 %. As for Case 2, the WSGG4\_Smith model is not able to reproduce the correct trend of the radiative wall heat flux and strongly underestimates the maximum value at  $x = 18 \text{ m}$  by about 58 %.

In Figure 19(a) contour plots of the net radiative wall heat flux of the benchmark solution calculated by the NBCK model are depicted for the side wall at the radial position  $y = 0 \text{ m}$ . In accordance with Figure 18, the maximum value of  $130.20 \text{ kW/m}^2$  is located along the centerline of the furnace at the axial position  $x = 18 \text{ m}$ . In Figure 19(b)-(e) the normalized error of the FSCK, WBCK\_MGF, WSGG5\_Kangwanp and WSGG5\_Bordbar models are shown, respectively, to provide information about their overall performance. The normalized error of the radiative net wall flux  $\Delta_{n,flux}$  was computed as

$$\Delta_{n,flux} = \frac{q_{W,NBCK} - q_{W,Model}}{q_{W,NBCK,max}}, \quad (119)$$

where  $q_{W,NBCK}$ ,  $q_{W,NBCK,max}$  and  $q_{W,Model}$  are the net radiative wall heat fluxes of the NBCK model, its peak value, and the fluxes calculated by other radiation models. As can be seen in Figure 19(b), the predicted net wall fluxes calculated by the FSCK model show the best agreement with the benchmark solution with maximum deviations of less than 3 % along the side wall. The WBCK\_MGF model strongly under-predicts the net radiative wall heat fluxes up to 25 %, which is the highest deviation predicted by the gas radiation models investigated. As

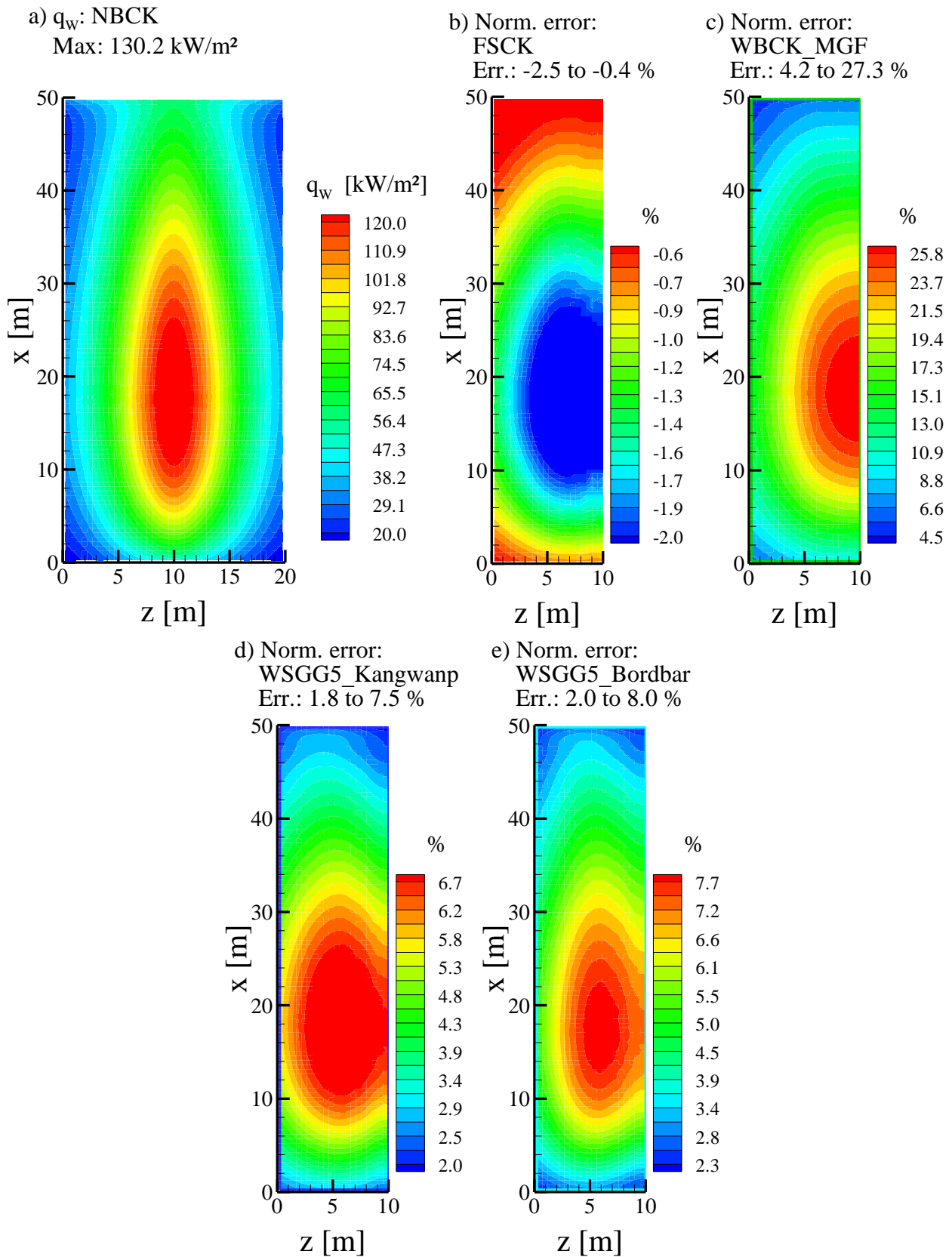


Figure 19: Reference solution of the net wall heat flux in radial direction  $y$  calculated by the NBCK model (a) and the normalized error of the FSCK (b), WBCK\_MGF (c), WSGG5\_Kangwanp (d) and WSGG5\_Bordbar (e) models for the side wall at  $y = 0$  m.

shown in Figure 19(d) and (e), the WSGG5\_Kangwanp and WSGG5\_Bordbar model results display a similar level of agreement with the benchmark solution with maximum errors close to 8 %. The errors decrease in the parts of the side wall closer to the inlet and outlet of the furnace, which also can be observed in the results of the FSCK and WBCK\_MGF models in Figure 19(b) and (c).

### 3.2.1.4 Overall model performance

A qualitative evaluation of the computational cost of the investigated models can be discussed by comparing the number of RTEs solved per angular direction. In Table 6 information about the number of RTEs and the accuracy of the considered gas radiation models is given for each investigated test case. The accuracy is evaluated by means of the mean relative errors  $\Delta_s$  for the radiative source terms along the furnace centerline, and  $\Delta_f$  the radiative net wall heat fluxes along the axial centerline of the side wall at  $y = 0 \text{ m}$  and  $z = 10 \text{ m}$ . The mean relative errors are calculated as:

$$\Delta_s = \sum_1^{101} \left| \frac{\nabla \cdot q_{NBCK,l} - \nabla \cdot q_{Model,l}}{\nabla \cdot q_{NBCK,l}} \right| / 101, \quad (120)$$

$$\Delta_f = \sum_1^{101} \left| \frac{q_{w,NBCK,l} - q_{w,Model,l}}{q_{w,NBCK,l}} \right| / 101, \quad (121)$$

with  $\nabla \cdot q_{NBCK,l}$ ,  $\nabla \cdot q_{Model,l}$ ,  $q_{w,NBCK,l}$  and  $q_{w,Model,l}$  being the radiative source terms and net wall heat fluxes of the reference NBCK model and the considered radiation models at each axial position  $l$ , respectively.

Table 6: The number of transfer equations per direction,  $n_t$ , and the mean relative errors of the radiative source term,  $\Delta_s$ , and the radiative wall heat flux,  $\Delta_f$ , of the considered radiation models for the investigated test cases of the 3D coal-fired virtual furnace

Model	$n_t$	$\Delta_s$ (%)	$\Delta_f$ (%)
	Case 1/ 2/ 3	Case 1/ 2/ 3	Case 1/ 2/ 3
NBCK	3150/3150/3150	-/-/-	-/-/-
FSCK	10/ 10/ 10	1.2/ 1.1/ 0.4	1.3/ 1.0/ 1.9
WBCK_SPF	288/ 270/ 284	11.2/ 21.5/ 28.8	9.1/ 19.8/ 25.6
WBCK_MGF	7/ 7/ 7	7.4/ 21.3/ 26.5	7.0/ 19.4/ 24.3
WBCK_GGF	4/ 4/ 4	8.6/ 22.1/ 26.6	8.4/ 20.7/ 24.5
WSGG4_Smith	4/ 4/ 4	16.9/ 57.4/ 51.9	20.0/ 58.3/ 53.8
WSGG5_Yin2013/2010	5/ 5/ 5	22.7/ 23.3/ 32.9	16.0/ 23.9/ 31.9
WSGG5_Johansson	5/ 5/ 5	10.4/ 18.4/ 25.9	11.9/ 16.0/ 22.3
WSGG5_Kangwanp	5/ 5/ 5	2.1/ 12.0/ 2.1	1.8/ 5.0/ 6.0
WSGG5_Bordbar	5/ 5/ 5	6.4/ 14.8/ 5.2	3.3/ 15.3/ 6.7
WSGG25_Cassol	25/ 25/ 25	28.4/ 17.8/ 3.4	19.7/ 8.3/ 6.5

The most accurate model is the FSCK based on the updated parameters of Rivière and Soufiani [81], which predicts the radiative source term and the net wall heat fluxes within a mean relative error of less than 2 % for all the three test cases. This accuracy is remarkable, since only 10 RTEs have to be solved in comparison to 3150 for the reference NBCK model. However, it should be kept in mind that the major computational overhead of this model, besides solving the RTEs, is the computation of suitable cumulative distribution functions for the CO<sub>2</sub>-H<sub>2</sub>O mixtures in each control volume, which have to be generated from the updated SNB parameters. Nevertheless, the computational effort of this procedure is significantly reduced by generating a prescribed database for the encountered temperatures and mole fractions in the test cases [19].

For the WBCK models based on the EWBM database, mean relative errors between 21 % and 29 % are observed for the oxy-fuel combustion test cases, even so the computational effort is higher (WBCK\_SPF) or similar (WBCK\_MGF/GGF) as for the FSCK model.

Concerning the WSGG models, a wide range of disparity is observed among the different sets of parameters. For the two oxy-fuel combustion test cases, the WSGG5\_Kangwanp and WSGG5\_Bordbar are found to be the most reliable with maximum mean relative errors of 10 % and 19 %, respectively. The WSGG5\_Johansson and WSGG5\_Yin models showed higher mean deviations up to 29 % and 36 %. The aforementioned test cases also reveal that the range of pressure path length products used to obtain and validate the WSGG parameter sets should be wide enough to cover those encountered in real-sized combustors. Therefore, it is important to consider longer path lengths relevant to real-sized boilers and to provide the corresponding benchmarks in evaluation of the performance of different gas radiation models to recommend the appropriate WSGG parameter sets for CFD simulations.

### 3.2.2 Conclusions

In this subsection, the performance of several gas radiation models was investigated for three 3D test cases with path lengths typical for industrial scale coal-fired furnaces. The same non-uniform temperature distribution was specified in all cases, whereas the inhomogeneous distributions of CO<sub>2</sub> and H<sub>2</sub>O mole fractions were varied to resemble typical conditions for air (Case 1) and oxy-fuel combustion with dry (Case 2) and wet (Case 3) flue gas recirculation. The benchmark solutions were provided by the NBCK model based on the updated EM2C parameters [81] to investigate the performance of gas radiation models at path lengths up to 55 m at atmospheric pressure. Supporting the findings made in [41] and Subsection 3.1, it was found again under conditions of higher dimensions and, thus, longer path lengths as well as

inhomogeneous gas concentrations and non-isothermal temperature profiles that the most accurate gas radiation model is the FSCK model based on the updated EM2C SNB parameters of Rivière and Soufiani [81], which predicted the radiative source terms and net wall heat fluxes with less than 2 % mean relative deviation from the benchmark solution. The use of a pre-generated database further improves the computational efficiency. Thus, the FSCK model is recommended for calculating the radiative heat transfer in CFD simulations of practical large-scale oxy-fuel combustion systems.

Regarding the WBCK formulations, the present results confirm the conclusions given in Subsection 3.1.2 and [28] that the optimized WBCK\_MGF/GGF models have similar accuracy at much higher computational efficiency than the more expensive WBCK\_SPF model. However, higher deviations of up to 29 % from the benchmark solutions are observed for test cases with dimensions of a real coal-fired furnace. Further improvement potential is seen in estimating the limits for the absorption coefficient that were originally optimized for air-firing conditions, see [101], and updating the EWBM parameters using recently released spectroscopic databases like HITEMP 2010.

If the WSGG model is applied to calculate gas radiation heat transfer because of its simple implementation and high computational efficiency, the parameter sets of Kangwanpongpan et al. [51] and Bordbar et al. [53] are recommended for CFD simulations of practical oxy-fuel applications with large pressure path length products and molar ratios of H<sub>2</sub>O to CO<sub>2</sub> between 0.01 and 0.5. Their results of the oxy-fuel test cases showed consistently acceptable agreement with the benchmark solutions among the investigated WSGG parameter sets with maximum mean relative errors of about 15 %. Generally, it can be stated that the accuracy of different WSGG parameter sets, derived especially for oxy-fuel conditions, is dependent on the test conditions and varies significantly among the available parameter sets. Results of the present test cases have revealed that the long path lengths of real-sized boilers and the underlying database used to obtain and validate the WSGG parameter sets strongly influence the accuracy and, thus, care should be taken in applying appropriate parameter sets to accurately predict the heat transfer by gas radiation in real oxy-fuel applications.

The commonly used conventional WSGG parameter set of Smith et al. [82] derived for air-fuel combustion in commercial CFD codes is not recommended for oxy-fuel combustion calculations with either long or short pressure path lengths, since it is often not able to reproduce qualitatively the net wall heat flux distributions and suffers significant error in the radiative source term distributions.

### 3.3 Gas-particle radiation modelling in a 2D virtual oxy-fuel coal-fired furnace with wet recycle

In this subsection, the thermal radiation heat transfer is investigated for a 2D square geometry representing a plane between black walls with a side length  $L$  of 20 m within an idealized oxy-coal combustion furnace. The distributions for the physical quantities (temperature, CO<sub>2</sub> and H<sub>2</sub>O mole fractions, cross-sectional areas per volume for coal/char and ash particles) were derived from an in-house CFD simulation of a real hard-coal boiler fired with air. The considered plane is located slightly above the last burner region to capture the influence of coal/char and ash particles on the radiative heat transfer. As in the former subsection, it is assumed that the temperature distribution of an air-fired boiler remains the same in an oxy-fired boiler. Thus, the following distribution of temperature was derived from the CFD simulations:

$$\begin{aligned} |f_r| \leq 0.85: & \quad T = 1965 \text{ K} - 115 \text{ K} \cdot \left( \cos \left( \frac{|f_r|}{0.85} \cdot \pi \right) + 1 \right) \\ |f_r| > 0.85: & \quad T = 1965 \text{ K} - 115 \text{ K} \cdot \left( \cos \left( \frac{|f_r|}{0.85} \cdot \pi \right) + 1 \right) - 1254 \text{ K} \cdot \left( \frac{|f_r| - 0.85}{0.15} \right)^4, \end{aligned} \quad (122)$$

where the radial factor  $f_r = \min(2r/L, 1)$  is calculated with the radial distance from the central point  $r = \sqrt{(x - L/2)^2 + (y - L/2)^2}$  and the side length  $L$  of the square enclosure. A typical temperature of 693 K is set for the black walls.

CO<sub>2</sub> and H<sub>2</sub>O were considered as the only radiating gaseous species. The corresponding volume fractions from the air-fired CFD simulations were transformed into a possible oxy-fuel combustion scenario with wet flue gas recirculation. The transformation was carried out by weighting the air-fired values with a linear approximation that was defined with appropriate inlet and outlet boundary conditions for the volume fractions of CO<sub>2</sub> and H<sub>2</sub>O, respectively, encountered in typical furnaces with air- and wet oxy-fuel-fired combustion conditions. The following distributions for the CO<sub>2</sub> and H<sub>2</sub>O mole fractions were derived from those values:

$$\begin{aligned} |f_r| \leq 0.4: & \quad Y_{CO_2} = 0.6766 \\ |f_r| > 0.4: & \quad Y_{CO_2} = 0.64 + 0.0366 \cdot \cos \left( \frac{|f_r| - 0.4}{0.6} \cdot \frac{1}{2} \pi \right), \end{aligned} \quad (123)$$

$$\begin{aligned} |f_r| \leq 0.75: & \quad Y_{H_2O} = 0.321 \\ |f_r| > 0.75: & \quad Y_{H_2O} = 0.3168 + 0.0118 \cdot \sin \left( \frac{|f_r| - 0.75}{0.25} \cdot \frac{3}{2} \pi + 0,2\pi \right). \end{aligned} \quad (124)$$

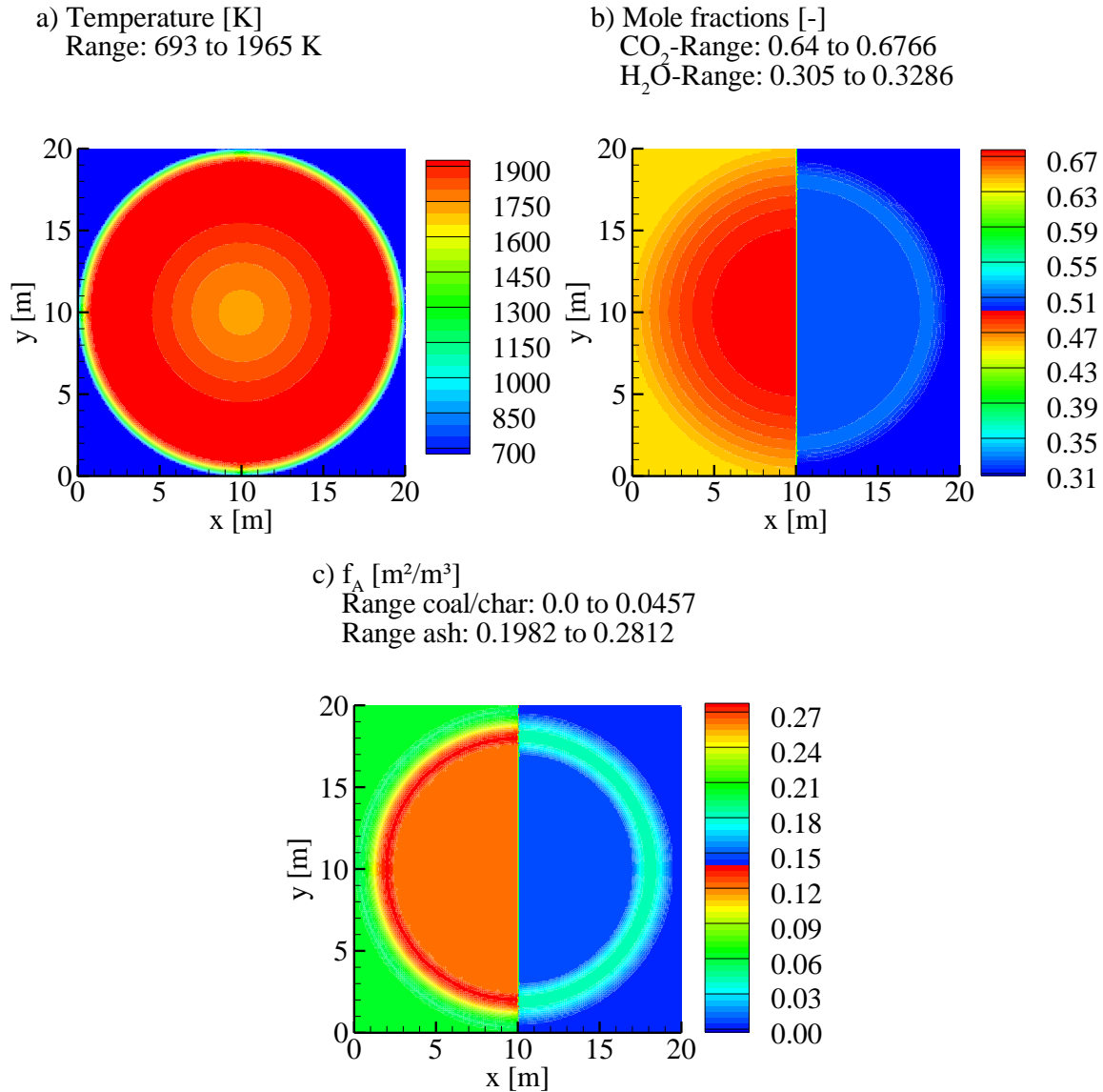


Figure 20: Distributions of temperature (a), gas volume fractions of CO<sub>2</sub> (b, left, upper legend) and H<sub>2</sub>O (b, right, lower legend) as well as cross-sectional area per volume of ash (c, left, upper legend) and coal/char particles (c, right, lower legend) within the enclosure.

Constant particle diameters of 80  $\mu\text{m}$  for coal/char particles and 10  $\mu\text{m}$  for ash particles were used in all simulations. The diameter of the coal/char particles was calculated as the mean Sauter diameter from the discretized diameter distribution obtained with the CFD simulation. Thus, the following distribution of the cross-sectional area per volume of the coal/char particles,  $f_{A,coal}$ , was derived:

$$\begin{aligned}
 |f_r| \leq 0.7: & \quad f_{A,coal} = 0.008 \frac{\text{m}^2}{\text{m}^3} \\
 |f_r| > 0.7: & \quad f_{A,coal} = \left( 0.008 + 0.03 \cdot \sin\left(\frac{|f_r| - 0.7}{0.3} \cdot \frac{3}{2}\pi\right) + 0.022 \cdot \left(\frac{|f_r| - 0.7}{0.3}\right) \right) \frac{\text{m}^2}{\text{m}^3} \quad (125)
 \end{aligned}$$

In accordance with Johansson et al. [67], the mean diameter of ash particles was assumed to be  $10 \mu\text{m}$  and the profile of the cross-sectional area per volume of the ash particles,  $f_{A,ash}$ , was:

$$\begin{aligned} |f_r| \leq 0.75: & \quad f_{A,ash} = 0.265 \frac{\text{m}^2}{\text{m}^3} \\ |f_r| > 0.75: & \quad f_{A,ash} = \left( 0.2397 + 0.0415 \cdot \cos \left( \frac{|f_r| - 0.75}{0.25} \cdot \frac{3}{2} \pi - 0.3\pi \right) \right) \frac{\text{m}^2}{\text{m}^3} \end{aligned} \quad (126)$$

The total pressure is set to 1 atm. For illustration purposes, the distributions of temperature, (a), gas mole fractions, (b), and cross-sectional area per volume of the coal/char and ash particles, (c), are depicted in Figure 20 within the considered enclosure.

### 3.3.1 Results and discussion

The simulation results were calculated with the FVM, since it was shown, e.g. by Boulet et al. [112], to be superior to the DOM when solving the RTE in strongly forward scattering media (as is the case for the considered coal/char and ash particles). Uniformly distributed grids of  $81 \times 81$  spatial and  $8 \times 16$  angular control volumes were used to discretize the spatial and angular computational domain, respectively. Each of the  $8 \times 16$  angular division is subdivided into  $5 \times 5$  sub-angles to satisfy the normalization of the phase function, for further details see e.g. [112], [125], [136]. The solution of the radiative intensity was considered converged, when the following condition was fulfilled:

$$\frac{(I^n - I^{n-1})}{I^n} \leq 10^{-7}, \quad (127)$$

where  $I^n$  is the radiative intensity of the actual iteration and  $I^{n-1}$  is the one of the previous iteration, respectively. A grid resolution study showed that a finer discretization for spatial and/or angular space has a negligible influence on the simulations results with relative error deviations within 1 %.

The accuracy of the approximate models will be assessed by defining a relative error for the radiative source terms,  $\Delta_s$ , and net wall heat fluxes,  $\Delta_f$ , as follows:

$$\Delta_s = \frac{(\nabla \cdot q_{benchmark} - \nabla \cdot q_{model})}{\nabla \cdot q_{benchmark}}, \quad (128)$$

$$\Delta_f = \frac{(q_{w,benchmark} - q_{w,model})}{q_{w,benchmark}}, \quad (129)$$

where  $\nabla \cdot q_{benchmark}$  and  $\nabla \cdot q_{model}$  are the radiative source terms and  $q_{w,benchmark}$  and  $q_{w,model}$  are the net wall heat fluxes of the benchmark and the assessed model, respectively. It is noted here that for calculating the relative errors of the radiative source term  $\Delta_s$ , only locations where

the values fulfilling the condition  $|\nabla \cdot q_{benchmark}| \geq 0.1 \cdot |\nabla \cdot q_{benchmark,max}|$  are considered in order to avoid interpreting discrepancies in regions where the radiative source term is insignificant.

### 3.3.1.1 Influences of various contributions on total radiation

The contributions of scattering, gas and particle radiation are examined in this subsection for the considered test case within the NBCK context. Figure 21 illustrates the radiative source term distributions and the relative errors for the different models within the enclosure. The benchmark results, given in Figure 21(a), are calculated with the NBCK model for the gas radiation and the particle radiative properties computed with Mie theory, hereafter denoted as “Mie-Model”. In accordance with the distributions of the physical quantities (temperature, CO<sub>2</sub> and H<sub>2</sub>O mole fractions, coal/char and ash cross-sectional areas), the radiative source term is axisymmetric. The radiative source term exhibits a maximum value of  $326.1 \text{ kW/m}^3$  in the region where hot particles emit strongly. It decreases as the distance toward the centerline is reduced to reach a negative value of  $-43.5 \text{ kW/m}^3$  at the axis midpoint ( $x = 10 \text{ m}$ ,  $y = 10 \text{ m}$ ). This shows that the center of the domain is dominated by absorption of radiation from combustion gases and ash. Absorption by relatively cold gas and particles prevails also close to the wall and the edges of the domain with values of the radiative source of about to  $-367 \text{ kW/m}^3$ . The simulation results of the “OnlyGas-Model”, which considers solely gas radiation, given in Figure 21(b), are significantly lower than the benchmark solutions in most of the enclosure with exception in the absorbing core, where an over-prediction with a maximum difference of up to about 109.5 % is observed. The mean relative deviation is 41.6 % and the maximum values are under-predicted by about 37.1 %. When only particle radiation is considered, denoted as “OnlyParticle-Model” hereafter, see Figure 21(c), lower mean and maximum relative errors of about 28.5 % and 81.1 %, respectively, are obtained with the highest discrepancies being observed in the region of strong emission.

The “NoScattering-Model” does not account for particle scattering at all, but considers the non-gray absorption and emission by both gases and particles. It can be observed in Figure 21(d) that the relative errors can be up to about -24.7 % in locations, where the total values of the radiative source term are close to the threshold value (the lower limit of radiative source term to be included in the error calculation), whereas the mean relative deviation is about 6.7 %. The maximum values are slightly over-predicted by about 2.0 %. Generally, the absolute values are higher than the benchmark solution, i.e., the “NoScattering-Model” predicts higher emission rates.

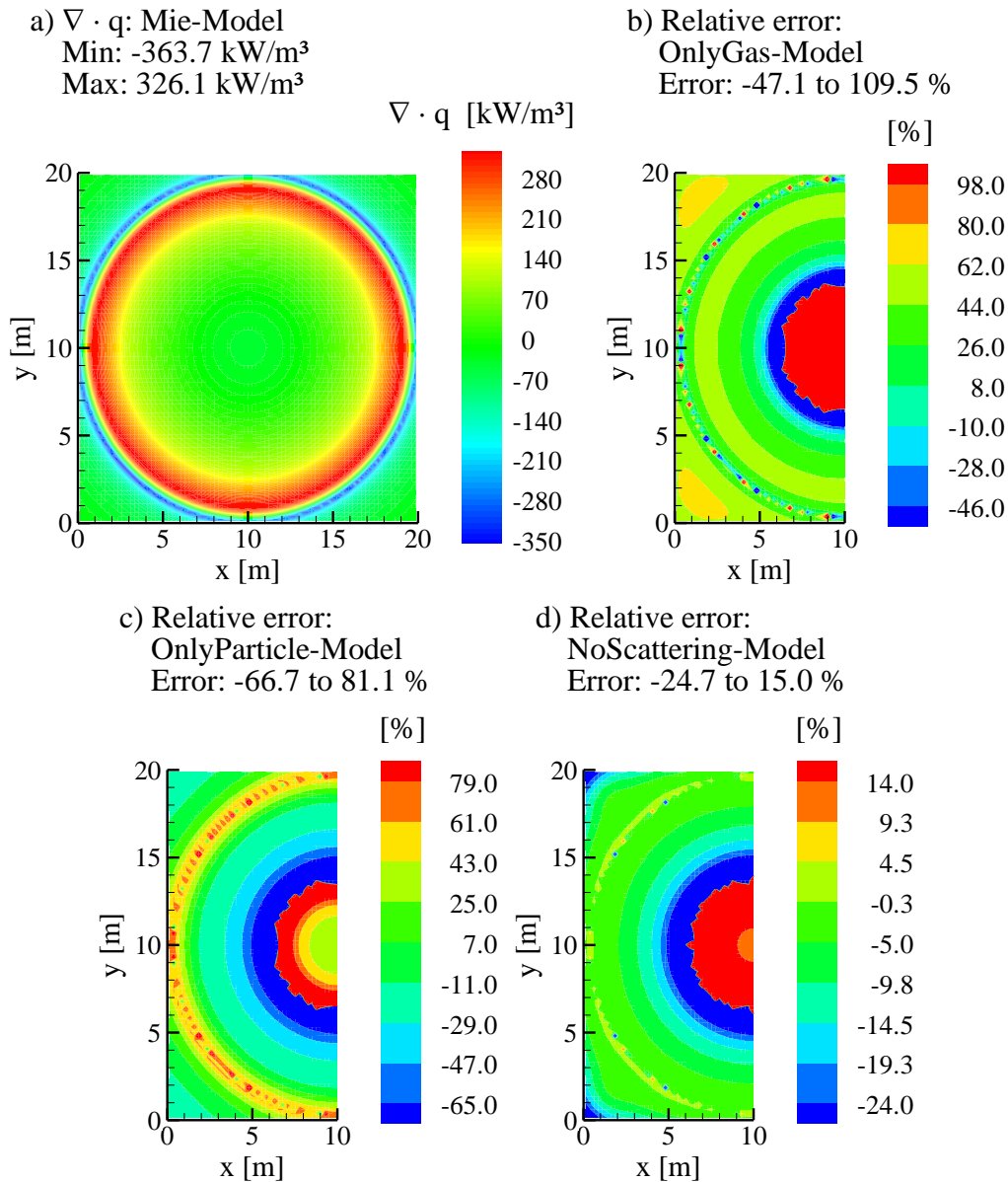


Figure 21: Radiative source term distribution within the enclosure for the NBCK model with Mie phase functions, (a), and relative errors for only gas radiation, (b), only particle radiation, (c), and neglected particle scattering, (d).

The distributions of the net wall heat fluxes are displayed in Figure 22 at the side wall at  $y = 20 \text{ m}$  in  $y$ -direction and the relative errors of the assessed models. For the benchmark solutions of the “Mie-Model”, the net wall heat flux peaks at the midpoint of  $x = 10 \text{ m}$  with a value of  $482.4 \text{ kW/m}^2$ , but decreases to about  $69.3 \text{ kW/m}^2$  at the edges of the side wall.

The “OnlyParticle-Model” strongly overestimates the net heat fluxes due to the neglect of absorption by cold gases located close to the wall. The peak value and minimum values are over-predicted by about 12.9 % and 49.5 %, respectively, and a mean relative error of 31.2 % can be observed. Neglecting the particle radiation limits strongly the emission of the medium

and leads to lower net heat fluxes, as is shown for the “OnlyGas-Model”. The peak value is underestimated by 37.5 %, whereas the values at the corners are similarly over-predicted by about 37.9 % as for the other models, yielding to a mean relative difference of about 23.0 %.

The “NoScattering-Model” over-predicts the net heat fluxes over the whole side wall, with deviations of approximately 6.8 % for the peak value and 40.6 % at the corners and a mean relative error of 14.1 %. This can be related to the higher emission predicted by this model (see Figure 21(d)).

The results of this subsection show that although the radiative heat transfer is dominated by particle radiation the gas radiation has to be considered. It can be also concluded that neglecting scattering by particulate matter leads to higher radiative source terms and net wall heat fluxes, since the process of redistributing radiative intensity by particle scattering is not accounted for, which is especially important for the prediction of the radiative net wall heat fluxes.

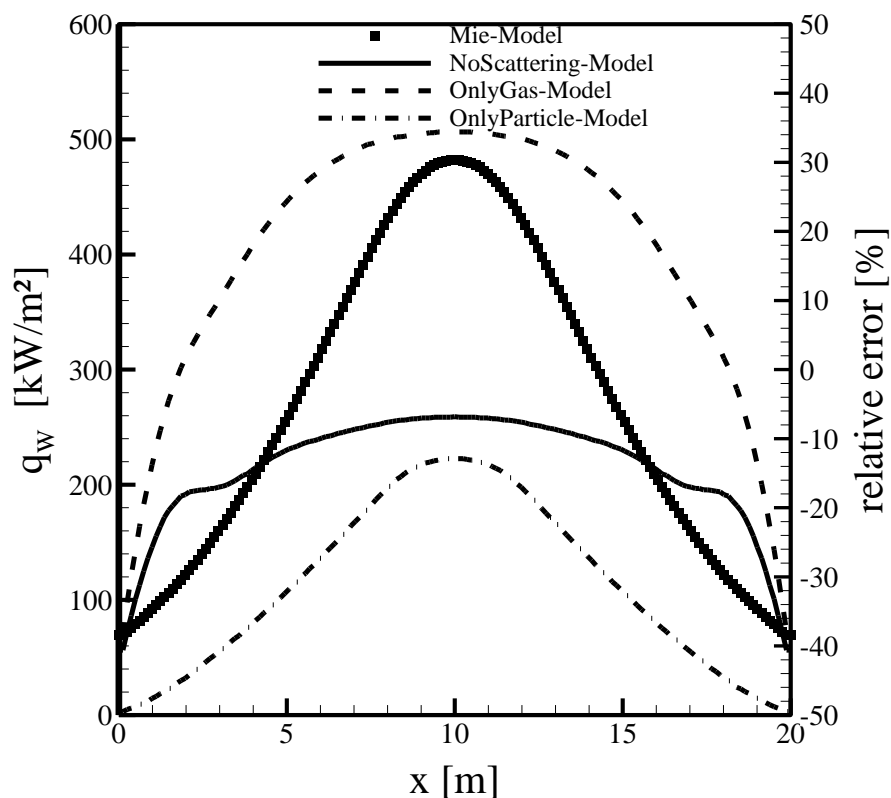


Figure 22: Distributions of the net wall heat flux in the radial direction  $y$  along the side wall at  $y = 20 \text{ m}$  for the reference “Mie-Model” and the relative errors for models without scattering, only gas radiation, and only particle radiation within the NBCK context.

### 3.3.1.2 Influence of particle radiation modelling within the NBCK context

In this subsection, the simulation results are presented for different approximations of modelling the particle radiative properties. The investigations are conducted within the NBCK context, since it provides very accurate solutions due to the detailed resolution of the spectral range.

#### Henyeey-Greenstein phase function and transport approximation

Firstly, the influence of approximating the detailed Mie phase function with the analytical Henyeey-Greenstein function, given in Equation (79), and the transport

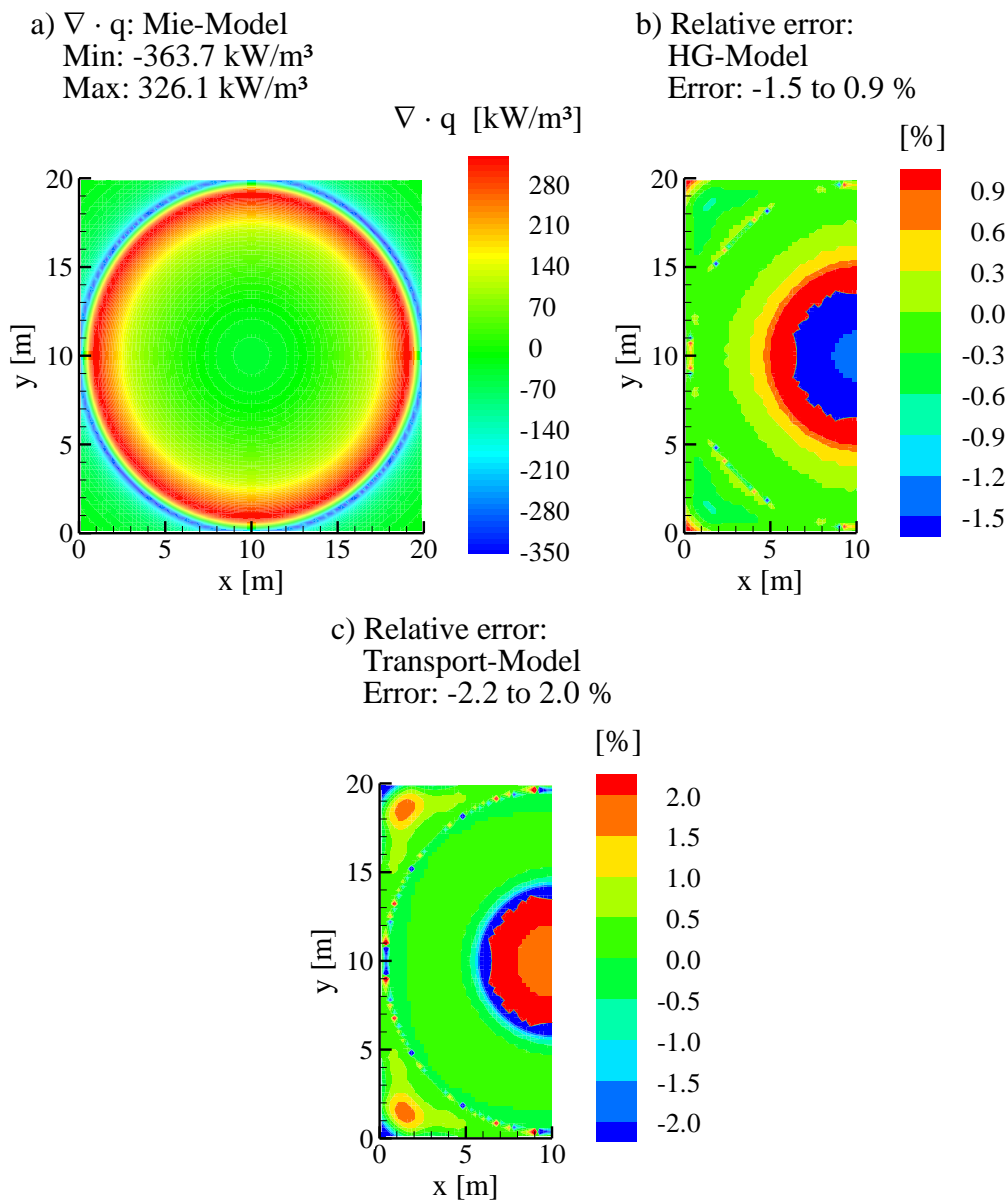


Figure 23: Distributions of the radiative source term within the enclosure predicted by the NBCK model with the Mie phase functions, (a), and the relative error of the NBCK model when the Mie phase functions are approximated by the Henyeey-Greenstein expression, (b), and the transport approximation, (c).

approximation, given in Equation (80), is examined. Nonetheless, the absorption and scattering coefficients of the particles are still obtained from Mie theory. Figure 23 shows the radiative source term predicted by the benchmark “Mie-Model” (Figure 23(a)) and the relative errors of the “HG-Model” (Figure 23(b)) and the “Transport-Model” (Figure 23(c)) within the confinement. With a mean relative error of 0.2 % and maximum deviations of less than 1.5 % the “HG-Model” predicts very accurately the radiative source terms. A similar accuracy is observed for the “Transport-Model” with maximum relative differences of less than 2.2 % and a mean relative error of 0.4 %.

Distributions of the net wall heat fluxes in  $y$ -direction along the side wall at  $y = 20\text{ m}$  and the corresponding relative error caused by using the “HG-Model” and the “Transport-Model” are illustrated in Figure 24. Using the Henyey-Greenstein phase function to approximate the Mie phase function shows again a very low level of relative errors compared to the benchmark solution. The peak value is only slightly underestimated with a relative error of about 0.1 %. A maximum deviation of about 2.1 % can be observed for the smallest values at the edges of the side wall. Otherwise, the net wall heat fluxes are reproduced with a relative error smaller than 1 % within the location range from  $x = 0.6\text{ m}$  to  $x = 19.4\text{ m}$ , resulting in a mean relative error of about only 0.2 %. Similar observations can be drawn for the “Transport-Model” results. For this approximation, the peak value is slightly overestimated with a relative error of about 0.2 %, whereas slightly higher maximum differences of 6.3 % can be seen at the edges of the side wall. Generally, the radiative heat flux is accurately reproduced with a relative deviation of less than 1 % within the location range from  $x = 1\text{ m}$  to  $x = 19\text{ m}$ , giving a mean relative error of 0.6 %.

The above results show that approximating the phase functions of the coal/char and ash particles with the appropriate spectral asymmetry factor for the Henyey-Greenstein functions and the transport approximation is sufficient to get reliable predictions with a significant saving by a factor of eight and twelve, respectively, in computational time as compared to the ‘exact’ Mie phase function. Since the simulation results obtained with the HG phase function are virtually the same as those calculated with the Mie phase functions, they will be considered as the benchmark hereafter. Correspondingly, approximate models will also be run by considering the HG phase function.

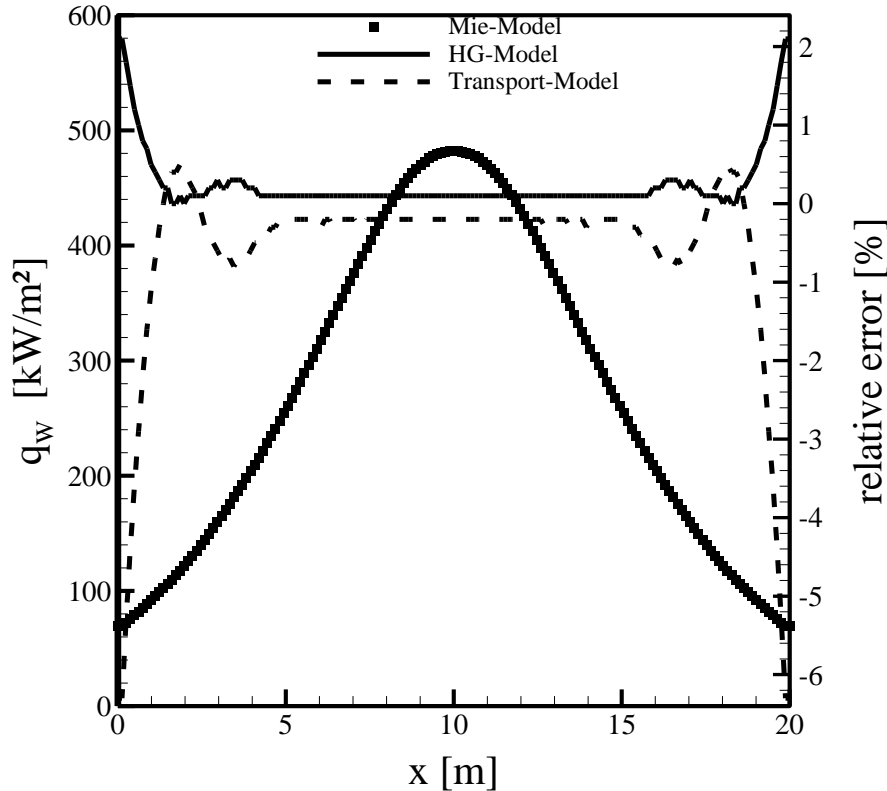


Figure 24: Distributions of the net wall heat flux in the radial direction  $y$  along the side wall at  $y = 20 \text{ m}$  calculated with the Mie phase functions as reference (Mie-Model) and the relative error due to applying the Henyey-Greenstein phase functions (HG-Model) within the NBCK context.

### Approximate modelling of radiative particle properties

In this subsection, the impact of modelling the particle radiative properties with the gray formulations given in Subsection 2.3.4 is investigated to assess their accuracy. Figure 25 and Figure 26 depict the distributions of the radiative source term within the enclosure and the net wall heat flux for the benchmark “HG-Model” and the relative errors caused by using gray particle radiative properties. Generally, it can be stated for all models that the higher relative errors of the radiative source term occur in locations with low values of the radiative source terms close to the threshold of  $|\nabla \cdot q_{\text{benchmark}}| \approx 0.1 \cdot |\nabla \cdot q_{\text{benchmark,max}}|$ , as expected.

The results of the “GrayAsymFactor-Model”, which applies gray Henyey-Greenstein phase functions obtained with Planck-mean asymmetry factors, show very good agreement with the benchmark solutions for the radiative source term. All the minima and maxima are correctly calculated with relative errors less than 1%. The maximum deviations of up to 5.5% are observed at locations where the radiative source terms are close to the threshold value, whereas the mean relative error is only about 1.0%. Similar to the radiative source terms, the net wall heat fluxes are also predicted accurately by the “GrayAsymFactor-Model”. The peak value is

slightly underestimated by about 0.8 %, whereas the values at the corners are under-predicted by about 9.7 %, yielding a mean relative difference of approximately 3.3 %.

The accuracy of the “GrayParticle-Model”, where all radiative particle properties (absorption and scattering coefficients as well as phase functions) are modeled by the according Planck-mean values, is demonstrated in Figure 25(c) and Figure 26. Higher deviations compared to the “GrayAsymFactor-Model” are observed. For the radiative source term, the global minima are underestimated by about 8.8 %, whereas the maximum values are correctly reproduced with less than 1 % relative differences. Higher deviations of up to 17.5 % are observed for regions where the radiative source terms are low and close to the threshold value. Figure 25(c) shows that the “GrayParticle-Model” predicts lower radiative source term values, especially in regions where the absorption term is higher than the emission term (negative values of the radiative source term in Figure 25(a)). This is due to the use of Planck-mean values of the absorption coefficients, which provide a good estimation of the overall emission, but not absorption in the considered domain. With a mean relative error of about 4.2 % the results of the “GrayParticle-Model” are in good overall agreement with the benchmark solution. The net wall heat fluxes are under-predicted by the “GrayParticle-Model” over the whole side wall with a relative error of 1.3 % at the maximum value at  $x = 10 \text{ m}$ , but the relative errors jump to 29.4 % at the corners (see Figure 26). The mean relative error is about 11.7 %.

The “GrayCIR-Model”, which applies spectrally constant values for the refractive indices of coal/char and ash particles, shows the highest deviation from the benchmark results with over-prediction of the maximum values of the radiative source term by about 7.6 %, whereas it under-predicts the minimum values by -6.1 %. Also, the maximum deviations and the mean relative error of 48.7 % and 7.5 % are the highest among the investigated particle radiative models. This observation is in accordance to the findings of Johansson et al. [58], who stated that the application of different refractive indices for ash particles results in higher differences of the radiative source term. Thus, further simulations were carried out using a constant refractive index either for the coal/char or ash particles. The simulation results, not shown here, identify that the higher deviations are caused by using a constant refractive index for the ash particles. It was observed that the results obtained with a constant refractive index for the ash particles and a spectrally varying one for the coal/char particles are almost identical to the one shown in Figure 25(d) of the “GrayCIR-Model”, whereas the simulation results with a constant refractive index for the coal/char particles and a spectrally varying one for the ash particles are almost indistinguishable from the benchmark solution. Thus, using a constant

refractive index for the ash particles is in contrast to the experimental observations given in [109]–[111] that show a strong spectral variation of this quantity. In consequence, use of this assumption leads to higher deviations from the benchmark solution of the radiative source term. Another important reason for the larger errors associated with the assumption of constant refractive index for fly-ash particles is that in this test case the cross-sectional area per unit volume of the ash particles is much higher than the one for coal particles. Therefore, changes in the radiative properties of the ash particles strongly influence the radiation field.

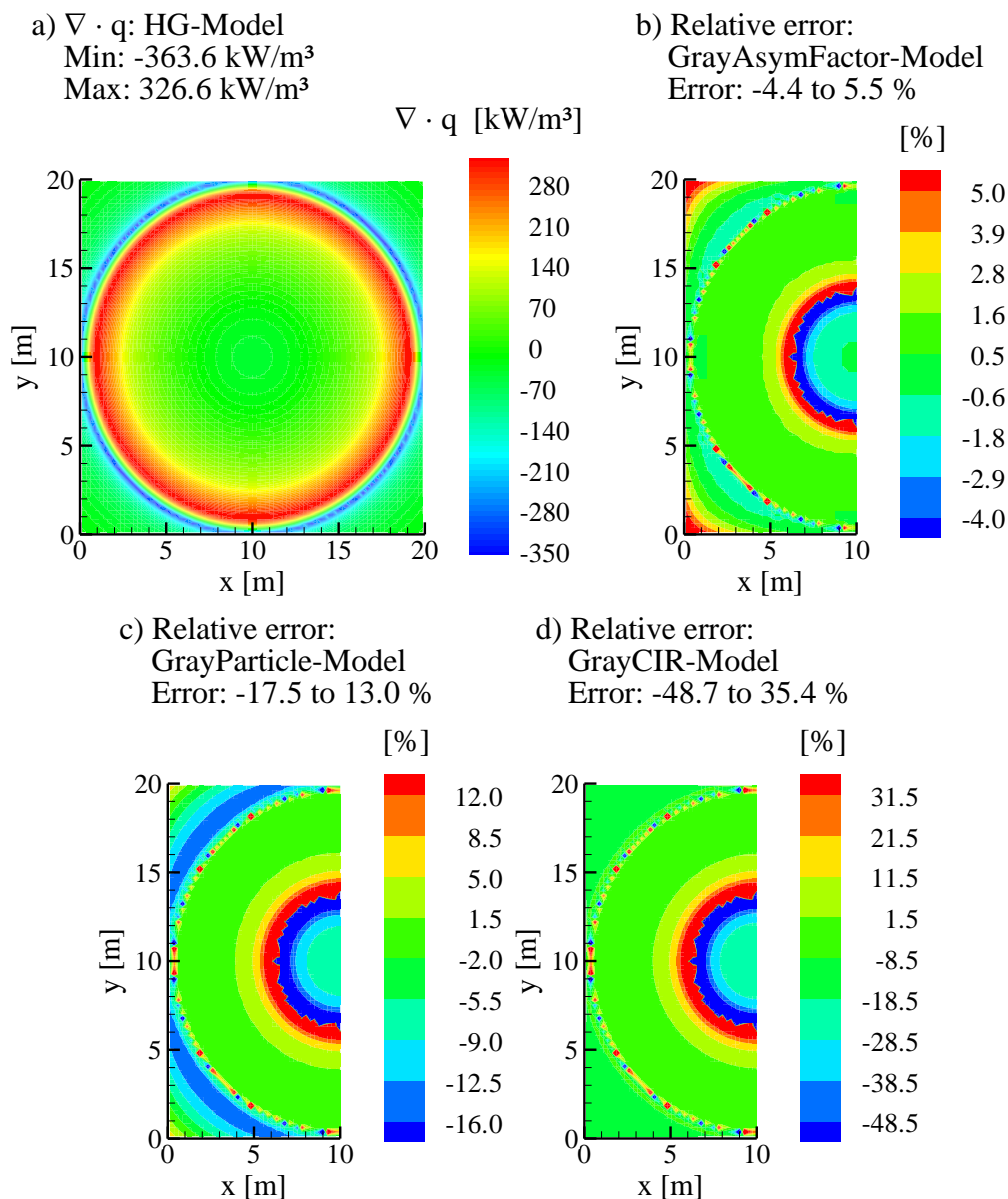


Figure 25: Distributions of the radiative source term within the confinement from the NBCK model with the Henyey-Greenstein phase functions, (a), the relative error caused by using gray asymmetry factors, (b), gray particle properties, (c), and gray refractive indices of all particles, (d).

In contrast to the findings for the radiative source term, the results of the “GrayCIR-Model” are more accurate for the net wall heat flux in comparison to the ones of the “GrayParticle-Model” (see Figure 26). The maximum value at  $x = 10\text{ m}$  is over-predicted by about 1.8 %, while on the contrary relative errors of approximately 9.8 % are observed for the minimum values at the corners of the side wall. Nevertheless, it provides a similar mean relative error of about 3.9 % compared to the “GrayAsymFactor-Model”.

For this test case, it can be stated that approximating the phase functions of the coal/char and ash particles with gray Henyey-Greenstein functions obtained with Planck-mean values of the corresponding asymmetry factors, but applying non-gray absorption and scattering coefficients, is a very good compromise between accuracy and efficiency in modelling radiative heat transfer by coal/char and ash particles. Thus, it is attractive to apply this approximation within the context of the WBCK, FSCK and WSGG models, which will be discussed in the following subsection.

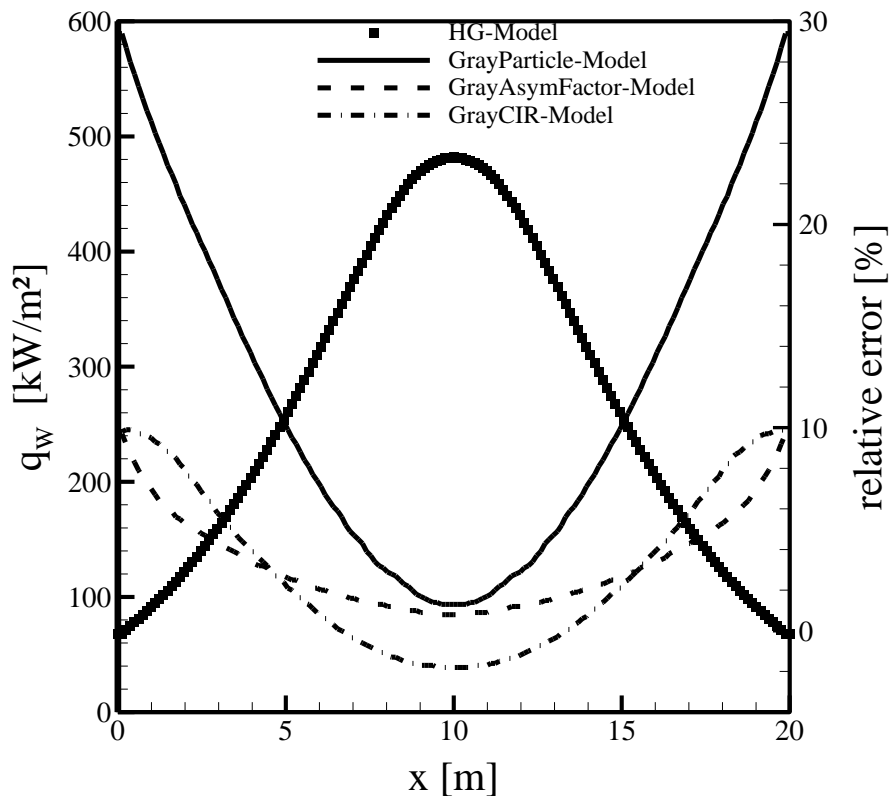


Figure 26: Distributions of the net wall heat flux in radial direction  $y$  along the side wall at  $y = 20\text{ m}$  calculated with the reference “HG-Model” and the relative errors for three gray particle radiative properties within the NBCK context.

### 3.3.1.3 Influence of gas radiation modelling

The influence of spectral resolution of modelling gas radiation on the simulation results is investigated in this subsection. For this evaluation, the radiative source term and net wall heat flux distributions simulated with the WBCK, based on the HITEMP 2010 spectroscopic database as presented in Subsection 2.2.3, FSCK and WSGG models, the latter one based on the parameters of Bordbar et al. [53], are illustrated in Figure 27 and Figure 28, respectively. It is noted here that the WBCK, FSCK and WSGG models all apply gray Henyey-Greenstein phase functions. The distributions of the radiative source term within the enclosure are given in Figure 27, with the simulation results of “NBCK\_HG-Model” as the reference solution in Figure 27(a). Figure 27(b) shows that the relative errors of the radiative source term predicted by the “WBCK-Model” are fairly low, suggesting that the results of this approximate model are in good agreement with the benchmark solution. The relative errors at the minimum and maximum values are less than 1.1 % and the mean relative deviation is only about 0.8 % for the whole confinement. The maximum deviations of about 5.8 % are observed only at locations where the values of the radiative source term are very low and close to the threshold value. The predicted net wall heat fluxes by the “WBCK-Model” are also almost indistinguishable from those by the “NBCK\_GrayAsymFactor-Model”, see Figure 25(b). The peak value and the minimum values near the corners are under-predicted by about 0.7 % and 9.1 %, respectively, resulting in a mean difference of about 2.8 %.

Computing the radiative source term distribution with the global FSCK model applying also the Planck-mean values for the scattering coefficients, denoted as “FSCK-Model”, shows a good overall agreement of the simulation results with the benchmark solution. The minimum values are slightly over-predicted by about 3.9% and the maximum values are underestimated by about 3.9 %, while the mean relative error is about 4.6 %. Only at locations, where the absolute values are close to the threshold value, the deviations are higher with values up to about 25.7 %. This level of accuracy is comparable to that of the NBCK model using gray particle properties, denoted as “GrayParticle-Model”, shown in Figure 25(c). However, the “FSCK-Model” is much more computationally efficient, since the RTE is solved only for 10 gas-particle absorption coefficients, compared to 3150 in the NBCK model and 119 in the WBCK model. With regard to the performance in the former 3D geometries, the slightly higher deviation from the NBCK model results is likely due to the use of gray scattering coefficients for the particles than the modelling of the gas radiation. The net wall heat fluxes predicted with the “FSCK-Model” are also in reasonable agreement with the benchmark solution with relative deviations

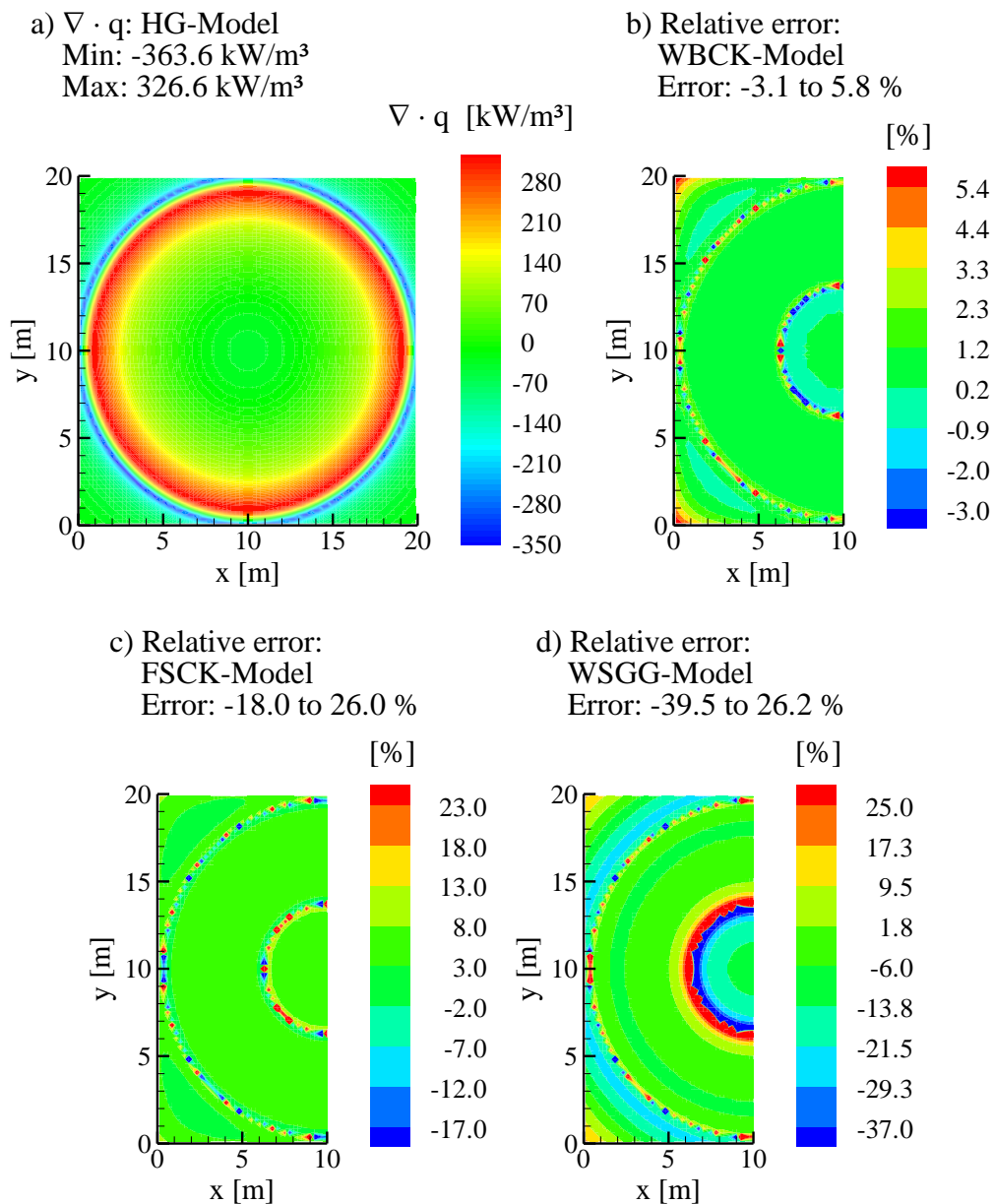


Figure 27 Distributions of the radiative source term within the confinement predicted by the NBCK model, (a), and the relative errors of the WBCK model, (b), the FSCK model, (c), and WSGG model, (d).

of 3.1 % for the peak and 11.5 % for the minima near the edges, leading to a mean relative error of about 4.9 %.

Regarding the simulation results of the radiative source term distribution computed with the WSGG model given in Figure 27(d), which considers the particle radiative properties as gray, a further loss of overall accuracy, especially with respect to the minimum values, can be observed. The maximum values are only slightly over-predicted by 1.4 %, whereas the minimum values are underestimated by about 16.6 %. This leads to a mean relative error of about 8.9 %. The maximum deviation of up to 39.5 % is encountered at locations, where the values are close to the threshold value and a change from absorption to emission is present.

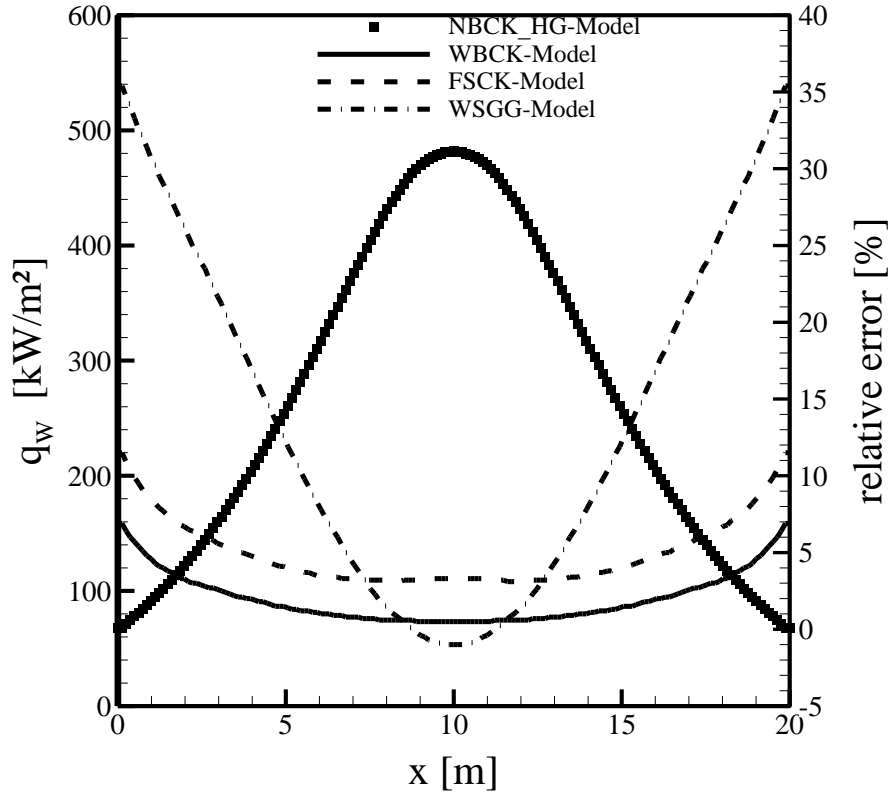


Figure 28: Distributions of the net wall heat flux in radial direction  $y$  along the side wall at  $y = 20 \text{ m}$  for the reference “NBCK\_HG-Model” and the relative errors of “NBCK\_GrayAsym-Factor-Model”, “WBCK-Model”, and “FSCK-Model”.

The net wall heat fluxes calculated with the WSGG model presented in Figure 28 show a close agreement with the benchmark data for the maximum value with a relative error of about 1 %. In contrast to the WBCK and FSCK results, a steeper decrease of the net wall heat flux is predicted towards the corners resulting in maximum differences of up to 35.4 % and a mean relative error of ca. 13.8 %. This resembles the same trend as observed for the NBCK “GrayParticle-Model” given in Figure 26 and is likely caused by considering particle absorption as gray.

### 3.3.2 Conclusions

In this subsection the influence of different contributions to the total radiation, the modelling of particle as well as gas radiative properties were investigated. The following conclusions could be drawn:

Although radiation heat transfer is dominated by the particles under the representative conditions of this investigation, gas radiation has to be modeled accurately, since it can contribute up to 50 % of the radiative source term and, thus, it is still important to adequately take into account the non-gray properties of  $\text{CO}_2$  and  $\text{H}_2\text{O}$ .

The Henyey-Greenstein phase function is a good approximation of the ‘exact’ Mie phase functions for coal and ash particles. Thus, it can be used as an accurate and efficient procedure to model the phase functions for coal/char and ash particles rather than computing the more complex and computationally expensive Mie phase functions. Additionally, the transport approximation offers an efficient and accurate modelling approach for particulate matter with strong forward scattering characteristics.

In accordance with the findings of Johansson et al. [58], it was observed that the choice of the complex refractive index for ash particles has a stronger impact on the simulation results than that for the coal particles. Using a gray complex refractive index for coal has no influence on prediction, whereas use of such approximation for ash particles introduces significant discrepancies.

The Planck-mean particle radiative properties were found to provide predictions on the whole within 20 % of the reference solutions.

Approximating the scattering phase functions as gray Henyey-Greenstein ones, obtained with the corresponding Planck-mean values of the asymmetry factors for the coal/char and ash particles, was found to be a reliable assumption.

The WBCK model in connection with non-gray particle absorption and scattering efficiencies and gray Henyey-Greenstein phase functions was found to provide predictions in close agreement with the benchmark, but with significantly less computational effort. Thus, a careful choice of the wide-bands, for which the blackbody intensity and the radiative properties of the particles are assumed constant, is a reasonable and efficient approach to compute the radiative source terms with nearly the same accuracy as the NBCK model with gray phase functions.

The FSCK scheme proposed by Modest and Riazzi [37], based on gray scattering coefficients and gray phase functions, is appropriate to model the radiative heat transfer including gas and particle radiation in CFD-simulations for engineering applications and offers additional reduction in computational expense with similar accuracy as the WBCK model.

The WSGG model with the parameters of Bordbar et al. [53] and gray particle radiative properties shows good agreement to the benchmark results, especially for regions, where emission is pre-dominant. The assumption of gray particle absorption coefficients likely causes the higher deviations in comparison to the WBCK and FSCK models.

## 4 Conclusions and perspectives

The aim of this thesis was to provide a recommendation for a thermal radiation model to be used in commercial CFD software packages to predict the radiative source terms and wall heat fluxes for different oxy-fuel combustion conditions. The model was chosen with regard to the highest accuracy at reasonable computational expenses. For this purpose, three different virtual combustors were considered to investigate the influences of the encountered pressure path lengths, inhomogeneously distributed amounts of radiating gases, presence of particles and their radiative modelling as well as inhomogeneous temperature distributions on the accuracy of the various radiation models. The following conclusions could be drawn:

The application of the correlated-k approach within the narrow-band context with the updated narrow-band parameters of Rivière and Soufiani [81] offers the possibility to provide benchmark results for applications where neither very accurate line-by-line results nor experimental data are available. The simulation results are as accurate as computed with statistical narrow-band models compared to line-by-line benchmark data and close to the benchmark data itself, which is in accordance to the findings of Chu et al. [20], Consalvi and Liu [137] or Chu et al. [19], but with less computational expense, since no ray-tracing technique has to be applied. In contrast to the work of Johansson [67], the additional inclusion of scattering of particulate matter is easily realized by maintaining the accuracy for modelling the gas absorption, since absorption based solution algorithms can be applied rather than translating gas transmissivities into according gas absorption coefficients, which could introduce a loss of accuracy considering the impact of gas radiation on the total radiation. Within the narrow-band context, it was found that approximating the scattering phase function with simpler analytical functions like the Henyey-Greenstein phase function or the use of the transport approximation leads to the same accuracy as applying tedious Mie computations with respect to spectrally integrated radiative properties like the radiative source terms and net wall heat fluxes. Similar conclusions could be drawn by the work of Gronarz et al. [70] when comparing the simulation results computed with the delta-Eddington approximation and the benchmark results obtained with Mie phase functions. Furthermore, retrieving spectrally

varying particle properties with a gray complex index of refraction for ash particles yielded to higher deviations from the benchmark results than applying a gray complex index of refraction for coal particles, which is in accordance with the findings of Johansson et al. [58]. Additionally, it was found that applying gray Henyey-Greenstein phase functions computed with Planck-mean asymmetry factors had only minor influences on the accuracy of predicting the radiative source terms and net heat fluxes. Thus, the use of gray scattering properties for spectrally coarser models as wide-band and global models was justified for the considered coal/char and ash particles. However, considering all particle radiative properties to be gray led to higher deviations from the benchmark results.

Additionally, wide-band models based on two different spectral databases, EWBM and HITEMP 2010, were considered. For the wide-band models based on EWBM, the findings of Ströhle [28] could be confirmed that the computationally much less expensive multiple gases formulation was as accurate as the spectral formulation, whereas use of the gray gases formulation resulted in more deviation from the benchmark results, since the latter one is only suited for homogeneously distributed gas mole fractions. Furthermore, it was found that for oxy-fuel conditions with lower pressure path lengths, non-isothermal temperature and inhomogeneous gas concentrations profiles, as well as for homogeneous gas concentrations profiles as given by e.g. by Porter et al. [41], good agreement of the simulation results for the WBCK\_SPF and WBCK\_MGF was reached compared to the benchmark results considering only gas radiation. However, for oxy-fuel combustion cases with higher pressure path lengths, higher loss in accuracy of up to 29 % maximum mean error was found. As a consequence, the WBCK model based on the EWBM spectral database with its actual parameters should be avoided to compute radiative heat transfer in a real-sized oxy-fuel combustor. Here, the computation of the total gas transmissivity for the optimization procedure for the MGF formulation from newer databases as e.g. given by Rivière and Soufiani [81] and updating the correlations originally derived for air-combustion to oxy-fuel scenarios could lead to an improved accuracy of the model. This is supported by the simulation results computed with the WBCK model based on the HITEMP 2010 spectral database for the gas-particle test case with wet oxy-fuel combustion conditions, which were in remarkable accordance with the benchmark solutions. This conclusion is consistent with the findings of Chu et al. [19], who observed a similar agreement of the simulation results with this updated WBCK model compared to the ones obtained with the NBCK model considering only gas radiation.

The full-spectrum correlated-k model consistently predicted the radiative source terms and net wall heat fluxes with the highest accuracy and reasonable computational effort among

the considered global radiation models in this thesis. Regardless of the encountered pressure path lengths and inhomogeneity of the gas mole as well as temperature distributions, the mean relative errors were below 3 % for the test cases considering only gas radiation and less than 5 % with additional particle radiation. These findings are in accordance with numerous other works, e.g. of Porter et al. [41] who investigated homogenous gas mole distributions in oxy-fuel combustion scenarios, Chu et al. [19] who considered various total operating pressures for oxy-fuel combustion conditions, or Yang et al. [138] who inquired the influences of radiative modelling on the CFD simulation results of small and large scale oxy-coal furnaces. Additionally, it was found that the assumption of gray scattering as proposed by Modest and Riazzi [37] was reliable for the considered gas-particle test case.

Furthermore, various parameter sets derived for air and oxy-fuel conditions were applied in this thesis to analyze their influences on the accuracy of the weighted-sum-of-gray-gases model. It was revealed that the range of pressure path length products used to obtain and validate the WSGG parameter sets should be wide enough to cover those encountered in real-sized combustors. Here, the parameters of Kangwanpongpan et al. [51] and Bordbar et al. [53], both derived from the HITEMP 2010 spectral database, were found to be most reliable for real-sized oxy-coal furnaces. The WSGG models with the parameters of Johansson et al. [49], based on the older SNB database of Soufiani and Taine [97], and Yin et al. [48], the latter one based on the EWBM spectral database, showed higher mean deviations for the same test cases. In contrast, for conditions with homogeneous gas concentrations, non-isothermal temperature profiles and smaller pressure path lengths as introduced by Porter et al. [41], the results for the radiative source terms and wall heat fluxes obtained with the parameters of Bordbar et al. and Johansson et al. showed good agreement with the benchmark solution, whereas the use of the parameters of Kangwanpongpan et al. led to higher mean deviations, see [139]. For conditions with inhomogeneous gas concentrations and non-isothermal temperature profiles as well as shorter pressure path lengths, as considered in this thesis, these three parameter sets all showed similar accuracy with mean deviations up to 17 %. However, the simulation results obtained with the parameters of Yin et al. showed constantly good accuracy for oxy-fuel conditions at lower pressure path lengths regardless of the gas mole distributions being homogeneous or inhomogeneous, as given in [139]. These findings confirm that the long path lengths encountered in real combustion furnaces and the underlying database strongly influence the accuracy of the used WSGG parameter set. Therefore, it is important to consider longer path lengths relevant to real-sized boilers and to provide the corresponding benchmarks in evaluation of the performance of different gas radiation models to recommend the

appropriate WSGG parameter sets for CFD simulations. Furthermore, it was found that the use of Planck-mean gray radiative properties in conjunction with the WSGG parameters of Bordbar et al. leads to higher deviations from the benchmark results than considering only particle scattering as gray with the FSCK model. This finding confirms the conclusion of Hofgren and Sundén [72] that considering particle radiation solely as gray with the according Planck-mean values should be avoided and at least non-gray particle absorption should be taken into account.

In summary, one of the main conclusions of this work is that the FSCK methods are the next generation of radiative property models to be used in CFD simulations of real combustion applications due to its consistently high accuracy and reasonable computational expense for all considered oxy-fuel combustion scenarios and, thus, are more general than WSGG models.

A further reduction of the computational effort of the FSCK model could be obtained by the use of pre-generated databases in the form of look-up tables. These look-up tables should include various particle radiative properties such as coal/char, ash and soot with different diameters and material composition to be applicable for a broad range of real engineering applications. Furthermore, these databases could be enlarged to Sulphur dioxide if investigations show a high impact for high-sulfur coals. In this thesis, the accuracy of the considered radiation models was assessed with regard to benchmark solutions computed by narrow-band models, which were formerly evaluated against accurate line-by-line results. The reason for this procedure was the lack of literature data regarding experimentally measured radiative properties like radiative source terms, wall heat fluxes or radiative intensities in oxy-fuel combustion conditions of real-sized furnaces. As future work, it would be desirable to measure the aforementioned quantities in a real-sized furnace to validate the considered radiation models and the reliability of LBL calculations. This could be achieved e.g. within the framework of the Collaborative Research Center SFB/Transregio 129 “Oxyflame”. Additionally, the knowledge gap of accurately measured data of particle radiative properties with different coal and ash compositions as well as size distributions should be closed. Here, it is also interesting to know if the use of Mie-theory is sufficient to approximate the radiative properties of aspherical and inhomogeneous particles. The application of the “transport approximation” should be further investigated, since it provides a strong reduction in computational effort, but no commitment in accuracy loss for the prediction of integrated radiative properties as e.g. the radiative source term or heat flux. If the weighted-sum-of-gray-gases model is the favorite radiation model of choice due to its simple implementation in commercially available CFD software packages, then parameters for combined non-gray gas and particle radiation should be

derived, which account for different burnout states, diameters, concentrations and types of material of the considered particles.

# Bibliography

- [1] IEA (2019), “World Energy Outlook 2019,” 2019. [Online]. Available: <https://www.iea.org/reports/world-energy-outlook-2019>.
- [2] A. F. Ghoniem, “Needs, resources and climate change: clean and efficient conversion technologies,” *Progress in Energy and Combustion Science*, vol. 37, pp. 15–51, 2011.
- [3] Z. H. Liang, W. Rongwong, H. Liu, K. Fu, H. Gao, F. Cao, R. Zhang, T. Sema, A. Henni, K. Sumon, and others, “Recent progress and new developments in post-combustion carbon-capture technology with amine based solvents,” *International Journal of Greenhouse Gas Control*, vol. 40, pp. 26–54, 2015.
- [4] D. P. Hanak, S. Michalski, and V. Manovic, “From post-combustion carbon capture to sorption-enhanced hydrogen production: A state-of-the-art review of carbonate looping process feasibility,” *Energy Conversion and Management*, vol. 177, pp. 428–452, 2018.
- [5] V. Gargiulo, M. Alfè, F. Raganati, A. Zhumagaliyeva, Y. Doszhanov, P. Ammendola, and R. Chirone, “CO<sub>2</sub> adsorption under dynamic conditions: An overview on rice husk-derived sorbents and other materials,” *Combustion Science and Technology*, vol. 191, pp. 1484–1498, 2019.
- [6] L. Giordano, D. Roizard, and E. Favre, “Life cycle assessment of post-combustion CO<sub>2</sub> capture: A comparison between membrane separation and chemical absorption processes,” *International Journal of Greenhouse Gas Control*, vol. 68, pp. 146–163, 2018.
- [7] W. L. Theo, J. S. Lim, H. Hashim, A. A. Mustafa, and W. S. Ho, “Review of pre-combustion capture and ionic liquid in carbon capture and storage,” *Applied Energy*, vol. 183, pp. 1633–1663, 2016.
- [8] G. Scheffknecht, L. Al-Makhadmeh, U. Schnell, and J. Maier, “Oxy-fuel coal combustion—A review of the current state-of-the-art,” *International Journal of Greenhouse Gas Control*, vol. 5, pp. S16–S35, 2011.
- [9] L. Chen, S. Z. Yong, and A. F. Ghoniem, “Oxy-fuel combustion of pulverized coal: Characterization, fundamentals, stabilization and CFD modeling,” *Progress in Energy and Combustion Science*, vol. 38, pp. 156–214, 2012.
- [10] R. Stanger, T. Wall, R. Spörl, M. Paneru, S. Grathwohl, M. Weidmann, G. Scheffknecht, D. McDonald, K. Myöhänen, J. Ritvanen, and others, “Oxyfuel combustion for CO<sub>2</sub> capture in power plants,” *International Journal of Greenhouse Gas Control*, vol. 40, pp. 55–125, 2015.
- [11] J. Adánez, A. Abad, T. Mendiara, P. Gayán, L. De Diego, and F. García-Labiano, “Chemical looping combustion of solid fuels,” *Progress in Energy and Combustion Science*,

- vol. 65, pp. 6–66, 2018.
- [12] M. B. Toftegaard, J. Brix, P. A. Jensen, P. Glarborg, and A. D. Jensen, “Oxy-fuel combustion of solid fuels,” *Progress in Energy and Combustion Science*, vol. 36, pp. 581–625, 2010.
- [13] L. Strömberg, G. Lindgren, J. Jacoby, R. Giering, M. Anheden, U. Burchhardt, H. Altmann, F. Kluger, and G.-N. Stamatelopoulos, “Update on Vattenfall’s 30 MWth oxyfuel pilot plant in Schwarze Pumpe,” *Energy Procedia*, vol. 1, pp. 581–589, 2009.
- [14] E. Portillo, B. Alonso-Fariñas, F. Vega, M. Cano, and B. Navarrete, “Alternatives for oxygen-selective membrane systems and their integration into the oxy-fuel combustion process: A review,” *Separation and Purification Technology*, vol. 229, p. 115708, 2019.
- [15] P. Wienchol, A. Szlęk, and M. Ditaranto, “Waste-to-energy technology integrated with carbon capture—Challenges and opportunities,” *Energy*, vol. 198, p. 117352, 2020.
- [16] H. Chu, F. Liu, and H. Zhou, “Calculations of gas thermal radiation transfer in one-dimensional planar enclosure using LBL and SNB models,” *International Journal of Heat and Mass Transfer*, vol. 54, pp. 4736–4745, 2011.
- [17] H. Chu, M. Gu, H. Zhou, and F. Liu, “Calculations of narrow-band transmissivities and the Planck mean absorption coefficients of real gases using line-by-line and statistical narrow-band models,” *Frontiers in Energy*, vol. 8, pp. 41–48, 2014.
- [18] H. Chu, M. Gu, J.-L. Consalvi, F. Liu, and H. Zhou, “Effects of total pressure on non-grey gas radiation transfer in oxy-fuel combustion using the LBL, SNB, SNBCK, WSGG, and FSK methods,” *Journal of Quantitative Spectroscopy and Radiative Transfer*, vol. 172, pp. 24–35, 2016.
- [19] H. Chu, J.-L. Consalvi, M. Gu, and F. Liu, “Calculations of radiative heat transfer in an axisymmetric jet diffusion flame at elevated pressures using different gas radiation models,” *Journal of Quantitative Spectroscopy and Radiative Transfer*, vol. 197, pp. 12–25, 2017.
- [20] H. Chu, F. Liu, and H. Zhou, “Calculations of gas radiation heat transfer in a two-dimensional rectangular enclosure using the line-by-line approach and the statistical narrow-band correlated-k model,” *International Journal of Thermal Sciences*, vol. 59, pp. 66–74, 2012.
- [21] J. Taine and A. Soufiani, “Gas IR radiative properties: from spectroscopic data to approximate models,” in *Advances in Heat Transfer*, vol. 33, Elsevier, 1999, pp. 295–414.
- [22] A. A. Lacis and V. Oinas, “A description of the correlated k distribution method for modeling nongray gaseous absorption, thermal emission, and multiple scattering in vertically inhomogeneous atmospheres,” *Journal of Geophysical Research: Atmospheres*, vol. 96, pp. 9027–9063, 1991.
- [23] J. Taine, “A line-by-line calculation of low-resolution radiative properties of CO<sub>2</sub>-CO-transparent nonisothermal gases mixtures up to 3000 K,” *Journal of Quantitative*

- Spectroscopy and Radiative Transfer*, vol. 30, pp. 371–379, 1983.
- [24] F. Liu, “Numerical solutions of three-dimensional non-grey gas radiative transfer using the statistical narrow-band model,” *ASME Journal of Heat Transfer*, vol. 121, pp. 200–203, 1999.
- [25] D. Edwards, “Molecular gas band radiation,” in *Advances in Heat Transfer*, vol. 12, Elsevier, 1976, pp. 115–193.
- [26] P. Y. C. Lee, K. Hollands, and G. Raithby, “Reordering the absorption coefficient within the wide band for predicting gaseous radiant exchange,” *ASME Journal of Heat Transfer*, vol. 118, pp. 394–400, 1996.
- [27] G. Parthasarathy, J. C. Chai, and S. V. Patankar, “A simple approach to non-gray gas modeling,” *Numerical Heat Transfer*, vol. 29, pp. 113–123, 1996.
- [28] J. Ströhle, “Wide band correlated-k approaches for non-grey radiation modelling in oxy-fuel combustion with dry recycling,” *Fuel*, vol. 90, pp. 3007–3013, 2011.
- [29] D. Edwards and W. Menard, “Comparison of models for correlation of total band absorption,” *Applied Optics*, vol. 3, pp. 621–625, 1964.
- [30] M. F. Modest, “The weighted-sum-of-gray-gases model for arbitrary solution methods in radiative transfer,” *ASME Journal of Heat Transfer*, vol. 113, pp. 650–656, 1991.
- [31] M. K. Denison and B. W. Webb, “A spectral line-based weighted-sum-of-gray-gases model for arbitrary RTE solvers,” *ASME Journal of Heat Transfer*, vol. 115, pp. 1004–1012, 1993.
- [32] V. P. Solovjov and B. W. Webb, “SLW modeling of radiative transfer in multicomponent gas mixtures,” *Journal of Quantitative Spectroscopy and Radiative Transfer*, vol. 65, pp. 655–672, 2000.
- [33] V. P. Solovjov, D. Lemonnier, and B. W. Webb, “The SLW-1 model for efficient prediction of radiative transfer in high temperature gases,” *Journal of Quantitative Spectroscopy and Radiative Transfer*, vol. 112, pp. 1205–1212, 2011.
- [34] J. T. Pearson, “The Development of Updated and Improved SLW Model Parameters and Its Application to Comprehensive Combustion Predictions,” 2013.
- [35] M. F. Modest and H. Zhang, “The full-spectrum correlated-k distribution for thermal radiation from molecular gas-particulate mixtures,” *ASME Journal of Heat Transfer*, vol. 124, pp. 30–38, 2002.
- [36] H. Zhang and M. F. Modest, “A multi-scale full-spectrum correlated-k distribution for radiative heat transfer in inhomogeneous gas mixtures,” *Journal of Quantitative Spectroscopy and Radiative Transfer*, vol. 73, pp. 349–360, 2002.
- [37] M. F. Modest and R. J. Riazzi, “Assembly of full-spectrum k-distributions from a narrow-band database; effects of mixing gases, gases and nongray absorbing particles, and mixtures with nongray scatterers in nongray enclosures,” *Journal of Quantitative*

- Spectroscopy and Radiative Transfer*, vol. 90, pp. 169–189, 2005.
- [38] V. P. Solovjov and B. W. Webb, “A local-spectrum correlated model for radiative transfer in non-uniform gas media,” *Journal of Quantitative Spectroscopy and Radiative Transfer*, vol. 73, pp. 361–373, 2002.
- [39] V. P. Solovjov and B. W. Webb, “The cumulative wavenumber method for modeling radiative transfer in gas mixtures with soot,” *Journal of Quantitative Spectroscopy and Radiative Transfer*, pp. 273–287, 2005.
- [40] F. André, “The  $\ell$ -distribution method for modeling non-gray absorption in uniform and non-uniform gaseous media,” *Journal of Quantitative Spectroscopy and Radiative Transfer*, vol. 179, pp. 19–32, 2016.
- [41] R. Porter, F. Liu, M. Pourkashanian, A. Williams, and D. Smith, “Evaluation of solution methods for radiative heat transfer in gaseous oxy-fuel combustion environments,” *Journal of Quantitative Spectroscopy and Radiative Transfer*, vol. 111, pp. 2084–2094, 2010.
- [42] A. G. Clements, R. Porter, A. Pranzitelli, and M. Pourkashanian, “Evaluation of FSK models for radiative heat transfer under oxyfuel conditions,” *Journal of Quantitative Spectroscopy and Radiative Transfer*, vol. 151, pp. 67–75, 2015.
- [43] V. Kez, J. Consalvi, F. Liu, J. Ströhle, and B. Epple, “Assessment of several gas radiation models for radiative heat transfer calculations in a three-dimensional oxy-fuel furnace under coal-fired conditions,” *International Journal of Thermal Sciences*, vol. 120, pp. 289–302, 2017.
- [44] A. G. Clements, S. Black, J. Szuhánszki, K. Stęchły, A. Pranzitelli, W. Nimmo, and M. Pourkashanian, “LES and RANS of Air and Oxy-coal Combustion in a pilot-scale Facility: Predictions of Radiative Heat Transfer,” *Fuel*, vol. 151, pp. 146–155, 2015.
- [45] V. Kez, F. Liu, J. Consalvi, J. Ströhle, and B. Epple, “A comprehensive evaluation of different radiation models in a gas turbine combustor under conditions of oxy-fuel combustion with dry recycle,” *Journal of Quantitative Spectroscopy and Radiative Transfer*, vol. 172, pp. 121–133, 2016.
- [46] R. Johansson, K. Andersson, B. Leckner, and H. Thunman, “Models for gaseous radiative heat transfer applied to oxy-fuel conditions in boilers,” *International Journal of Heat and Mass Transfer*, vol. 53, pp. 220–230, 2010.
- [47] G. Krishnamoorthy, “A new weighted-sum-of-gray-gases model for CO<sub>2</sub>-H<sub>2</sub>O gas mixtures,” *International Communications in Heat and Mass Transfer*, vol. 37, pp. 1182–1186, 2010.
- [48] C. Yin, L. C. Johansen, L. A. Rosendahl, and S. K. Kær, “New weighted sum of gray gases model applicable to computational fluid dynamics (CFD) modeling of oxy-fuel combustion: derivation, validation, and implementation,” *Energy & Fuels*, vol. 24, pp. 6275–6282, 2010.

- [49] R. Johansson, B. Leckner, K. Andersson, and F. Johnsson, "Account for Variations in the H<sub>2</sub>O to CO<sub>2</sub> Molar Ratio when Modelling Gaseous Radiative Heat Transfer with the Weighted-Sum-of-Grey-Gases Model," *Combustion and Flame*, vol. 158, pp. 893–901, 2011.
- [50] S. Rehfeldt, C. Kuhr, M. Ehmman, and C. Bergins, "Modeling of radiative properties of an oxyfuel atmosphere with a weighted sum of gray gases for variable carbon dioxide and water vapor concentrations," *Energy Procedia*, vol. 4, pp. 980–987, 2011.
- [51] T. Kangwanpongpan, F. H. França, R. C. da Silva, P. S. Schneider, and H. J. Krautz, "New Correlations for the Weighted-Sum-of-Gray-Gases Model in Oxy-fuel Conditions based on HITEMP 2010 Database," *International Journal of Heat and Mass Transfer*, vol. 55, pp. 7419–7433, 2012.
- [52] G. Krishnamoorthy, "A new weighted-sum-of-gray-gases model for oxy-combustion scenarios," *International Journal of Energy Research*, vol. 37, pp. 1752–1763, 2013.
- [53] M. H. Bordbar, G. Węcel, and T. Hyppänen, "A Line by Line based Weighted Sum of Gray Gases Model for Inhomogeneous CO<sub>2</sub>-H<sub>2</sub>O Mixture in Oxy-fired Combustion," *Combustion and Flame*, vol. 161, pp. 2435–2445, 2014.
- [54] C. Yin, L. A. Rosendahl, and S. K. Kær, "Chemistry and radiation in oxy-fuel combustion: a computational fluid dynamics modeling study," *Fuel*, vol. 90, pp. 2519–2529, 2011.
- [55] C. Yin, "Nongray-gas effects in modeling of large-scale oxy-fuel combustion processes," *Energy & Fuels*, vol. 26, pp. 3349–3356, 2012.
- [56] J. Guo, Z. Liu, P. Wang, X. Huang, J. Li, P. Xu, and C. Zheng, "Numerical investigation on oxy-combustion characteristics of a 200 MWe tangentially fired boiler," *Fuel*, vol. 140, pp. 660–668, 2015.
- [57] A. A. Bhuiyan and J. Naser, "Numerical modelling of oxy fuel combustion, the effect of radiative and convective heat transfer and burnout," *Fuel*, vol. 139, pp. 268–284, 2015.
- [58] R. Johansson, T. Gronarz, and R. Kneer, "Influence of Index of Refraction and Particle Size Distribution on Radiative Heat Transfer in a Pulverized Coal Combustion Furnace," *ASME Journal of Heat Transfer*, vol. 139, pp. 042702–042702–8, 2017.
- [59] T. Gronarz, M. Schnell, C. Siewert, L. Schneiders, W. Schröder, and R. Kneer, "Comparison of scattering behaviour for spherical and non-spherical particles in pulverized coal combustion," *International Journal of Thermal Sciences*, vol. 111, pp. 116–128, 2017.
- [60] D. Trivić, T. O'Brien, and C. Amon, "Modeling the radiation of anisotropically scattering media by coupling Mie theory with finite volume method," *International Journal of Heat and Mass Transfer*, vol. 47, pp. 5765–5780, 2004.
- [61] D. Trivić and C. Amon, "Modeling the 3-D radiation of anisotropically scattering media by two different numerical methods," *International Journal of Heat and Mass Transfer*, vol. 51, pp. 2711–2732, 2008.

- [62] T. Gronarz, C. Höges, V. Kez, M. Habermehl, and R. Kneer, "Comparison of scattering behaviour for inhomogeneous particles in pulverized coal combustion," *International Journal of Thermal Sciences*, vol. 140, pp. 1–7, 2019.
- [63] J. H. Joseph, W. J. Wiscombe, and J. A. Weinman, "The Delta-Eddington Approximation for Radiative Flux Transfer," *Journal of the Atmospheric Sciences*, vol. 33, pp. 2452–2459, 1976.
- [64] L. G. Henyey and J. L. Greenstein, "Diffuse Radiation in the Galaxy," *The Astrophysical Journal*, vol. 93, pp. 70–83, 1941.
- [65] L. A. Dombrovsky and D. Baillis, *Thermal radiation in disperse systems: an engineering approach*, Second Edition. Begell House New York, 2010.
- [66] L. A. Dombrovsky, "The use of transport approximation and diffusion-based models in radiative transfer calculations," in *ICHMT DIGITAL LIBRARY ONLINE*, 2012.
- [67] R. Johansson, B. Leckner, K. Andersson, and F. Johnsson, "Influence of Particle and Gas Radiation in Oxy-fuel Combustion," *International Journal of Heat and Mass Transfer*, vol. 65, pp. 143–152, 2013.
- [68] P. Nakod, G. Krishnamoorthy, M. Sami, and S. Orsino, "A comparative evaluation of gray and non-gray radiation modeling strategies in oxy-coal combustion simulations," *Applied Thermal Engineering*, vol. 54, pp. 422–432, 2013.
- [69] C. Yin, "On Gas and Particle Radiation in Pulverized Fuel Combustion Furnaces," *Applied Energy*, vol. 157, pp. 554–561, 2015.
- [70] T. Gronarz, J. Schulze, M. Laemmerhold, P. Graeser, J. Gorewoda, V. Kez, M. Habermehl, M. Schiemann, J. Ströhle, B. Epple, V. Scherer, and R. Kneer, "Quantification of the Influence of Parameters Determining Radiative Heat Transfer in an Oxy-fuel Operated Boiler," *Fuel Processing Technology*, vol. 157, pp. 76–89, 2017.
- [71] R. Johansson, "Efficient Treatment of Non-grey Radiative Properties of Particles and Gases in Modelling of Radiative Heat Transfer in Combustion Environments," *International Journal of Heat and Mass Transfer*, vol. 108, pp. 519–528, 2017.
- [72] H. Hofgren and B. Sundén, "Evaluation of Planck Mean Coefficients for Particle Radiative Properties in Combustion Environments," *Heat and Mass Transfer*, vol. 51, pp. 507–519, 2015.
- [73] J. Guo, F. Hu, W. Luo, P. Li, and Z. Liu, "A Full Spectrum k-distribution based Non-gray Radiative Property Model for Unburnt Char," *Proceedings of the Combustion Institute*, vol. 37, pp. 3081–3089, 2018.
- [74] J. Guo, F. Hu, W. Luo, P. Li, and Z. Liu, "A Full Spectrum k-distribution based Non-gray Radiative Property Model for Fly Ash Particles," *International Journal of Heat and Mass Transfer*, vol. 118, pp. 103–115, 2018.
- [75] J. Guo, X. Li, X. Huang, Z. Liu, and C. Zheng, "A Full Spectrum k-distribution based Weighted-Sum-of-Gray-Gases Model for Oxy-fuel Combustion," *International Journal of*

- Heat and Mass Transfer*, vol. 90, pp. 218–226, 2015.
- [76] H. B. K. Stephan, *Wärme und Stoffübertragung*, Sechste Auflage. Springer, 2008.
- [77] M. F. Modest, *Radiative Heat Transfer*, Third Edition. Academic press, 2013.
- [78] J. R. Howell, M. P. Mengüç, and R. Siegel, *Thermal Radiation Heat Transfer*, Fifth Edition. CRC press, 2015.
- [79] S. A. Clough, M. J. Iacono, and J.-L. Moncet, “Line-by-line calculations of atmospheric fluxes and cooling rates: Application to water vapor,” *Journal of Geophysical Research: Atmospheres*, vol. 97, pp. 15761–15785, 1992.
- [80] L. Rothman, I. Gordon, R. Barber, H. Dothe, R. Gamache, A. Goldman, V. Perevalov, S. Tashkun, and J. Tennyson, “HITEMP, the high-temperature molecular spectroscopic database,” *Journal of Quantitative Spectroscopy and Radiative Transfer*, vol. 111, pp. 2139–2150, 2010.
- [81] P. Rivière and A. Soufiani, “Updated band model parameters for H<sub>2</sub>O, CO<sub>2</sub>, CH<sub>4</sub> and CO radiation at high temperature,” *International Journal of Heat and Mass Transfer*, vol. 55, pp. 3349–3358, 2012.
- [82] T. Smith, Z. Shen, and J. Friedman, “Evaluation of coefficients for the weighted sum of gray gases model,” *ASME Journal of Heat Transfer*, vol. 104, pp. 602–608, 1982.
- [83] M. K. Denison and B. W. Webb, “An absorption-line blackbody distribution function for efficient calculation of total gas radiative transfer,” *Journal of Quantitative Spectroscopy and Radiative Transfer*, vol. 50, pp. 499–510, 1993.
- [84] L. Pierrot, P. Rivière, A. Soufiani, and J. Taine, “A fictitious-gas-based absorption distribution function global model for radiative transfer in hot gases,” *Journal of Quantitative Spectroscopy and Radiative Transfer*, vol. 62, pp. 609–624, 1999.
- [85] T. Kangwanpongpan, R. C. da Silva, and H. J. Krautz, “Prediction of oxy-coal combustion through an optimized weighted sum of gray gases model,” *Energy*, vol. 41, pp. 244–251, 2012.
- [86] A. H. Al-Abbas, J. Naser, and D. Dodds, “CFD Modelling of Air-fired and Oxy-fuel Combustion in a Large-scale Furnace at Loy Yang A Brown Coal Power Station,” *Fuel*, vol. 102, pp. 646–665, 2012.
- [87] C. Galletti, G. Coraggio, and L. Tognotti, “Numerical investigation of oxy-natural-gas combustion in a semi-industrial furnace: validation of CFD sub-models,” *Fuel*, vol. 109, pp. 445–460, 2013.
- [88] R. M. Goody and Y. L. Yung, *Atmospheric radiation: theoretical basis*, Second Edition. Oxford University Press, 1989.
- [89] W. Malkmus, “Random Lorentz band model with exponential-tailed S<sup>-1</sup> line-intensity distribution function,” *Journal of the Optical Society of America*, vol. 57, pp. 323–329,

- 1967.
- [90] W. Godson, "The evaluation of infra-red radiative fluxes due to atmospheric water vapour," *Quarterly Journal of the Royal Meteorological Society*, vol. 79, pp. 367–379, 1953.
- [91] S. J. Young, "Nonisothermal band model theory," *Journal of Quantitative Spectroscopy and Radiative Transfer*, vol. 18, pp. 1–28, 1977.
- [92] M. F. Modest, "Narrow-band and full-spectrum k-distributions for radiative heat transfer—correlated-k vs. scaling approximation," *Journal of Quantitative Spectroscopy and Radiative Transfer*, vol. 76, pp. 69–83, 2003.
- [93] M. F. Modest and D. C. Haworth, *Radiative Heat Transfer in Turbulent Combustion Systems: Theory and Applications*. Springer, 2016.
- [94] G. Domoto, "Frequency integration for radiative transfer problems involving homogeneous non-gray gases: the inverse transmission function," *Journal of Quantitative Spectroscopy and Radiative Transfer*, vol. 14, pp. 935–942, 1974.
- [95] J. Cai and M. F. Modest, "Absorption coefficient regression scheme for splitting radiative heat sources across phases in gas-particulate mixtures," *Powder Technology*, vol. 265, pp. 76–82, 2014.
- [96] C. Yin, "Refined weighted sum of gray gases model for air-fuel combustion and its impacts," *Energy & Fuels*, vol. 27, pp. 6287–6294, 2013.
- [97] A. Soufiani and J. Taine, "High temperature gas radiative property parameters of statistical narrow-band model for H<sub>2</sub>O, CO<sub>2</sub> and CO, and correlated-K model for H<sub>2</sub>O and CO<sub>2</sub>," *International Journal of Heat and Mass Transfer*, vol. 40, pp. 987–991, 1997.
- [98] F. Cassol, R. Brittes, F. H. França, and O. A. Ezekoye, "Application of the Weighted-Sum-of-Gray-Gases Model for Media Composed of Arbitrary Concentrations of H<sub>2</sub>O, CO<sub>2</sub> and Soot," *International Journal of Heat and Mass Transfer*, vol. 79, pp. 796–806, 2014.
- [99] D. Edwards and A. Balakrishnan, "Thermal radiation by combustion gases," *International Journal of Heat and Mass Transfer*, vol. 16, pp. 25–40, 1973.
- [100] M. Denison and W. Fiveland, "A correlation for the reordered wave number of the wide-band absorptance of radiating gases," *ASME Journal of Heat Transfer*, vol. 119, pp. 853–856, 1997.
- [101] J. Ströhle, "Assessment of the re-ordered wide band model for non-grey radiative transfer calculations in 3D enclosures," *Journal of Quantitative Spectroscopy and Radiative Transfer*, vol. 109, pp. 1622–1640, 2008.
- [102] J. A. Nelder and R. Mead, "A simplex method for function minimization," *The Computer Journal*, vol. 7, pp. 308–313, 1965.

- [103] C. F. Bohren and D. R. Huffman, *Absorption and scattering of light by small particles*. John Wiley & Sons, 1983.
- [104] G. Mie, “Beiträge zur Optik Trüber Medien,” *Annalen der Physik*, vol. 25, pp. 377–445, 1908.
- [105] E. M. Purcell and D. J. Morin, *Electricity and Magnetism*, Third Edition. Cambridge University Press, 2013.
- [106] A. M. Mathai and H. J. Haubold, *Special Functions for Applied Scientists*, vol. 4. Springer, 2008.
- [107] M. Mengüç and R. Viskanta, “On the radiative properties of polydispersions: a simplified approach,” *Combustion Science and Technology*, vol. 44, pp. 143–159, 1985.
- [108] S. Manickavasagam and M. Mengüç, “Effective Optical Properties of Pulverized Coal Particles Determined from FT-IR Spectrometer Experiments,” *Energy & Fuels*, vol. 7, pp. 860–869, 1993.
- [109] R. Gupta and T. Wall, “The Optical Properties of Fly Ash in Coal Fired Furnaces,” *Combustion and Flame*, vol. 61, pp. 145–151, 1985.
- [110] D. Goodwin and M. Mitchner, “Flyash Radiative Properties and Effects on Radiative Heat Transfer in Coal-fired Systems,” *International Journal of Heat and Mass Transfer*, vol. 32, pp. 627–638, 1989.
- [111] A. Lohi, J. Wynnyckyj, and E. Rhodes, “Spectral Measurement of the Complex Refractive Index of Fly Ashes of Canadian Lignite and Sub-bituminous Coals,” *The Canadian Journal of Chemical Engineering*, vol. 70, pp. 751–758, 1992.
- [112] P. Boulet, A. Collin, and J. Consalvi, “On the finite volume method and the discrete ordinates method regarding radiative heat transfer in acute forward anisotropic scattering media,” *Journal of Quantitative Spectroscopy and Radiative Transfer*, vol. 104, pp. 460–473, 2007.
- [113] L. Liu, L. Ruan, and H. Tan, “On the discrete ordinates method for radiative heat transfer in anisotropically scattering media,” *International Journal of Heat and Mass Transfer*, vol. 45, pp. 3259–3262, 2002.
- [114] B. Hunter and Z. Guo, “Phase-Function Normalization in the 3-D Discrete-Ordinates Solution of Radiative Transfer—PART II: Benchmark Comparisons,” *Numerical Heat Transfer, Part B: Fundamentals*, vol. 62, pp. 223–242, 2012.
- [115] B. Hunter and Z. Guo, “Comparison of quadrature schemes in DOM for anisotropic scattering radiative transfer analysis,” *Numerical Heat Transfer, Part B: Fundamentals*, vol. 63, pp. 485–507, 2013.
- [116] F. Lockwood and N. Shah, “A new radiation solution method for incorporation in general combustion prediction procedures,” in *Symposium (international) on combustion*, 1981, vol. 18, pp. 1405–1414.

- [117] F. Liu, G. Smallwood, D. Snelling, and Ö. Gülder, "A ray-tracing method for solving the radiative transfer equation in three-dimensional participating media," *Proceedings of the Combustion Institute*, pp. 1–17–1–22, 1997.
- [118] F. Liu, Ö. Gülder, G. Smallwood, and Y. Ju, "Non-grey gas radiative transfer analyses using the statistical narrow-band model," *International Journal of Heat and Mass Transfer*, vol. 41, pp. 2227–2236, 1998.
- [119] C. Thurgood, A. Pollard, and H. Becker, "The  $T_N$  Quadrature Set for the Discrete Ordinates Method," *ASME Journal of Heat Transfer*, vol. 117, pp. 1068–1070, 1995.
- [120] T. Kim, J. Menart, and H. S. Lee, "Nongray Radiative Gas Analyses using the SN Discrete Ordinates Method," *ASME Journal of Heat Transfer*, vol. 113, pp. 946–952, 1991.
- [121] K. D. Lathrop and B. G. Carlson, "Discrete Ordinates Angular Quadrature of the Neutron Transport Equation," 1964.
- [122] W. Fiveland, "Discrete-ordinates solutions of the radiative transport equation for rectangular enclosures," *ASME Journal of Heat Transfer*, vol. 106, pp. 699–706, 1984.
- [123] W. Fiveland, "Three-dimensional radiative heat-transfer solutions by the discrete-ordinates method," *Journal of Thermophysics and Heat Transfer*, vol. 2, pp. 309–316, 1988.
- [124] G. Raithby and E. Chui, "A finite-volume method for predicting a radiant heat transfer in enclosures with participating media," *ASME Journal of Heat Transfer*, vol. 112, pp. 415–423, 1990.
- [125] J. C. Chai, H. S. Lee, and S. V. Patankar, "Finite Volume Method for Radiation Heat Transfer," *Journal of Thermophysics and Heat Transfer*, vol. 8, pp. 419–425, 1994.
- [126] S. H. Kim and K. Y. Huh, "A new angular discretization scheme of the finite volume method for 3-D radiative heat transfer in absorbing, emitting and anisotropically scattering media," *International Journal of Heat and Mass Transfer*, vol. 43, pp. 1233–1242, 2000.
- [127] S. C. Mishra and H. K. Roy, "Solving transient conduction and radiation heat transfer problems using the lattice Boltzmann method and the finite volume method," *Journal of Computational Physics*, vol. 223, pp. 89–107, 2007.
- [128] J. Chai, H. S. Lee, and S. V. Patankar, "Improved treatment of scattering using the discrete ordinates method," *ASME Journal of Heat Transfer*, vol. 116, pp. 260–263, 1994.
- [129] W. Minkowycz, E. Sparrow, and J. Murthy, *Handbook of Numerical Heat Transfer*. Wiley, New York, 2006.
- [130] F. Liu, H. Becker, and A. Pollard, "Spatial differencing schemes of the discrete-ordinates method," *Numerical Heat Transfer*, vol. 30, pp. 23–43, 1996.
- [131] P. J. Coelho, "Advances in the discrete ordinates and finite volume methods for the solution of radiative heat transfer problems in participating media," *Journal of*

- Quantitative Spectroscopy and Radiative Transfer*, vol. 145, pp. 121–146, 2014.
- [132] J. Ströhle, U. Schnell, and K. R. Hein, “A mean flux discrete ordinates interpolation scheme for general co-ordinates,” in *ICHMT DIGITAL LIBRARY ONLINE*, 2001.
- [133] J. Ströhle, T. Myhrvold, and N. A. Røkke, “A numerical evaluation of different oxy-fuel concepts for a gas turbine combustor,” in *ASME Turbo Expo 2004: Power for Land, Sea, and air*, 2004, pp. 283–291.
- [134] J. Zhang, T. Ito, S. Ito, D. Riechelmann, and T. Fujimori, “Numerical Investigation of Oxy-coal Combustion in a Large-scale Furnace: Non-gray Effect of Gas and Role of Particle Radiation,” *Fuel*, vol. 139, pp. 87–93, 2015.
- [135] J. Ströhle, B. Epple, and M. Orth, “Spectral modelling of radiative heat transfer in oxy-coal combustion,” in *1st Oxyfuel Combustion Conference, Cottbus, Germany*, 2009.
- [136] E. Chui, G. Raithby, and P. Hughes, “Prediction of radiative transfer in cylindrical enclosures with the finite volume method,” *Journal of Thermophysics and Heat Transfer*, vol. 6, pp. 605–611, 1992.
- [137] J. Consalvi and F. Liu, “Radiative heat transfer in the core of axisymmetric pool fires-I: Evaluation of approximate radiative property models,” *International Journal of Thermal Sciences*, vol. 84, pp. 104–117, 2014.
- [138] X. Yang, A. Clements, J. Szuhánszki, X. Huang, O. F. Moguel, J. Li, J. Gibbins, Z. Liu, C. Zheng, D. Ingham, and others, “Prediction of the radiative heat transfer in small and large scale oxy-coal furnaces,” *Applied energy*, vol. 211, pp. 523–537, 2018.
- [139] A. Hoff, “Implementierung und Validierung verschiedener Gasstrahlungsmodelle zur Simulation von Oxyfuel-Verbrennungsprozessen,” 2015.